Templated Self-Assembly for Complex Pattern Fabrication

by

Jae-Byum Chang

B.S. Physics
Korea Advanced Institute of Science and Technology, Daejeon, Korea (2008)

Submitted to the Department of Materials Science and Engineering
in Partial Fulfillment of the Requirements for the Degree of

Doctor of Philosophy in Materials Science and Engineering
at the
MASSACHUSETTS INSTITUTE OF TECHNOLOGY
February 2014

Signature of Author : .....
Department of Materials Science and Engineering
January 7th, 2014

Certified by : .....
Karl K. Berggren
Professor of Electrical Engineering and Computer Science
Thesis Supervisor

Accepted by : .....
Gerbrand Ceder
R.P. Simmons Professor of Materials Science and Engineering
Chair, Department of Committee on Graduate Students

Templated Self-Assembly for Complex Pattern Fabrication

by
Jae-Byum Chang
Submitted to the Department of Materials Science and Engineering
on January 7, 2014, in partial fulfillment of the
requirements for the degree of
Doctor of Philosophy in Materials Science and Engineering

Abstract

The long-term goal of my Ph.D. study has been controlling the self-assembly of various materials using state-of-the-art nanofabrication techniques. Electron-beam lithography has been used for decades to generate nanoscale patterns, but its throughput is not high enough for fabricating sub-10-nm patterns over a large area. Templated block copolymer(BCP) self assembly is attractive for fabricating few-nanometer-scale structures at high throughput. On an unpatterned substrate, block copolymer self-assembly generates dense arrays of lines or dots without long-range order. Fortunately, physical features defined by electron lithography can guide the self-assembly of block copolymer. In our previous work, the orientation of cylindrical phase block copolymer was controlled simply by changing the distance between physical features, and resulting polymer patterns were analyzed by an image analysis program.

Here, we first demonstrated high throughput sub-10-nm feature sizes by applying the same approach to a cylindrical morphology 16kg/mol PS-PDMS block copolymer. The half-pitch of the PDMS cylinders of this block copolymer film is 9 nm, so sub-10-nm structures can be fabricated. We also applied the similar approach to a triblock terpolymer to achieve dot patterns with square symmetry. To achieve a more complex pattern, electron-beam induced cross-linking of a block copolymer and second solvent-annealing process was used. By using this method, a line-dot hybrid pattern was achieved. Despite that the block copolymer self-assembly area had been heavily studied, researchers had yet to ascertain how to design nanostructures to achieve a desired target pattern using block copolymers. To address this problem, we developed a modular method that greatly simplifies the nanostructure design, and using this method, we achieved a circuit-like block-copolymer pattern over a large area. The key innovation is the use of a binary set of tiles that can be used to very simply cover the desired patterning area. Despite the simplicity of the approach, by exploiting neighbor-neighbor interactions of the tiles, a complex final pattern can be formed. The vision is thus one of programmability of patterning by using a simple instruction set. This development will thus be of interest to scientists and engineers across many fields involving self-assembly, including biomolecule, quantum-dot or nanowire positioning; algorithmic self-assembly; and integrated-circuit development.

We applied this concept - controlling the assembly of materials using nanostructures - to a different material, protein. Single-molecule protein arrays are useful tools for studying biological phenomena at the single-molecule level, but have been developed only for a few specific proteins using the streptavidin-biotin complex as a linker. By using carefully designed gold nanopatterns and cysteine-gold interaction, we developed a process to make single-molecule protein arrays that can be used for patterning a broad range of proteins.

Thesis Supervisor: Karl K. Berggren
Title: Associate Professor of Electrical Engineering and Computer Science

Acknowledgements

First of all, I would like to express my sincere thanks to my thesis advisor, Prof. Karl K. Berggren for giving me advices on research, graduate school life, and my future career. He encouraged me to develop new ideas by connecting many different ideas and topics, and also gave me opportunities to work on diverse fields with many collaborators. I appreciate his encouraging, guidance, and training.

I also would like to express my deep gratitude to Professor Caroline A. Ross, Professor Alfredo Alexander-Katz, and Professor Bradley D. Olsen for their advices and guidance as my thesis committee. I would like to express appreciation to Professor Caroline A. Ross for her kind advices on block copolymer self-assembly and help with defining research directions and writing papers.

I would like to thank Professor Amy E. Keating and Yong Ho Kim for the successful collaboration on templating biomolecules. While working with them on the biomolecule project, I learned a lot about the chemical properties and functions of biomolecules.

I would like to thank Joel Yang and Yeon Sik Jung for teaching me nanofabrication techniques and block copolymer self-assembly. Also, I would like to thank Jeong Gon Son and Hong Kyoon Choi, and other block copolymer team members for their collaborations. I do believe that I worked with the best team in the world.

I would like to thank Jim Daley and Mark Mondol for their advices, comments, and technical supports, and also I would like to thank my friends, group members, officemates, and classmates.

I would like to express the deepest gratitude to my mom and dad for their trust, support, and love. Finally, I would like to thank my wife, Won Hye Chung for her understanding, encouragement, and love.

Contents

List of Figures

beam irradiation to be aligned with the microdomain orientation, though not with a specific microdomain[15].

1. Introduction

The objective of this thesis is controlling the self-assembly of materials at nanoscale to fabricate complex pattern and develop a new computational scheme. Nanoscale pattern-generation methods such as particle beam[1–3] and extreme ultraviolet lithography[4], nanoimprint lithography(NIL)[5], and templated self-assembly(TSA)[6–8] have become interesting manufacturing technologies because of advantages such as <10 nm feature sizes[9], the ability to form arbitrary designs[7], compatibility with a wide variety of materials with different properties[10,11], and the ability to pattern wafer-size areas[12]. However, the real-world adoption of these techniques is hindered by limitations such as slow patterning times, lack of pattern fidelity, defectivity[13], and inadequate scientific understanding of the methods[14].

Here I aim to address the limitations of nanoscale pattern-generation methods by increasing the fundamental scientific understanding, pattern complexity, and throughput of templated self-assembly-based pattern generation. With these achievements, nanomanufacturing can leverage the many benefits of TSA such as <10 nm feature size, high pattern fidelity, and material versatility. We will outline our prior work in the TSA of block copolymers (BCPs) and nanocollapse (NC) of resist features, describe our research approach for overcoming the limitation of TSA, and discuss methods for increasing the educational and broad societal impact of this work.

1.1 Current pattern generation methods

The fabrication of integrated circuits has been propelled by Moore's Law and requires advances in nanopatterning, but these advances are also required for a plethora of other emerging technologies. Examples of other applications include nanoelectronic[15] and energy devices[16], biosensing[17], plasmonics[18], nano-electronic and mechanical systems (NEMS)[19], and surface energy engineering[20].

Particle-beam-lithography, extreme ultraviolet lithography, templated self-assembly, and nano-imprint-lithography are the most developed pattern-generation methods. These methods each encompass different advantages and disadvantages, but none of them have emerged as the go-to technique for complex, defect-free, high-throughput, small-scale nanopattern fabrication. Some of the limitations include slow patterning times, lack of pattern fidelity, defectivity, and inadequate scientific understanding. We suggest that the development of the above emerging technologies requires increases in three of these aspects: fundamental scientific understanding and modeling, complex patterning ability, and throughput.

1.2 Self-assembly as a pattern generation method

Self-assembly has been investigated to understand its potential as a pattern-generation method[21–30]. A wide variety of two- and three-dimensional patterns have emerged through the self-assembly of simple building blocks, for example micropillars[23] and dot arrays[21], and of a wide variety of materials, for example gold nanoparticles[24], organic backbone DNA[31], or polymeric crystals[6].

Self-assembly has a number of other key advantages such as nanoscale lengths[22], short assembly times[32], high structural uniformity[24] and the ability to transfer to other materials[6]. As a result, self-assembly provides promise for the generation of a wide variety of nanoscale patterns as exemplified in Figure 1(a-d). Despite these advantages, self-assembly typically lacks complex design at the microscale or uniform order at the macroscale, which limits it applications.

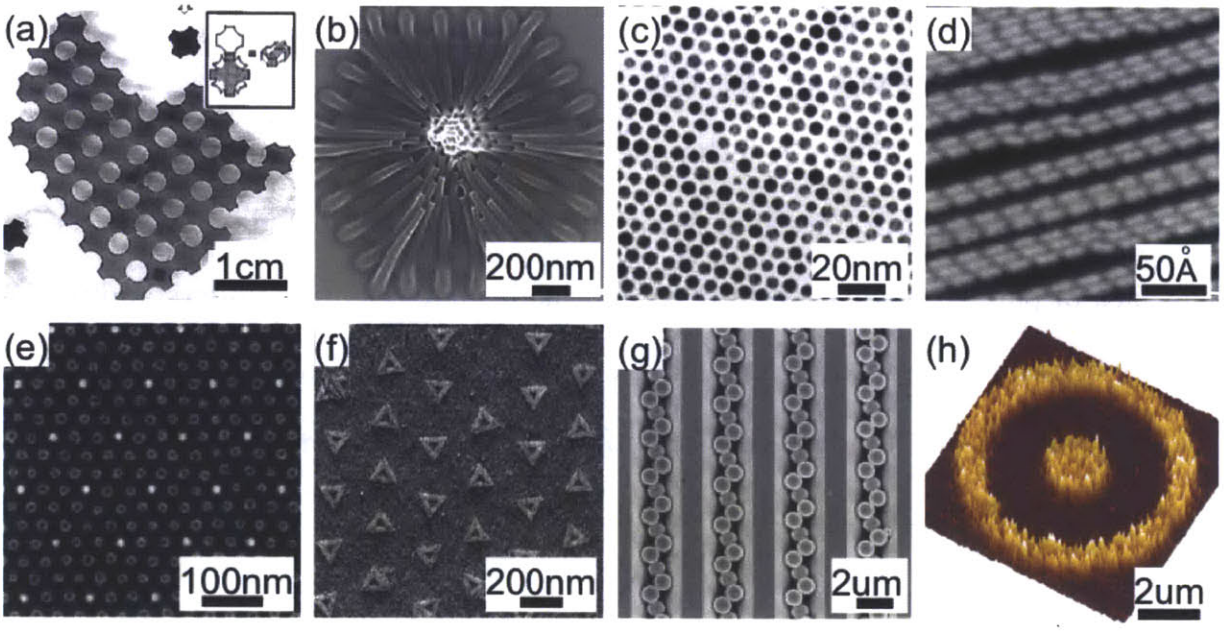

Figure 1-1. Examples of self-assembled patterns from (b,e) our group and (a,c,d,f-h) other references. Self-assembled (a) millimeter-sized crosses[21]; (b) nanopillars[32]; (c) gold nanoparticles[24]; (d) PVBA on Ag(111)[22]. (e-h) Patterns generated from self-assembly with lithographically defined templates. (e) Self-assembled PS-*b*-PDMS block copolymer templated by topographical templates[6]. (f) Self-assembled DNA patterns templated by chemical patterns[33]. (g) Self-assembled microbeads in topographic tranches[34]. (h) Self-assembled gold particles on chemical patterns[35].

To this end, researchers have investigated templates to direct self-assembly[33–51]. These templates aim to provide control over the self-assembled patterns: for example higher complexity at the few-feature-length scale[7] and higher order at the macroscopic length scale[24]. These templates provide a higher driving force towards desired orientations or patterns and therefore assist free-energy-minimization[6]. This driving force augmentation is typically accomplished by matching patterned surfaces features (of either different chemistries or physical topography) with characteristic geometries of the self-assembly system[52]. Examples of complex and long-range order of templated self-assembled materials are shown in Figure 1 (e-h). After self-assembly, the template can remain as a component of the final pattern[6] or be removed to leave only the self-assembled material[53].

Chapter 2 shows a method of achieving long-range ordered block copolymer patterns with a controlled orientation by using topographic template arrays. The orientation of the block copolymer patterns was understood by the concept of commensurate and the area fraction of grains was understood and explained by using an analytical theory. By extending this approach, a long-range ordered sub-10-nm linear pattern is also achieved. Chapter 2 also demonstrates a method of achieving square array of dots and dot-line hybrid patterns. The square arrays of dots are achieved by using triblock terpolymer and dot-line hybrid structures were achieved by using e-beam induced cross-linking.

Chapter 3 shows a new method of designing topographic template for achieving a circuit-like block copolymer patterns. Set of topographic template tiles consisting of

square lattices of posts with a restricted range of geometric features is developed. The block-copolymer patterns resulting from all tile arrangements are determined. By combining tiles in different ways, it is possible to predict a relatively simple template that will direct the formation of non-trivial block-copolymer patterns, providing a new template design method for a complex block-copolymer pattern.

In chapter 4, single-molecule protein arrays are developed. Cysteine residue of a protein are used to direct the attachment of the proteins to gold nanostructures . By using a fluorescence microscope, we show that the proteins were localized around the nanostructures. We expect that the techniques developed in this program could be used for studying biological phenomena at a single molecular level or developing an ultra-sensitive biomedical sensors or devices.

2. Templated self-assembly of block copolymers for periodic pattern fabrication

Templated self-assembly of block copolymers has been used for patterning periodic nanoscale patterns over large area. Here, we develop a method of achieving long-range ordered linear block copolymer patterns and circular patterns by using topographic templates. We also demonstrate the fabrication of dot-line hybrid patterns by using e-beam induced cross-linking.

2.1 Introduction

Self-assembly has a number of other key advantages such as nanoscale lengths[22], short assembly times[32], high structural uniformity[24] and the ability to transfer to other materials[6]. As a result, self-assembly provides promise for the generation of a wide variety of nanoscale patterns.

2.1.1 Block copolymer self-assembly

Block copolymers consist of two or several blocks of polymers and the blocks are joined at their ends by a covalent bond and form a single polymer chain. Figure 2-1 shows three different classes of block copolymers among a variety of molecular architectures: (1) diblock copolymer; (2) triblock copolymer; and (3) starblock terpolymer. Among these three classes of block copolymers, diblock copolymer is the simplest one. In the figure, solid and dotted lines represent different blocks of the block copolymer.

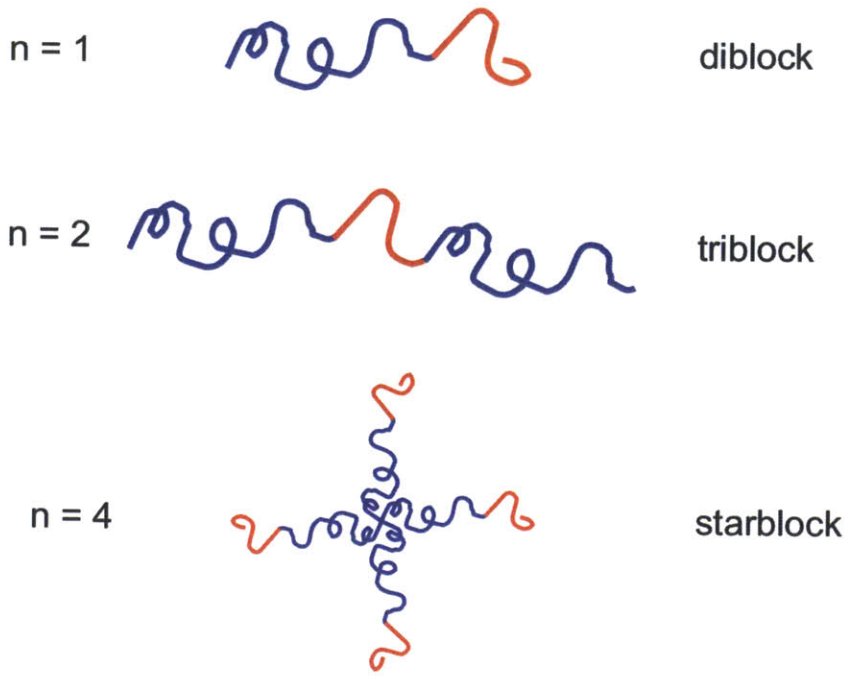

Figure 2-1. Schematics showing diblock copolymer, triblock copolymer, and starblock copolymer[54]. Redrawn from Figure 1 of Ref. 54.

Because the two blocks have different chemical properties and the solubility parameters of the two blocks are different, the block copolymer molecules tend to segregate into microstructures when they have enough kinetics energy to move and also when the temperature of the polymers is below the order-disorder temperature. This is called microphase separation. In this polymer molecule arrangement, the contact between similar blocks is maximized and the contact between the dissimilar blocks is minimized, which make the free energy of the system minimum. As the two blocks are covalently linked, the two blocks cannot simply phase-separate by making two layers of polymer chains, such as oil droplets in water. This phenomenon, microphase separation, depends on the temperature of the system, as at high temperature entropy of mixing becomes more dominant and at low temperature enthalpy of separation becomes more dominant.

To quantify the free energy cost of the separation of dissimilar two blocks, Flory-Huggins parameter χ is used[54]. In addition the Flory-Huggins parameter, two more parameters are used: (1) N, the degree of polymerization; and (2) f_A, the volume fraction of one block. The morphology generated by the microphase separation of two blocks depends on the volume fraction of one block, as shown in Figure 2-1. Among the three parameters $\chi, N, and\ f_A$, χ depends on the monomer pair of the two blocks and $N\ and\ f_A$ depends on the length of the total block copolymer chain and the relative ratio of one block to the other block.

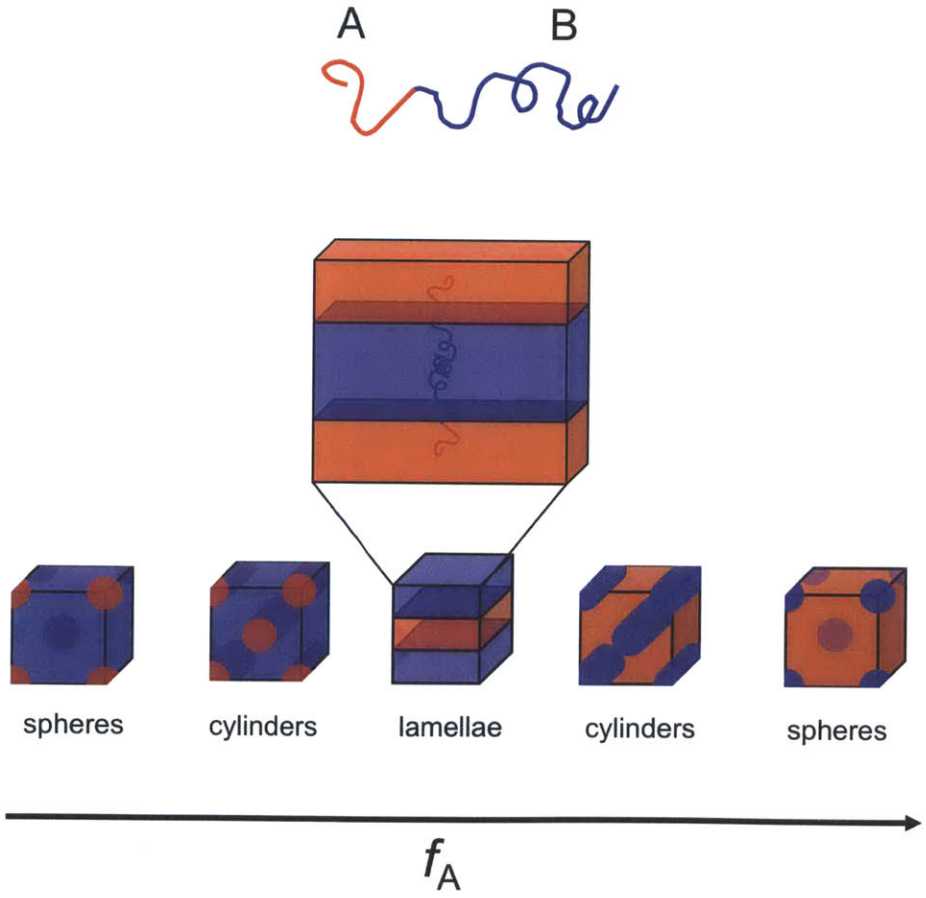

Figure 2-2. Schematics showing structures that can be formed when the block copolymer with various volume fraction self-assemble[55]. Redrawn from Ref. 55.

As shown above, the morphology of the microdomains formed by the self-assembly of block copolymers changes from spheres to lamellae as the volume fraction of one block increases. When the volume fraction of A block is small, A block forms a spherical microdomains embedded in the B block matrix. On the contrary, if the volume fraction of A block is large, A block forms a matrix and B block forms a spherical microdomains embedded in the A block matrix. As the microphase separation depends on the temperature of the system, the parameter measuring the free energy cost of the separation, χ also depends on the temperature. Generally, the temperature dependence of Flurry-Higgins parameter is given by $\chi = \frac{\alpha}{T} + \beta$ [54]. As shown in the equation, Flurry-Huggins parameter decreases as the temperature of the system increases.

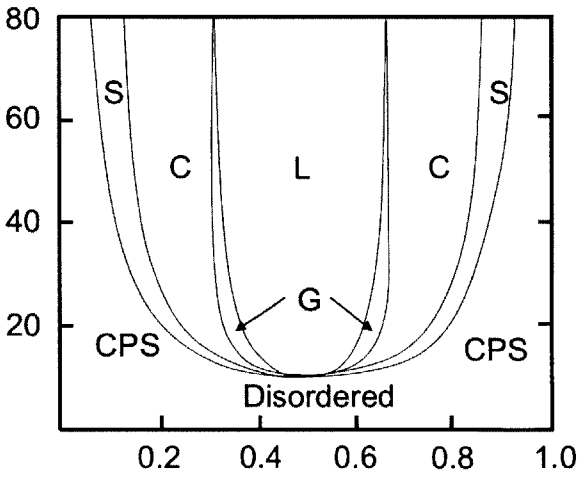

Figure 2-3. Simulated phase diagram of a block copolymer. polyisoprene-b-polystyrene[56]. Redrawn from Ref. 56.

Figure 2-3 shows how the morphology of the self-assembled diblock copolymers changes depending on the volume fraction of one block and also χN of the block copolymer. Note that the morphology changes depending not only on the relative length of one block, but also on the total length of the block copolymer. Also, when χN is smaller than a specific value, block copolymer chain cannot undergo the microphase separation, because when the chain is short, the area of the interface between two dissimilar blocks doesn't change, but the enthalpy gained by the separation decreases. Figure 2-3(b) shows experimental result of polyisoprene-b-polystyrene.

In this study, we used a polystyrene-b-polydimethylsiloxane (PS-*b*-PDMS) block copolymer and this block copolymer is composed of a long styrene polymer chain and long dimethylsiloxane chain. Block copolymers have been recently heavily studied because it can form periodic nanoscale objects over a large area with a relatively easy and rapid process. Recently, several groups have started studies on using the self-assembly of block copolymers in nanotechnology. The generation of the self-assembled nanoscale patterns over a large area in two dimensions (2D) could be used as a method for improving the throughput of relatively slow electron-beam lithography or for improving the resolution of optical lithography.

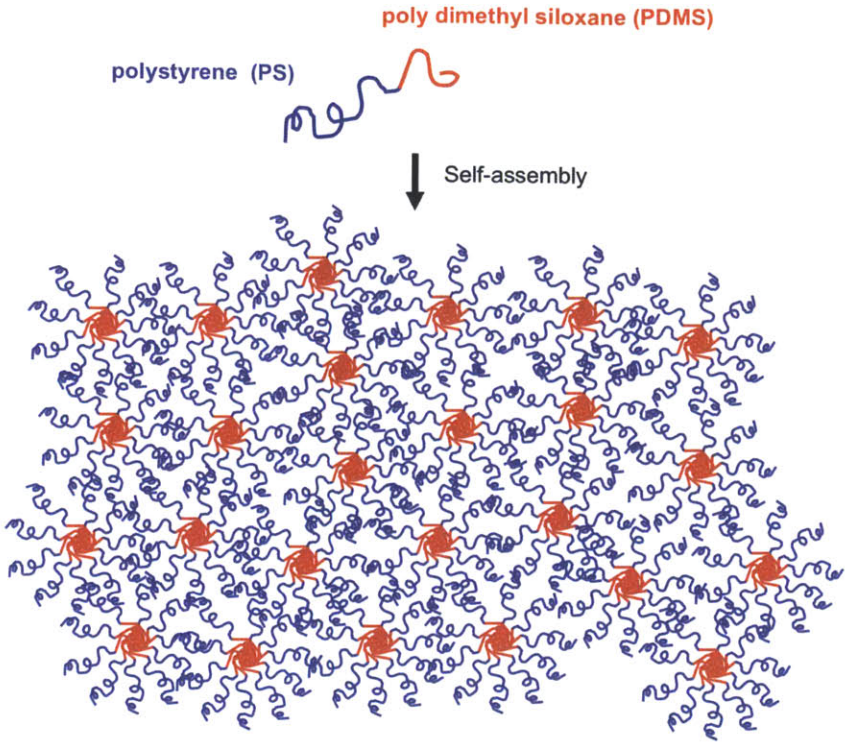

Figure 2-4. Schematic diagram showing how a PS-b-PDMS block copolymer self-assembles. Here, the self-assembled structure consists of spherical microdomains made of PDMS and a PS matrix.

2.1.2 Topographic templates

In our previous work, we used sphere-[6] and cylinder-[7] forming poly(styrene)-block-poly(dimethylsiloxane) (PS-b-PDMS) block copolymer. The advantages of PS-b-PDMS are a high χ parameter and high etch selectivity[57]. A chi parameter of 0.21 for PS-b-PDMS is much higher than PS-b-PMMA, which has also been used for block copolymer lithography[46]. Furthermore, because PDMS is composed of a silicon backbone, it is selectively resistant to oxygen plasma etching. The PS matrix can be easily removed by

an oxygen plasma etch to reveal PDMS microdomains[57]. PDMS microdomains in a self-assembled PS-b-PDMS block copolymer film can be guided by topographic post templates to produce nanopatterns with a precisely determined orientation and long-range order. Topographic post templates were fabricated by electron-beam exposure of hydrogen silsesquioxane (HSQ) and a high-resolution development system[58]. The surface of the substrate and the templates were functionalized by a PDMS brush to attract a PDMS block in PS-b-PDMS. We achieved long-range ordered close-packed dot patterns with period of 40 nm with 51.5 kg/mol spherical PS-b-PDMS[6]. Also, we achieved long-range ordered line patterns with period of 35 nm with 45.5 kg/mol cylindrical PS-b-PDMS[7]. The PDMS lines were aligned in one orientation when the x- and y-pitch of the template array satisfied the commensurate condition (commensurate condition: $1/L_o^2=a^2/L_x^2+b^2/L_y^2$, where a and b are integers and L_o is the natural pitch, L_x and L_y are the x- and y-pitch). We also demonstrated local control of PDMS lines by using elliptical or double-dot, instead of circular, template posts. The PDMS lines were constrained to be oriented parallel to the elliptical or double-dot templates. Complex patterns such as jogs and cross patterns were achieved by using elliptical and double-dot posts[7].

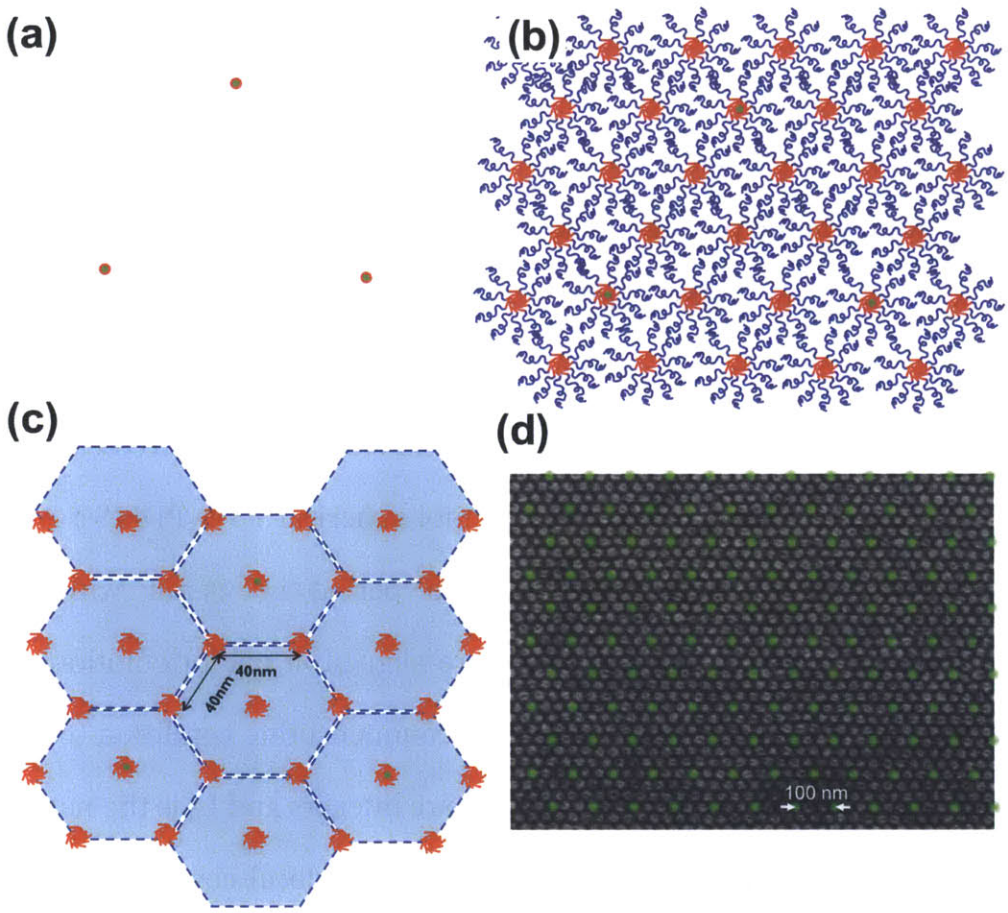

Figure 2-5. Schematic diagram showing how topographic template functionalized by one of the two blocks can be used for achieving long-range ordered microdomains.

Fabrication of multilevel thin film devices has some applications such as fabrication of metamaterials[59] and perhaps also via holes in integrated circuit manufacturing[60]. We showed that PS-brush-functionalized templating HSQ post arrays could control the alignment and the morphology of PS-b-PDMS BCP in two different layers. We fabricated very complicated three-dimensional structures, junctions, periodic superstructures and bends in different levels of the BCP. Moreover, we changed the morphology of the BCP in one of the layers from the original cylinders to the other morphologies, and therefore have two different morphologies on top of each other.

2.1.3 Pattern transfer methods

The patterned formed by the block copolymers need to be transferred to another material, such as magnetic materials or metals to fabricate bit-pattered magnetic media or integrated circuit. There are numerous studies that have reported the successful pattern transfer of 2D and 3D self-assembled structures onto functional materials from metals to dielectrics and graphene using dry or wet etching or lift-off processes[61–66]. For example, as shown in Figure 2-6 one of pattern transfer methods developed for PS-b-PDMS block copolymers[67]. In this method, first the PDMS microdomains are generated by an annealing of a block copolymer film, and then a thick metal layer is deposited on top of the substrate. After that, RIE is used to remove the top layer of metal and after that to remove PDMS microdomains to reveal the metal structure between the PDSM microdomains. It was shown that this method can be applied to various metals, such as Pt, Ti, and Ni.

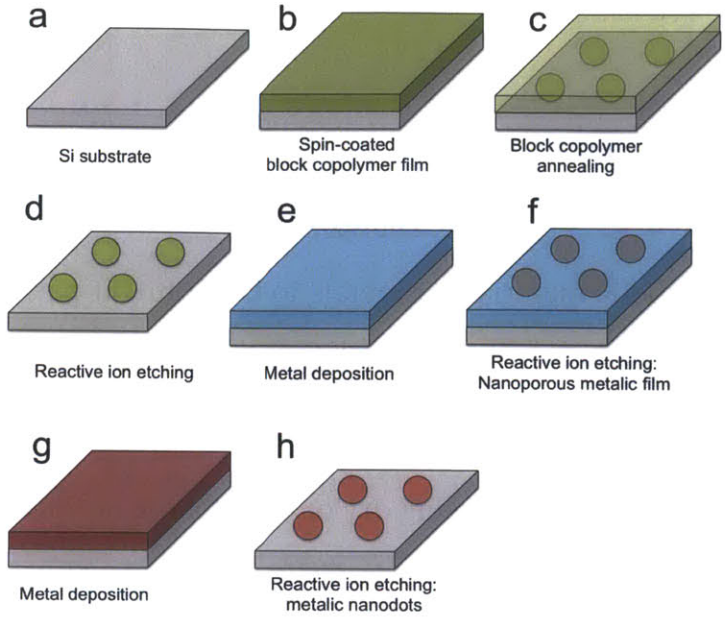

Figure 2-6. Schematics showing a method of pattern transfer from the self-assembly of PS-b-PDMS block copolymer film to metals[67]. Redrawn from Ref. 67.

There are also methods for transferring 3-D block copolymer structures to another materials, such as electrodeposition, sol-gel reactions, chemical vapor deposition, atomic layer deposition or chemical reduction processes, as well as codeposition or coassembly of the block copolymer with inorganic materials[68–70]. Sub-μm-scale 3D nanotemplates fabricated by 3D photolithography, mentioned above, have been successfully transformed into stretchable conductors, photonic crystals, and carbon microstructures via similar dry/wet backfilling or pyrolysis[71–73]. providing a starting point for developing pattern transfer processes applicable to 3D BCPs.

2.2 Long-range ordered line patterns by using topographic template arrays.

Block copolymer film on a smooth substrate generates a nanoscale patterns over the

substrate, but the pattern is not ordered along one orientation. The pattern consists of many grains with different orientations. To use the self-assembled block copolymer patterns for fabricating integrated circuits of magnetic storage media, a method of achieving long-range ordered block copolymer patterns should be developed.

2.2.1 Orientation control of sub-20-nm line patterns

Templated block copolymer self-assembly is attractive for fabricating few-nanometer-scale structures at high throughput. Among several morphologies of block copolymers, the cylindrical morphology is particularly important because it can be used for defining metallization lines in IC circuit fabrication. However, to be used in the IC circuit fabrication, we need to achieve a long-range ordered cylindrical-morphology block copolymer patterns, and also we need to be able to control the orientation of the patterns. In our previous study, we have developed a method of achieving long-range order from a self-assembly spherical-morphology PS-b-PDMS block copolymers by using minority block coated topographic template and commensurability[6].

We applied the same strategy to the self-assembly of cylindrical-morphology block copolymer. Figure 2-7 shows a scanning electron micrograph (SEM) of a guided cylindrical-morphology polystyrene-polydimethylsiloxane (PS-PDMS) block copolymer. Hydrogen silsesquioxane (HSQ) was used for the physical features of the template[58]. When the distance between the physical features satisfies the commensurate condition, the whole pattern was composed of a single orientation of in-plane PDMS cylinders in a PS matrix.

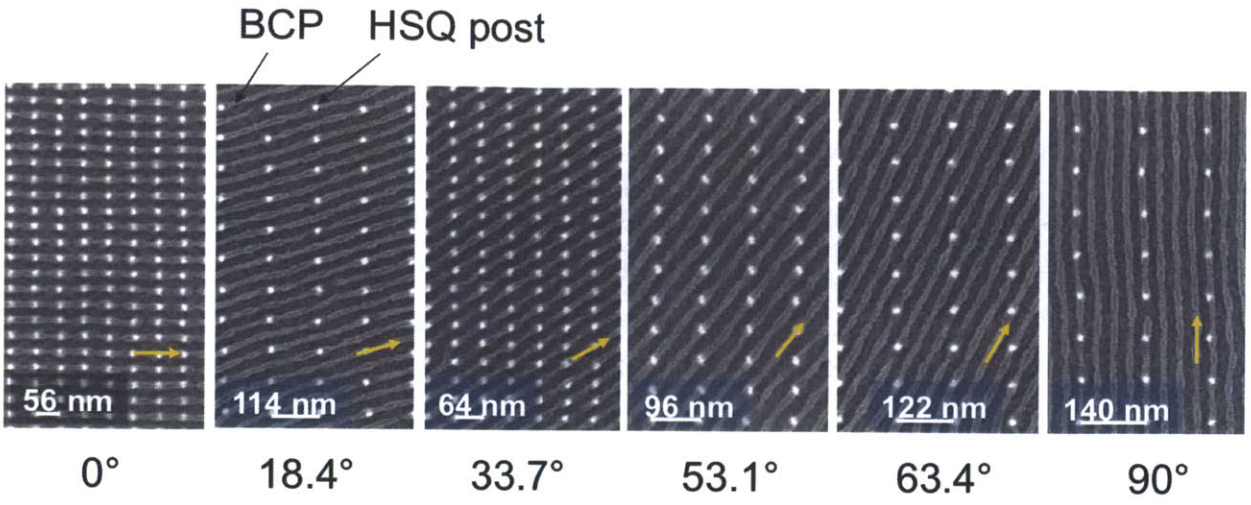

Figure 2-7. SEM images of PDMS microdomains formed on the patterned substrate. The bright dots are HSQ posts and gray lines are PDMS microdomains after the top PDMS surface and PS matrix are removed. Yellow arrows represent the orientations of the PDMS microdomains. L_x/L_y was fixed at 1.5. In the SEM images, the error bars show the L_X of the template arrays[7].

As shown in Figure 2-7, the PDMS microdomains were aligned along one direction when the block copolymer film was annealed on a patterned substrate. To predict and understand the orientation of the microdomains, we used three parameters, L_x, L_y, and L_o. L_x is the periodicity of the template array in the x-axis, and L_y is the periodicity of the template array in the y-axis, and Lo is the natural periodicity of the block copolymer. When $L_x=L_o$, the block copolymer cylinders were aligned along the y-axis, because in this orientation, the distance between two neighboring PDMS lines was equal to Lo, the natural periodicity of the block copolymer. However, for a larger L_x, such as Lo = (1/Lx^2+1/L_y^2)^0.5, the PDMS microdomains were aligned in the diagonal direction, also because in this orientation the distance between two PDMS microdomains was

equal to the natural periodicity of the block copolymer. In figure 2-7, the ratio between L_x and L_y (L_x/L_y) was fixed at 1.5. So, depending on L_x, the orientation of the block copolymer cylinders changed to make the distance between two neighboring PDMS microdomains was equal to the natural periodicity of the block copolymer.

2.3 Sub-10-nm pattern from a 16 kg/mol PS-b-PDMS block copolymer

Self-assembly of block copolymers is currently of interest as a method for fabricating nanopatterns[54,74–76]. It can generate dense arrays of nanoscale spherical, cylindrical or lamellar microdomains which can be used as lithographic masks[77–79]. Compared with conventional lithography methods, the self-assembly of block copolymers has two advantages: (1) the periodicity of dense structures can be scaled down to ~10 nm, which is well beyond the resolution limit of optical lithography;[80] and (2) nanopatterns can be fabricated over a large area in parallel, so the throughput can be several orders of magnitude higher than that of electron-beam lithography (EBL)[9]. Based on these two advantages, self-assembly of block copolymers has been used in the fabrication of devices including nanocrystal flash memory, nanowire transistors, gas sensors, patterned magnetic recording media, and contact holes for transistors[60,64,81–84].

Microdomains generated in a self-assembled block copolymer film can be guided by templates to produce nanopatterns with a precisely determined orientation and long-range order. Periodic templates, such as chemical patterns[46,52,85–87], topographic trenches[88,89], facets of single crystal sapphire[90], or other block copolymers[9,80] have been

used to impose long-range order on the microdomains. In prior work, sparse post arrays were used to control the in-plane orientation of 51 kg/mol spherical and 45.5 kg/mol cylindrical morphology poly(styrene-block-dimethylsiloxane) (PS-b-PDMS) block copolymer microdomains with a period of 40 nm and 34 nm respectively[6,7]. Designed post arrays were also used to locally control the orientations of the cylindrical microdomains, and to generate complex device-like nanopatterns[7].

To achieve sub-10-nm complex nanopatterns based on the self-assembly of block copolymers, a block copolymer with a sub-10-nm periodicity and a process for templating its self-assembly are required. Sub-10-nm periodicity has been achieved by various block copolymer systems, such as PS-b-PDMS[9,80], PS-b-PEO[11,90], and PMMA-b-PMAPOSS[10]. Several different approaches have been used to template the self-assembly of a block copolymer with a sub-10-nm periodicity, but sub-10-nm block copolymer patterns with a specific registration with substrate features have not yet been demonstrated[53].

Here, we present a method for achieving well-oriented and registered sub-10-nm PS-b-PDMS block copolymer patterns using topographic templates. To template the self-assembly of PS-b-PDMS with a sub-10-nm periodicity, the diameter of the posts must also be scaled down to the sub-10-nm range in concert with using lower molecular weight block copolymers which generate periodic patterns with sub-10-nm features. However, the fabrication of sub-10-nm posts is challenging even with state-of-the-art lithography[91]. To overcome this challenge, processes are needed to fabricate the templates, and a better understanding of the interaction between the microdomains and

the posts is required. In this work, the templated self-assembly of a 16 kg/mol cylindrical morphology PS-b-PDMS block copolymer with 18 nm period is demonstrated using sparse topographic templates. The interaction between the block copolymer and post templates with a range of diameters and heights was examined, and topographic templates were designed to align the block copolymer microdomains in specific directions on the substrate.

2.3.1 Orientation control of sub-10-nm line patterns

A 16 kg/mol cylindrical morphology PS-b-PDMS block copolymer (PDI ~1.08, f_{PS} ~0.69) was spin-coated onto a substrate to form a monolayer of in-plane PDMS cylinders. The thickness of the film was 24 nm, which is commensurate with a 18-nm-periodicity in-plane cylinder, a top surface layer of PDMS, and a bottom surface layer of PDMS. A 24-nm-thick films of the block copolymer were annealed in an acetone vapor in a chamber with a small leak until complete evaporation of solvent (~ 4 hr). During the solvent annealing, each block swelled to a different swelling ratio (PS ~ 1.62, PDMS ~ 1.44), which increased the effective f_{PS} from 0.67 to 0.70[53]. Solvent uptake by the film lowered the Flory-Huggins interaction parameter compared to that of the dried film. The annealed films were etched by oxygen plasma to remove the PS and reveal the oxidized PDMS microdomains. Figure 2-8(a) shows randomly oriented linear patterns with 18 nm periodicity formed on a smooth substrate.

To impose long-range order and to control pattern registration, we used rectangular arrays of posts with various periods L_x and L_y, as depicted in figure 2-8(b). In prior

work, posts with heights of ~35 nm and diameters of ~10 nm were effective in templating the self-assembly of a 45 kg/mol cylindrical morphology PS-b-PDMS block copolymer with periodicity of 34 nm[7]. Extrapolation of these dimensions suggests that posts with a height of ~18 nm and a diameter of ~5 nm would be needed to effectively template the self-assembly of a 18 nm period block copolymer. However, fabricating posts with diameter smaller than 10 nm is difficult with a conventional electron beam lithography system[58]. In this work, posts were fabricated with diameters of 6.3 nm – 13.8 nm and heights of 12 – 27 nm from high-contrast negative-tone-resist hydrogen silsesquioxane (HSQ) and a high contrast salty development system[62].

The posts were functionalized with a PDMS brush to be attractive to the PDMS block of the block copolymer. Prior work on a 34 nm period block copolymer[7] showed that the cylindrical PDMS microdomains contact the PDMS-coated posts and orient in plane so as to minimize the strain in the microdomain lattice, i.e. the commensurability between the post lattice and the equilibrium period L_o governs the self-assembly. For example, if $L_o = nL_x$ (with n an integer) then the microdomain lattice is commensurate with the L_x spacing and the cylinders are expected to orient along the *y*-axis with zero strain.

Fig. 2-10(c-t) shows templating using posts with a height of 19 nm and a diameter of 10 nm. By varying L_x from 29 nm to 72 nm with L_x/L_y = 1.15 and 1.5, we demonstrated every possible commensurate condition for the 18 nm period PS-b-PDMS, in which the orientation of the block copolymer cylinders could be varied between 0° and 90° with respect to the *x*-axis. The block copolymer cylinders formed an aligned linear pattern when the post arrays satisfied one of the commensurate conditions, exactly analogously

to the case of the 34 nm period block copolymer[7]. This result shows that an aligned linear pattern can be achieved by topographic post templates even for microdomains in the sub-10 nm regime. The final pattern achieved by topographic templates and a block copolymer can then be transferred into metal using previously demonstrated techniques[9].

To minimize the time required for template fabrication, it is desirable for the posts to be as sparse as possible. Fig. 2-10(k) shows good order even when the posts only occupy 5% of the final PDMS pattern, suggesting that this method of templated self-assembly can be considered as a method to increase the throughput of EBL by a factor of ~20. To decrease the density of the templates further, the posts can be replaced by well-spaced 'dashes' or fins which provide additional guidance to determine the in-plane orientation of the cylinders. Those results are given in 2.3.7 Appendix, which shows long-range ordered sub-10-nm block copolymer patterns guided by dash templates which occupied only 1/66 of the final pattern.

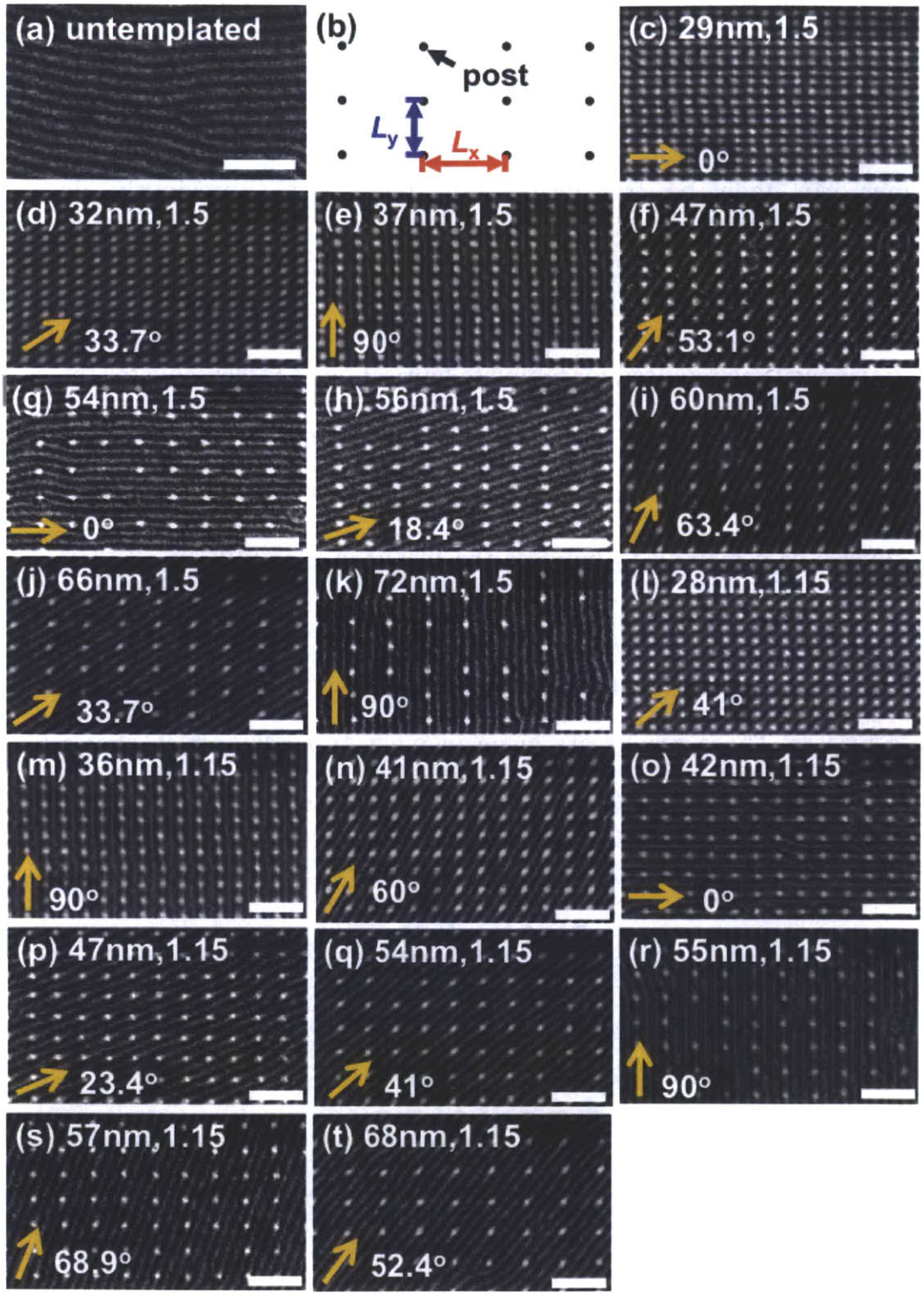

Figure 2-8. (a) SEM image of PDMS microdomains on a smooth substrate; (b) The definition of L_x and L_y of the post arrays; (c~t) SEM images of PDMS cylinders

templated by post arrays. The height of the posts was 19 nm and the diameter was 10 nm. Arrows indicate the direction of the PDMS cylinders. Each figure is annotated L_x, L_x/L_y. (c~k) L_x/L_y = 1.5 (l~t) L_x/L_y = 1.15. Scale bar = 100 nm.

2.3.2 Post diameter effect

We now consider the effects of post height and diameter on the templating process. Figure 2-9 illustrates how a block copolymer interacts with posts with a range of diameters, for L_x = 48 nm and L_y = 32 nm and a post height of 16 nm. The commensurate orientation of the 16 kg/mol PS-b-PDMS block copolymer cylinders for this array period is depicted in figure 2-9(a), giving a cylinder orientation of 53.1° with respect to the *x*-axis. At a height of 16 nm, posts with diameter ranging from 6.3 nm to 13.8 nm could be obtained; posts fell over when the aspect ratio was larger than ~3. Figure 2-9(b~g) shows the PDMS cylinders templated by posts with a range of diameters. As shown in figure 2-8(b), the PDMS cylinders were not aligned in a preferential orientation when templated by posts with a diameter of 6.3 nm, which is smaller than the width of the PDMS microdomain. However, the PDMS cylinders were aligned along the commensurate orientation (53.1°), when templated by posts with diameters comparable to the width of the PDMS microdomain, as shown in figure 2-9(c~f), although the PDMS cylinders lost long-range order and some fractions were aligned parallel to the *y*-axis, as shown in figure 2(g).

Figure 2-9(h) shows how the orientation of the block copolymer cylinders depended on the post diameter for a given post spacing. The distribution of cylinder orientations was found by a MATLAB image analysis program, which determined the area fractions of

cylinders oriented parallel to the y-axis (90°) and along the 53.1° commensurate orientation. The cylinders formed the expected commensurate orientation over >80% of the post lattice when the post diameter was in the range from 8 nm to 12 nm, which is comparable to the width of the PDMS microdomains. The maximum area fraction was achieved with a post diameter of 11 nm.

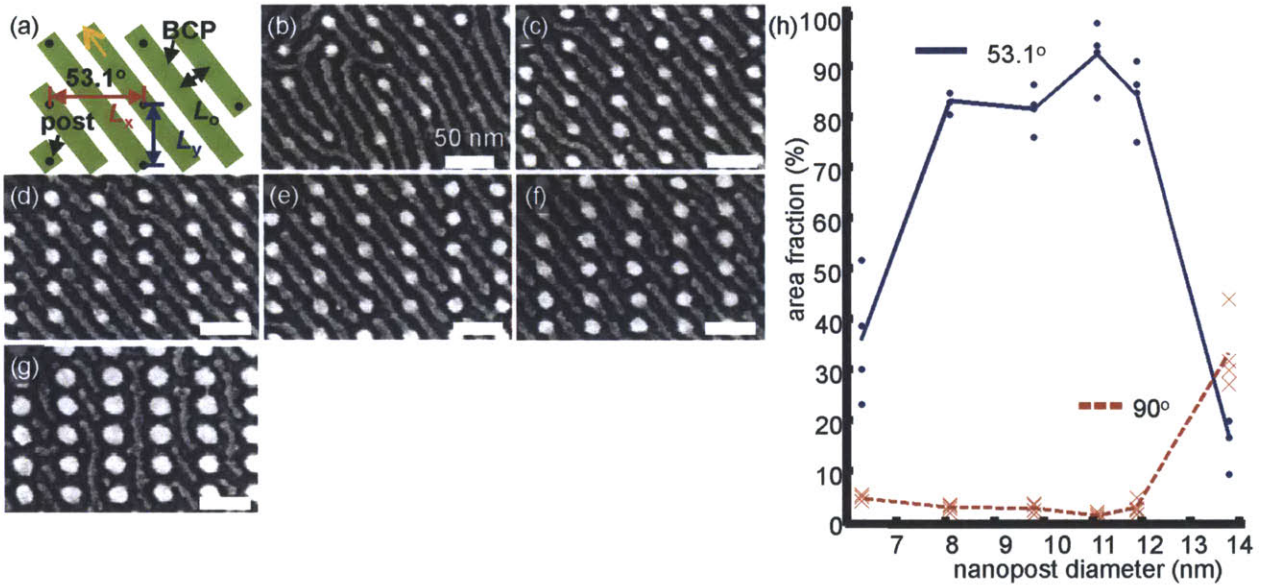

Figure 2-9. (a) The commensurate orientation for a post array with L_x = 48 nm and L_y = 32 nm. (b~g) PDMS microdomains templated by arrays with various post diameters with L_x = 48 nm and L_y = 32 nm and a post height of 16 nm. The diameter of posts was (b) 6.3 nm (c) 8.1 nm (d) 9.8 nm (e) 11.1 nm (f) 11.9 nm (g) 13.8 nm. Scale bar = 50 nm. (h) the area fraction of the cylinders oriented along the commensurate orientation and the fraction along the y-axis. (b~g) the samples were slightly overetched, which makes the PDMS cylinders disconnected.

When the post diameter was larger than 12 nm, the area fraction of the block copolymer cylinders oriented along the commensurate orientation decreased and the cylinders broke into shorter segments. Instead of aligning along the commensurate orientation, the block copolymer cylinders often lay along the larger gaps between the posts, parallel to the *y*-axis. The 12 nm diameter posts are wider than the equilibrium width of the cylindrical microdomain, leading to considerable distortion of the PDMS chains in the microdomain surrounding the post, which destabilizes the commensurate condition. Further information about how the orientation of PDMS cylinders changed depending on the post diameter is included in the Supporting Information.

2.3.3 Post height effect

Figure 2-10 shows how the block copolymer interacted with posts with a range of heights, 12 nm to 27 nm. The arrays had L_x of 48 nm and L_y of 32 nm, and a post diameter of 12 nm. The PDMS cylinders were not aligned when templated by posts with a height of 12 nm, as shown in figure 2-10(a). However, the PDMS cylinders were aligned and oriented along the commensurate orientation when templated by posts with a height of 16 nm, which is comparable to the equilibrium period of 16kg/mol PS-b-PDMS, as shown in figure 2-10(b). Figure 2-10(c~e) shows that the PDMS cylinders were oriented parallel to the *y*-axis when templated by posts taller than 19 nm. The area fractions in figure 2-10(f) were consistent with the above observations. A post height of 16 nm gave the highest fraction of the commensurate orientation, while taller posts promoted a *y*-axis orientation of the cylinders.

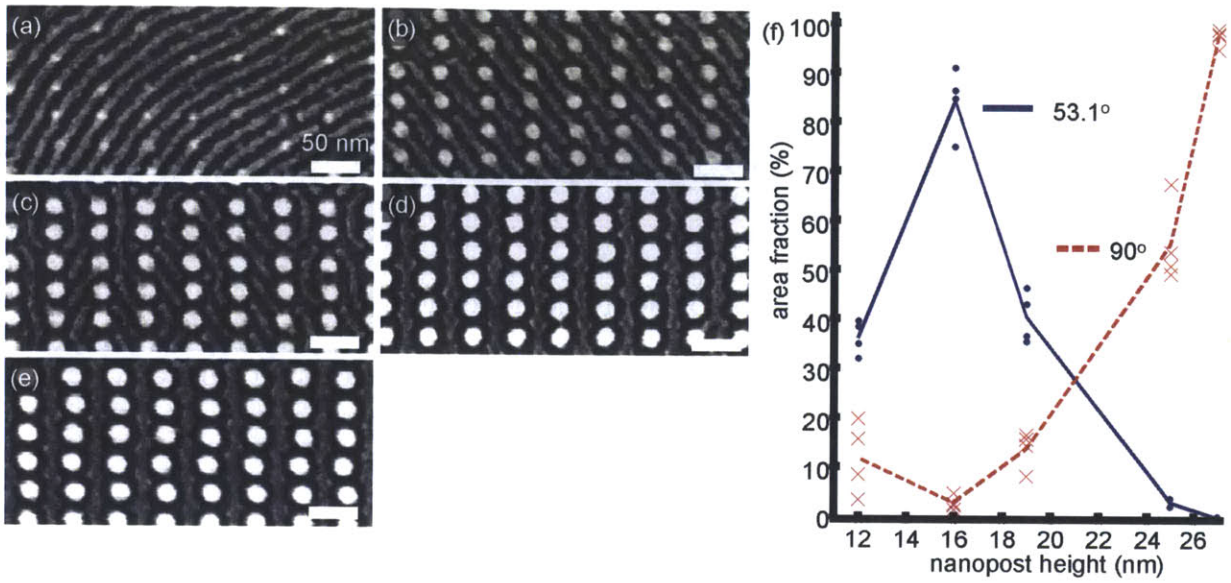

Figure 2-10. SEM images of PDMS microdomains templated by post arrays with various heights. L_x and L_y of the array was 48 nm and 32 nm respectively. The diameter of posts was 12 nm, and the height of posts was (a) 12 nm (b) 16 nm (c) 19 nm (d) 25 nm (e) 27 nm. Scale bar = 50 nm. (f) the area fractions of the cylinders oriented along the commensurate orientation and the *y*-axis. Each set of post height data came from a separate sample. (a~e) the samples were slightly overetched, which makes the PDMS cylinders disconnected.

2.3.4 SCFT simulation

To gain further insight into how PDMS microdomains interact with tall or short posts, we used self-consistent field theory (SCFT) simulation (collaboration with Adam F. Hannon, Professor Caroline A. Ross, and Prof. Alfredo Alexander-Katz). SCFT has been shown to agree with experimental results, and to predict 3D morphologies of block copolymers[92–94]. In the SCFT simulations, the volume fraction of PDMS f_{PDMS} = 0.33,

and $\chi N = 14.0$ where χ is the effective Flory-Huggins interaction parameter based on the equilibrium solvent uptake and $N = 69$ is the number of coarse-grained segments corresponding to a Kuhn monomer. For the experimental block copolymer, $\chi = 0.26$ at room temperature and $N = 174$, giving $\chi N = 45.2$. The details of the simulations are included in 2.3.4 Appendix. Since the simulation implicitly accounts for the solvent by using a lower effective χ and also coarse-grains the polymer by a factor of 2.5 in number of repeat units, the χN used in the model was much lower than the value based on the 0.26 bulk χ parameter and 174 degree of polymerization. Figure 2-13 shows the simulation result of block copolymer cylinders templated by posts with a range of heights, 12, 19 and 27 nm. The as-spun polymer film in the experiment was 24 nm thick, equivalent to $1.33L_o$. During the solvent annealing process, the polymer film swelled 1.6 times compared with the original film thickness. To simulate templated self-assembly during the solvent annealing process, the film thickness in the model was set as $2.11L_o$ to reflect the swelling of the film by the solvent. As in the experiment, the posts and substrate and the air interface of the film were attractive to the PDMS block, and the model shows PDMS wetting these surfaces.

The 12 nm post ($0.67L_o$) in the simulation led to the formation of a bicontinuous network of PDMS due to the periodic boundary conditions, implying that the cylinders could orient in either direction, as shown in figure 2-11(a,d,g). This structure is consistent with the experimental observation that the 12 nm posts did not induce long-range order because they were too short to make contact with the PDMS microdomains embedded in the PS matrix. Figure 2-11(b,e,h) shows the cylinders templated by posts with a height of 19 nm ($1.06L_o$). The PDMS cylinders were in contact with the PDMS-

coated posts, and were aligned along the commensurate orientation, with bulges corresponding to the post locations. However, when the height of posts was 27 nm ($1.5L_o$), the cylinders were not connected to the posts even though the posts had a layer of PDMS surrounding them, as shown in figure 2-11(c,f,i), and the cylinders lay along the larger gaps between the posts, as seen experimentally.

Figure 2-11(i) also shows why the diameter of posts in the SEM images of Figure 2-10 appeared different depending on the height of the posts, even though all posts were fabricated with the same electron dose. A thicker layer of PDMS from the block copolymer surrounded the taller posts, according to the simulations. The oxygen etching preserves the PDMS layer, making the final diameter of the posts larger than the as-fabricated HSQ posts.

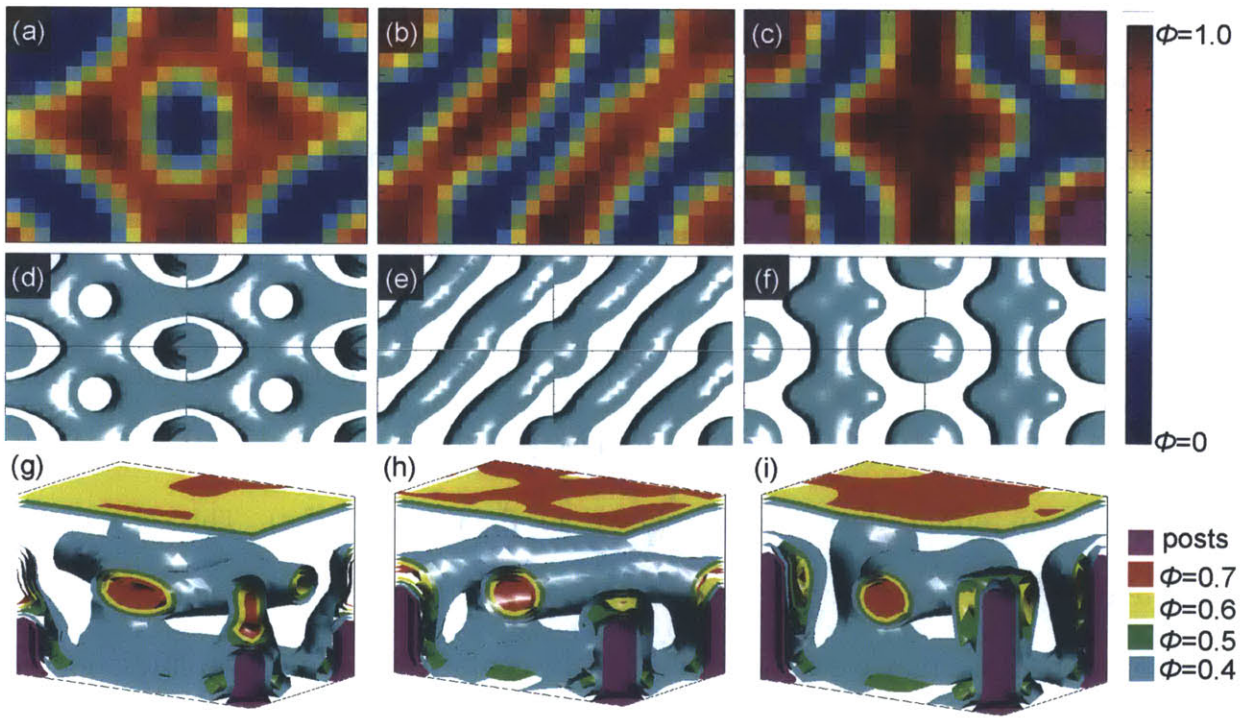

Figure 2-11. Unit-cell SCFT simulations of templated self-assembly of 16 kg/mol PS-b-PDMS modeled with $\chi N = 14.0$ and $f_{PDMS} = 0.33$ templated by posts with various heights. (a~c) cut-through cross-section 2D view at height of $1.11L_0$; (d~f) top-down view of 2x2 unit cells; (g~i) 3D view. In terms of L_0, the cell thicknesses are $2.11L_0$ corresponding to an evolving solvent annealing thickness of approximately 1.6 times the initial film thickness. The height of posts in terms of L_0 is (a,d,g) $0.67L_0$ (b,e,h) $1.06L_0$ (c,f,i) $1.50L_0$. These heights correspond to the respective heights in experiment of 12 nm, 19 nm, and 27 nm.

2.3.5 Area fraction depending on the post diameter and height.

The preceding results suggest that there is an optimum post height (~16 nm, similar to the height of the cylinders above the substrate) and diameter (~11 nm, similar to $L_0/2$ or the diameter of the cylinders) to obtain effective templating. To illustrate the window of post dimensions that provide the best templating, Figure 2-12 shows the area fraction of cylinders with commensurate orientation as a function of post height and diameter. The smaller posts gave poor templating while the larger diameter and height posts promoted a *y*-axis orientation, acting analogously to a topographical trench[9]. These results indicate the tolerance of the templating process to variations in post dimensions and provide guidelines for templating lower molecular weight block copolymers or complex structures using size-controlled orientation control within specific areas of the substrate.

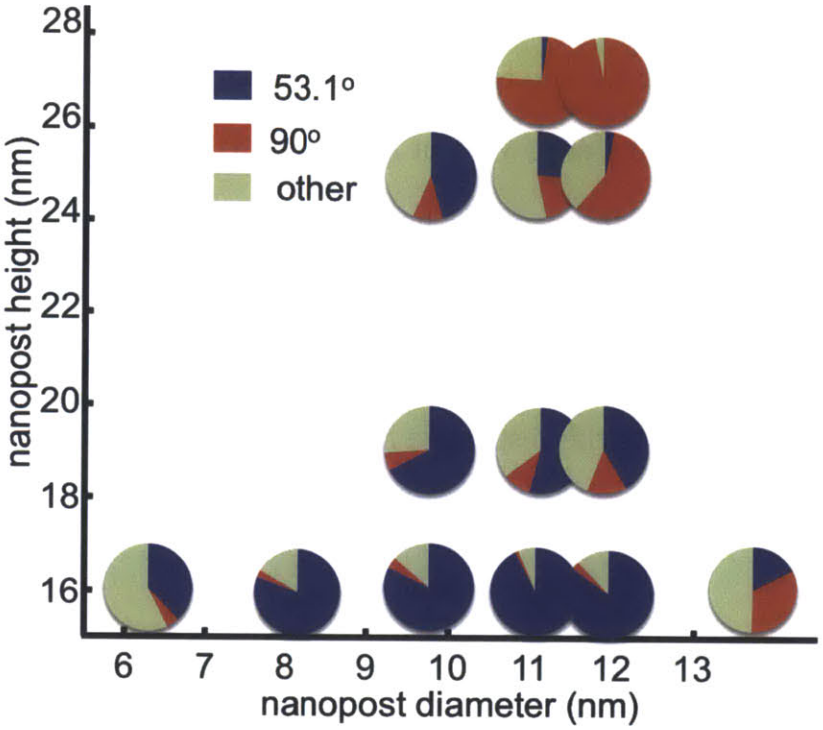

Figure 2-12. The change of area fraction of the block copolymer cylinders templated by various posts. (a) Pie charts show area fractions of the block copolymer cylinders oriented along the commensurate orientation (53.1°), the *y*-axis (90°), and other orientations.

2.3.6 Discussion

This work has shown that a cylindrical morphology PS-b-PDMS block copolymer with a period below 20 nm which forms microdomains with a diameter below 10 nm can be registered and oriented in plane using an array of functionalized topographic posts. Posts with a range of diameters and heights were fabricated from a high-contrast resist and a high-contrast development system, and their templating effects were tested. The diameter and the height of posts are major factors determining the interaction between the block copolymer cylinders and the posts and therefore the effectiveness of the

templating. The templating is optimized when the post diameter is similar to or smaller than the diameter of the cylindrical microdomains so that the distortion of the microdomains in contact with the posts is minimized, and when the height of the posts is similar to the height of the microdomains above the surface of the substrate. When templated by posts with appropriate diameter and height, the in-plane orientation of the cylinder array is determined by the commensurability between the post lattice and the equilibrium period, analogously to results on a 45.5 kg/mol PS-b-PDMS block copolymer with a larger period. In the optimized case the area fraction of the microdomains oriented along the commensurate orientation reached 92%. Short posts were ineffective at templating, while tall or wide posts promoted alignment of the cylinders along the *y*-axis, acting similarly to trenches[9]. Self-consistent field theory modeling illustrated the 3D arrangement of the microdomains and was in good agreement with the observations of post height effect. These findings enable an improved design of sparse topographic templates to direct the assembly of block copolymer patterns with a controlled in-plane orientation and sub-10-nm features. This suggests that templated self-assembly of block copolymers based on sparse topographic templates, formed for example by interference lithography followed by trimming down and replication by nanoimprint, could be used for fabricating sub-10-nm nanopatterns with high throughput.

2.3.7 Methods and area fraction analysis

Poly(styrene-block-dimethylsiloxane) (PS-b-PDMS) diblock copolymer was purchased from Polymer Source. The molecular weight of the block copolymer was 16 kg/mol with

polydispersity index of 1.08. The in-plane equilibrium spacing (L_o) of the block copolymer cylinders in a thin film after the PS matrix was removed by reactive ion etching was 18 nm. The hydroxyl-terminated PDMS brush (Mn = 0.8kg/mol, PDI ~1.10) was also purchased from Polymer Source. Hydrogen silsesquioxane (HSQ), a negative-tone electron-beam resist, was used for fabricating the topographic templates. 1% HSQ (XR-1521, solids) was purchased from Dow Corning.

HSQ films were spun coated to a thickness of 27 nm, 25 nm, 19 nm, 16 nm, and 12 nm by using spin speeds ranging from 1,000 rpm to 6,000 rpm on 3-inch silicon wafers. The thickness of the HSQ film was determined by ellipsometry. The HSQ coated silicon wafers were cleaved into 2 cm by 2 cm pieces. Single-pixel dots or short dashes (consisting of a short single-pass line) were exposed in a Raith 150 electron-beam lithography tool at 30 kV acceleration voltage. A range of post diameters was achieved from 6.5 nm to 15 nm by varying the electron dose. The samples were developed in a high-contrast developer system as described previously to remove unexposed resist and to reveal the topographic templates[91]. The sample was further treated with O_2/He plasma (50W, 10sec) to remove possible organic residues and to completely convert the HSQ structures into silicon oxide. Then, PDMS brush solution (1% in toluene) was spin coated on the substrate and thermally treated overnight at 170°C in vacuum. After the thermal treatment, residual brush molecules were removed by rinsing several times with toluene.

0.7 wt% of 16 kg/mol PS-b-PDMS dissolved in cyclohexane was spin-coated at 5000 rpm on PDMS brush coated template substrates. The block copolymer films were then exposed to solvent vapors using 1ml of acetone in a 9.3ml volume of glass chamber with

a controlled leak until complete evaporation of solvent. The annealing process took approximately 4 hrs. During the solvent annealing, the film swelled up to 1.5 times its original thickness and gradually relaxed as the solvent vapor pressure decreased[53]. To measure the thickness of films during solvent annealing, a Filmetrics F20-UV (Filmeterics, Inc.) instrument was used with a quartz window in the solvent annealing chamber. The annealed BCP films were first treated with a 2 sec, 50W, 10 mTorr CF_4 plasma and then a 12 sec, 50W, 6 mTorr O_2 plasma to remove first the PDMS surface layer and then the PS matrix to leave oxygen-plasma-modified PDMS cylinders on the substrate. The surface morphology was observed using a Raith 150 SEM operated with an acceleration voltage of 10 kV.

The relationship between L_x and L_y and throughput increase.

The throughput increase is a metric that describes how much of the final pattern consists of PDMS microdomains vs. posts made by electron beam lithography (EBL), i.e. the factor by which the block copolymer self-assembly can be considered to enhance the throughput of an EBL system, compared to writing the entire pattern using EBL. It is defined as the area of the final PDMS pattern divided by the area of the HSQ posts that were written. The throughput increase is proportional to L_x and L_y of the post array, i.e. inversely proportional to the density of the posts. As the post spacing increases it becomes more likely that multiple in-plane orientations of the cylinders will form because the difference in strain energy between competing orientations decreases[74]. This leads to formation of defects in the templated microdomain arrays, and limits the throughput increase which can be achieved by topographic templates. In Figure 2-10,

throughput increases of the order of 20 were demonstrated with the presence of a few defects per square μm under the annealing conditions used.

Dashes can be used to increase the throughput over 66-fold.

In the case when L_x was larger than 72 nm, only a fraction of cylinders aligned along the *y*-axis, which was the commensurate orientation for L_x of 72 nm. To prevent the cylinders from being oriented in unwanted orientations, a template consisting of an array of dashes (line segments) was used instead of posts. L_y of the array was fixed at 100 nm, and the length of the dashes was fixed at 60 nm.

When L_x was 18 nm, an array of dashes acted as trenches rather than topographic templates. As figure 2-13 shows, the cylinders aligned along the *x*-axis. When L_x was larger than 20 nm, the arrays acted as topographic templates and guided the cylinders along the *y*-axis. For dash-arrays with L_x of 708 nm, only 1/66 of the final pattern was fabricated by EBL.

To estimate the templating effect of the dash-arrays, the area fraction of the cylinders which made an angle between 80° and 90° with the *x*-axis was calculated by using an image-analysis program. If all angles between 0° and 90° were equally probable, the area fraction of cylinders oriented along an angle between 80° and 90° would be around 11.1%. As shown in appendix, the area fractions of cylinders oriented along the *y*-axis were higher than 50% for dash-arrays with a range of L_x of 85 nm to 756 nm. At some specific L_x, the area fractions reached 90%. To estimate how the commensurate conditions are applied to the dash-arrays, the deviation of L_x from the commensurate

condition for an orientation parallel to the y-axis was calculated. The commensurate condition for the orientation parallel to the y-axis is an integer multiple of the equilibrium period L_o (=18 nm). As shown in figure 2-13(f), the area fractions of the cylinders oriented along the y-axis decreased as L_x deviated from commensurability. This result implies that the y-axis orientation competes with other orientations when the L_x does not satisfy the commensurate condition for orientation parallel to the y-axis. Dash-arrays can increase the area fraction of the orientation parallel to the y-axis up to 90% when L_x satisfies the commensurate condition.

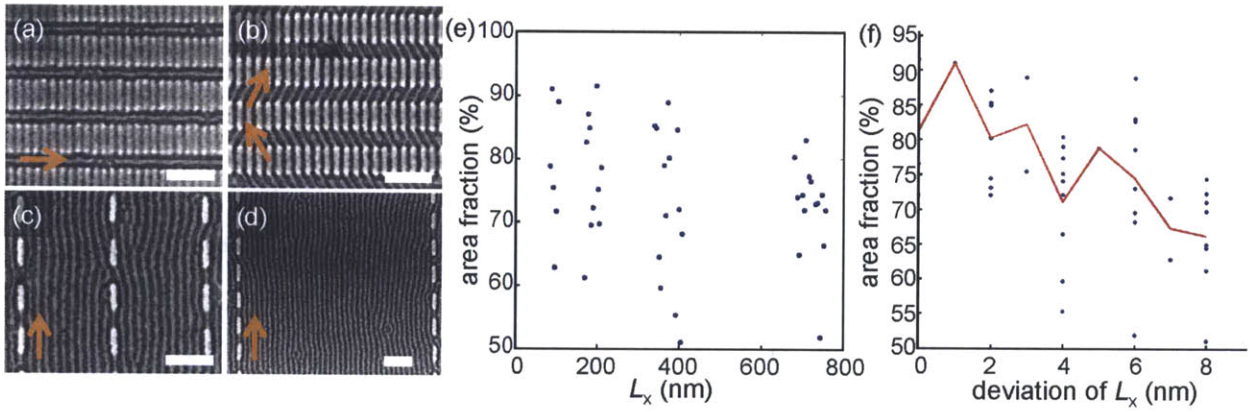

Figure 2-13. Block copolymers templated by dash-arrays. (a~d) Scanning electron micrograph images of PDMS microdomains templated by dash-arrays with various L_x. L_y was fixed at 100 nm and the length of each dash was fixed at 60 nm. L_x was (a) 18 nm (b) 21 nm (c) 198 nm (d) 708 nm. Scale bar = 100 nm. (e) Plot of the area fraction of PDMS oriented along the y-axis vs. the pitch of dashes. The area fraction was calculated by using an image-analysis program written in MATLAB. (f) Plot of the area fraction of PDMS cylinders oriented along the y-axis vs. the deviation of L_x from the commensurate condition for the orientation parallel to the y-axis. The commensurate condition for the

orientation parallel to the y-axis is an integer multiple of the equilibrium periodicity L_o (18 nm).

The area fraction distributions of the PDMS cylinders.

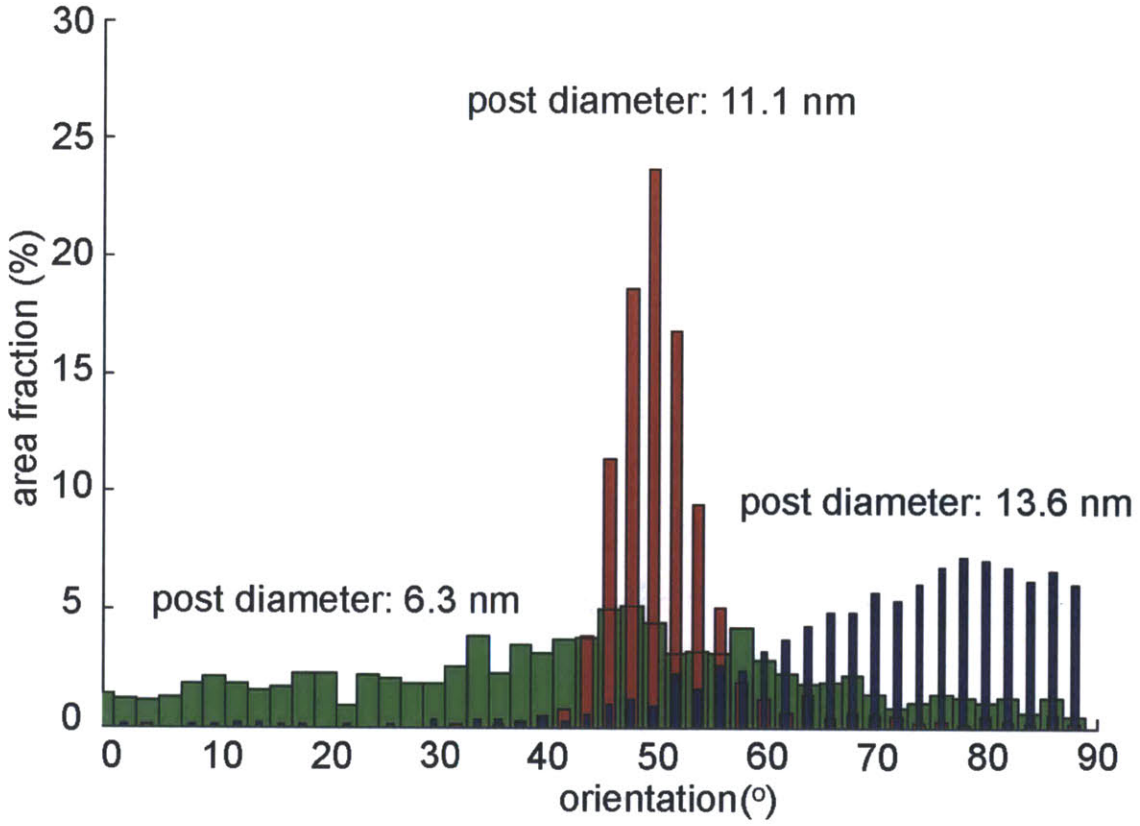

Figure 2-14. The area fraction distributions of the PDMS cylinders templated by posts with a height of 16 nm and a range of diameters as a function of in-plane orientation. The width of bars were adjusted to make all three area fraction distributions visible on the same axes. Post diameter is (green bars) 6.3 nm, (red bars) 11.1 nm, and (blue bars) 13.6 nm. Due to the distortion of the PDMS cylinders around the posts, the orientation of the PDMS cylinders can be measured with a few degrees error.

Figure 2-14 shows the area fraction distributions for PDMS cylinders as a function of the in plane orientation of the cylinders. The area fraction of the PDMS cylinders templated by posts with a diameter of 6.3 nm (green bars) is uniform over all the orientations, which means the PDMS cylinders were not aligned in a preferential orientation. This implies that posts with a diameter of 6.3 nm did not template the self-assembly of 16 kg/mol PS-b-PDMS. PDMS cylinders templated by posts with a diameter of 11.1 nm (red bars), which is similar to the diameter of the PDMS microdomains, were aligned in the commensurate orientation. However, PDMS cylinders oriented parallel to the *y*-axis when templated by posts with a diameter of 13.6 nm (blue bars).

SCFT simulation parameters

The SCFT simulations used to model the system uses the same formulation of the theory as presented in the supporting information section of Mickiewicz et. Al.[94] For the systems considered, the SCFT calculations were carried out on a 24X16X20 grid, volume fraction of the minority component f = 0.33, number of statistical segments in the chain used was 69 modeling the approximate number of Kuhn monomers in the real PS-b-PDMS system, and a χN = 14.0 modeling the reduced Flory-Huggins solubility parameter encountered in the solvent annealing. The cell dimensions were chosen to correspond to the real dimensions of a 48 nm by 32 nm post spacing with the thickness being selected as an intermediate thickness encountered during the solvent annealing. The natural polymer period L_0 corresponds to 9 grid points in the simulation grid. The simulations were run for 300,000 iterations to ensure the energy of the system was unchanging thus corresponding to an energy minimum structure. The posts, air

interface, and polymer brush layer were all modeled by constraining the fields to take on set values at the locations corresponding to those features with a large potential barrier to both the majority and minority block for the posts and substrate and an attractive potential to the minority block for the air interface and brush layer. A schematic showing these boundary conditions is shown in Figure S3. In addition to the topographical, chemical, and surface boundary conditions, the simulations used periodic boundary conditions in the X and Y directions, thus having the system be a unit cell in an infinitely periodic lattice.

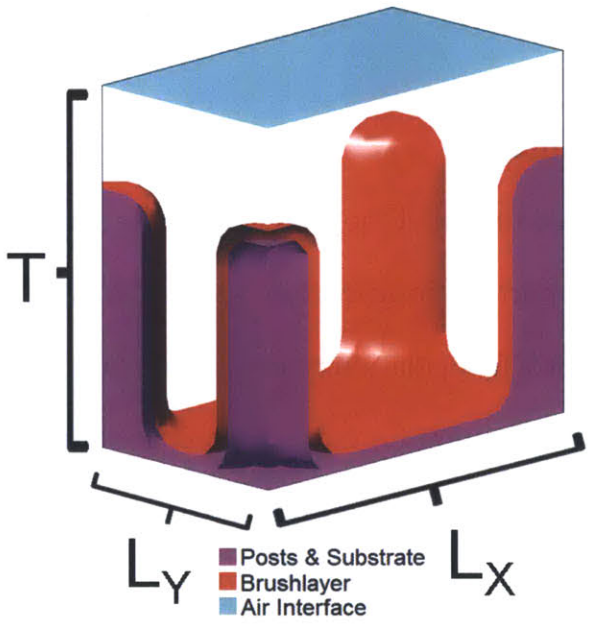

Figure 2-15. Schematic diagram showing the boundary conditions implemented in the SCFT simulations. The purple region represents the area where the fields were constrained to be a high potential barrier to both blocks of the polymer to model the posts and substrate, the red region represents the area were the fields were constrained to be attractive to the minority component to model the polymer brush layer, and the blue region represents the area where the fields were constrained to be attractive to the

minority component to model the lower surface energy PDMS has with air as observed in experiment. T is the cell thickness and L_X and L_Y are the post lattice dimensions.

2.4 Square array from a triblock terpolymer

In many applications, such as bit-patterned magnetic media, square array of dots is more useful than hexagonal array of dots. However, the spherical morphology block copolymer thin film generates dot arrays with square symmetry. Here, we demonstrate the dot arrays with hexagonal symmetry by using a triblock terpolymer.

2.4.1 Triblock terpolymer

Block copolymer self-assembly has been studied by many groups. Among many morphologies of block copolymers, parallel lines or close-packed dots have been heavily studied, because the parallel liens could be used for fabricating IC circuits and close-packed dots could be used for fabricating bit-patterned media. Recently, triblock terpolymers have been studied because it can produce more diverse and complex structures that cannot be achieved by using conventional diblock copoylemers[95–97]. The examples of such complex structures are ring-shape patterns[98] and square symmetry pattern[99]. Among these complex patterns, the dot patterns with square symmetry could be of interests because it could be useful in fabricating high density bit-patterned media[100] or via holes in integrated circuits. There have been many attempts to achieve a nanoscale dot patterns with square symmetry[24,101–104], but long-range ordered dot patterns with square symmetry have been difficult to achieve. So, here, we demonstrated the long-range ordered dot patterns with square symmetry by using polyisoprene-*block*-

polystyrene-*block*-polyferrocenylsilane (PI-*b*-PS-*b*-PFS) triblock terpolymer and topographic templates.

2.4.2 Templates for triblock terpolymer

The triblock film was made by mixing the PI-b-PS-b-PFS triblock terpolymer with 15% PS homopolymer and spin-coating on a smooth substrate. As shown in Figure 2-16, the self-assembled triblock terpolymer forms dot microdomains consisted of PFS and another dot microdomains consisted of PI. These two dot microdomains are embedded in the PS matrix. As two dot microdomains are formed from the self-assembly film, the two microdomains form a hexagonal array, as shown in Figure 2-18. However, we can selectively remove the PS matrix and PI dot microdomain by using reactive ion etching. As a result, we can achieve a square array of PFS microdomain on a substrate.

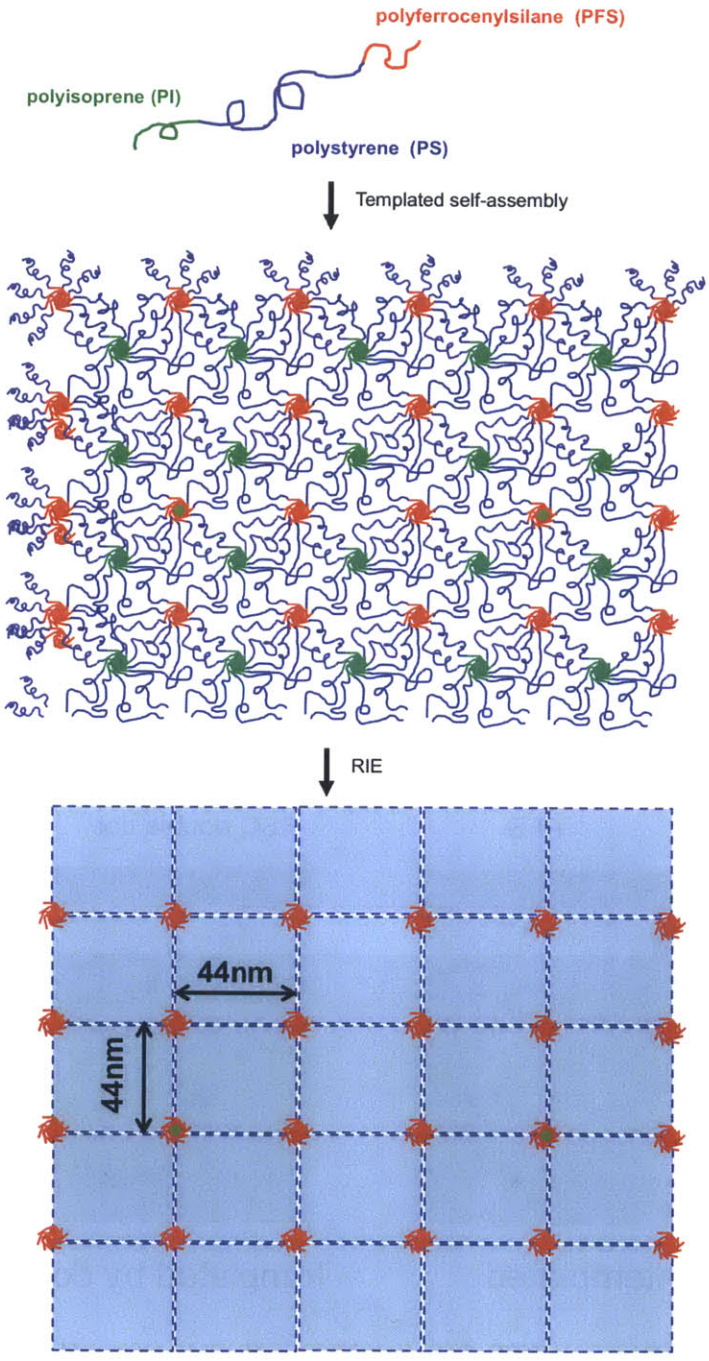

Figure 2-16. Schematics of the perpendicular orientation of alternating cylinders with square symmetry in an ABC triblock terpolymer film using solvent annealing.

Figure 2-17(A) shows the PFS microdomains after the PI microdomains and PS matrix were removed by RIE. The PFS microdomains made many grains with different

orientations. To achieve a long-range ordered PFS microdomains, we fabricated topographic post arrays by using electron-beam exposure of HSQ. As shown in Figure 2-19(b), the array consisted of double posts with a spacing between the two posts of the double post was 44 nm, which is equal to the natural periodicity of the PFS microdomains. The distances between the double posts were 88 nm along the x-axis and 132 nm along the *y*-axis. The height of the posts was 25 nm and the diameter was around 10 nm. The post sidewalls were coated with a PFS brush and the surface of the substrate was coated with a PEO brush. As shown in Figure 2-17(b), the triblock terpolymer film assembled on the patterned substrate showed a long-range ordered PFS microdomains after the RIE.

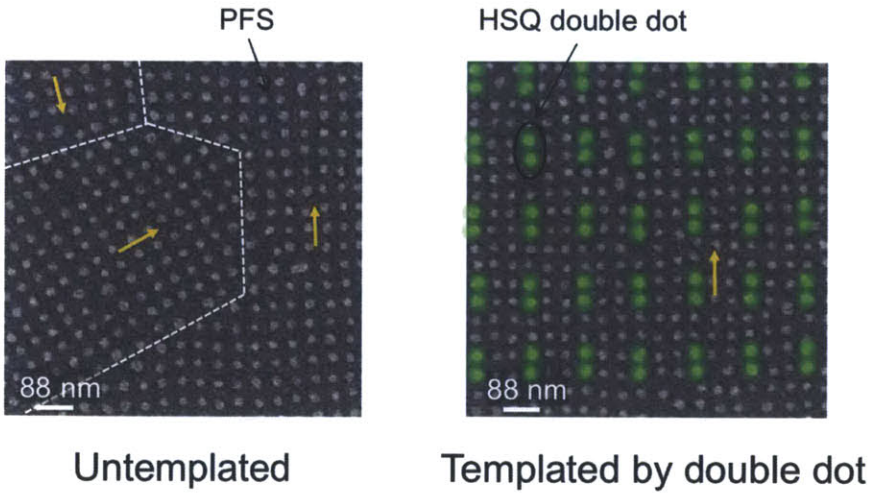

Figure 2-17. (a) SEM image PFS dots on a smooth substrate. (b) SEM image of PFS dots templated by topographic post arrays. The spacing between two dots of the double post was 44 nm. The substrate was functionalized with a PEO brush layer and the post sidewalls were coated with PFS brush layer.

2.5 Mixed morphology

Integrate circuit layout consists of lines and dots. However, the pattern generated by spherical morphology block copolymers or cylindrical morphology block copolymers can have only one morphology. Here, we demonstrate the fabrication of dot-line hybrid structures by using e-beam induced cross-linking.

2.5.1 Two morphologies on one substrate

Templated block copolymer(BCP) self-assembly is attractive for fabricating few-nanometer scale structures at high throughput. It has been used to fabricate various devices and applications, such as nanocrystal flash memories, nanowire transistors, and patterned magnetic-recording media. On an unpatterned substrate, block copolymer self-assembly generates dense arrays of lines or dots without long-range order[39,74,75,77,105]. To impose this long-range order, topographic templates or chemical template have been used. However, the limitation of the block copolymers self-assembly to be used in more diverse industrial applications is, the morphology of the resulting pattern is limited only to simple patterns, such as an array of dots patterns or lines. The morphology of the resulting patterns is decided by the volume fraction of the block copolymers. Also, the periodicity of the resulting pattern is decided by the molecular weight of the block copolymers. There has been a study of controlling the morphology and natural periodicity of the pattern by controlling the annealing condition of the block copolymer[91] or by straining the block copolymer pattern with incommensurate template[80,106]. However, achieving two different morphologies on a single substrate or one morphology with two different periodicities on a single substrate have not been achieved.

2.5.2 E-beam induced crosslinking

Here we present a method for achieving two different morphologies on a single substrate by cross-linking a solvent-annealed block copolymer film using electron-beam irradiation and performing a second solvent annealing process. By using this method, we achieved a sub-10-nm dot and line patterns on a single substrate. As shown in Figure 2-18, the morphology of 16 kg/mol PS-b-PDMS block copolymer can be tuned by using two solvents: (1) DMF; and (2) Acetone. A solvent-annealing with DMF vapor yields spherical morphology PDMS microdomains and a solvent-annealing with acetone vapor yields cylindrical morphology PDMS microdomains. The block copolymer chains in the solvent-annealed block copolymer film can be treated with a second solvent annealing process to change the morphology of the block copolymer microdomains from spherical to cylinder or from cylinder to spherical. We used electron-beam irradiation to cross-link the polymer chain in the self-assembled block copolymer film after the first solvent-annealing process. When the polymer chains were cross-linked, the polymer chains cannot move during the second annealing process and the pattern formed at the first annealing process were maintained after the second annealing process.

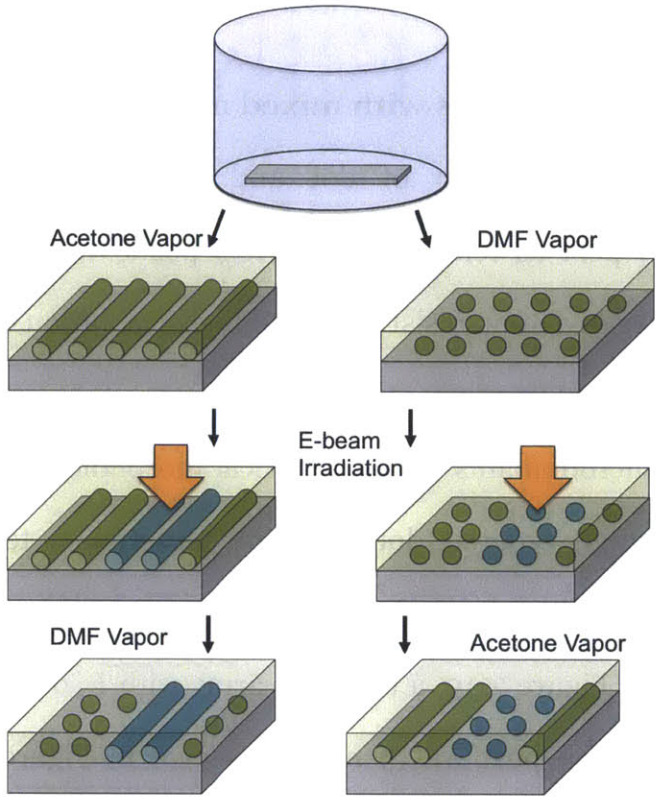

Figure 2-18. Schematics of the formation of dual morphologies in PS-**b**-PDMS block copolymer thin films resulting from solvent annealing, electron-beam irradiation, and a subsequent solvent anneal. The PS-**b**-PDMS film forms a cylinder morphology in acetone and spheres in DMF vapor. After a first anneal the films were selectively irradiated with a electron-beam to crosslink a region of the film, and then annealed in the other solvent to change the morphology in the unirradiated regions. The orientation of the sphere or cylinder array is determined by a topographical template (not shown) enabling the electron beam irradiation to be aligned with the microdomain orientation, though not with a specific microdomain[53]. Redrawn from Ref. 53.

2.5.3 Block copolymer patterns with mixed morphology

We demonstrated a combination of dot and line patterns by using hydrogen silsesquioxane (HSQ) post as template. The HSQ posts were fabricated by electron-beam exposure of a negative tone resist HSQ and high-resolution development system[58]. HSQ posts have been used in many studies to achieve a long-range ordered spherical morphology PDMS microdomains[6] and cylindrical morphology PDMS microdomains[7]. To achieve a long-range ordered dot and line patterns, a template array that is commensurate with both morphologies: spherical morphology and cylindrical morphology. As shown Figure 2-19, a template array with L_x of 45 and L_y of 78 nm was used. The diameter of the post was 9 nm. As shown in Figure 2-21, the cylindrical morphology PDMS microdomains were aligned along a diagonal orientation and the spherical morphology PDMS microdomains were also closely-packed.

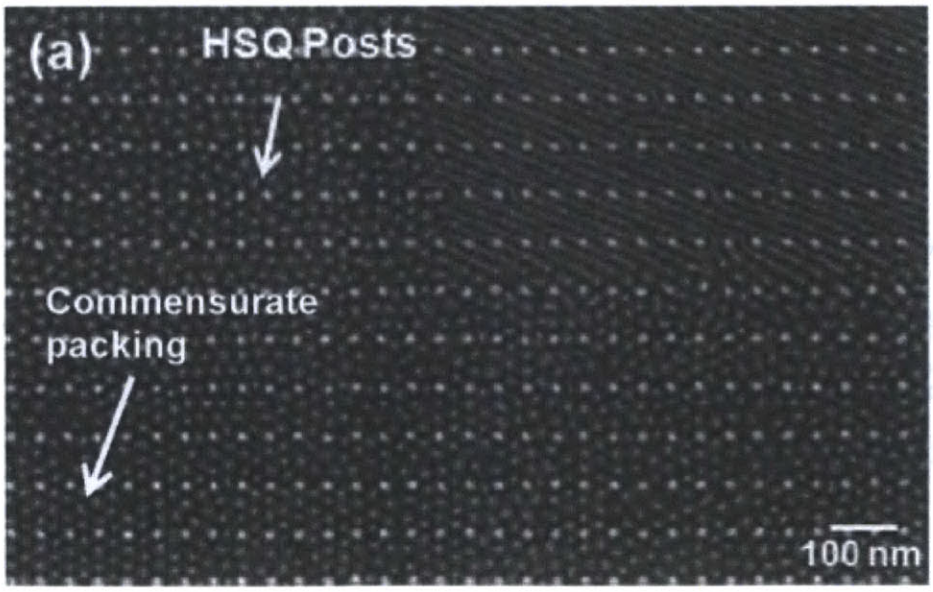

Figure 2-19. Dual phase patterns combined with post templating. SEM images of dual

phase block copolymer patterns combined with post templates with a period of 45 nm x 78 nm, commensurate with cylinders angled at 23° to the post lattice and a 26 nm center-to-center sphere array aligned along the y axis[53].

3. Tile-Based Directed Self-assembly of Block-Copolymers

Directed self-assembly of block copolymers has been used for fabricating various nanoscale patterns, ranging from periodic lines to simple bends. However, assemblies of dense bends, junctions, and line segments in a single pattern have not been achieved by using sparse templates, because no systematic template-design methods for achieving such complex patterns existed. To direct a complex pattern by using a sparse template, the template needs to encode the key information contained in the final pattern, without being a simple copy of the pattern. Here we develop a set of topographic template tiles consisting of square lattices of posts with a restricted range of geometric features. The block-copolymer patterns resulting from all tile arrangements are determined. By combining tiles in different ways, it is possible to predict a relatively simple template that will direct the formation of non-trivial block-copolymer patterns, providing a new template design method for a complex block-copolymer pattern.

3.1 Introduction

The self-assembly of block-copolymer thin films can generate dense nanoscale patterns over large areas[55,77,78,105,107–110]. When directed by a sparse topographic or chemical template, the block copolymers self-assemble into long-range ordered patterns with a controlled orientation[7,36,46,52,86,90,111–113]. These aligned patterns have been used as lithographic masks to fabricate devices including patterned magnetic recording media,

flash memory, and nanowire or graphene ribbon transistors[64,81–83,114–117]. Aperiodic templates are necessary to fabricate patterns consisting of combinations of bends, line segments and junctions using block copolymer directed self-assembly. Stoykovich et al. and Liu and et al. have shown that an array of jogs, bends or T-junctions and an isolated jog can be formed from a self-assembled polystyrene-*b*-polymethylmethacrylate (PS-*b*-PMMA) block copolymer with lamellar-morphology on a chemical template[36,118]. We have shown previously that a polystyrene-*b*-polydimethylsiloxane (PS-*b*-PDMS) block copolymer with cylindrical-morphology can be directed to form an array of bends by using a topographic template[7]. These approaches rely on the intuitive design of templates that contain features with similar density and arrangement to the features in the target pattern and produce relatively simple and periodic patterns. Recently, we theoretically designed templates for directed self-assembly using a Monte Carlo algorithm to move posts randomly within the simulation cell until the free energy is minimized. By using this method, a template for an array of junctions was predicted[119], but the template features were not constrained to have any predetermined spacing or location. What is missing in these three approaches is the ability to template patterns over a large area that contain complex assemblies of dense bends, terminations, and junctions directed by a simple (and therefore, more easily manufacturable) template.

The key advantages of using templated self-assembly of block copolymers are resolution enhancement and additionally and increase in throughput. In terms of the resolution enhancement, there have been many studies on fabricating long-range ordered block copolymer patterns by using low-resolution templates such as micron-scale trenches (e.g. Jung et. al. Nano Lett. 2010). There have been also a few studies on achieving an

array of bends and junctions by using low-resolution templates. However, to achieve isolated jogs, a same-resolution template was used (e.g. Liu et. al. Adv. Func. Mater 2010), as we report in this work. In general as the information content of the pattern increases, one would expect the template information content will also need to increase, so that one would not expect to direct e.g. an isolated bend in a block copolymer line surrounded by line terminations by using a micron scale trench.

In this work, we showed that the throughput can be increased by ~5-fold by fabricating only a small fraction of the final pattern and having the block copolymer fill in the rest according to the rules we established. This would be the minimum throughput enhancement; if the pattern contains regions of e.g. parallel lines then simpler templates could be used in those regions. One only needs the approach described here for regions where various features need to be placed in proximity in a non-trivial pattern. For faster fabrication of the template, a massively parallel technique could be used to fabricate a square lattice of posts and a serial technique to add double posts where required.

3.2 Development of rules for a square-grid template

We present a general and modular approach to designing and fabricating dense and complex block-copolymer patterns by developing block-copolymer assembly rules for square template tiles and joining the tiles together in a mosaic to form a desired target pattern. The template tiles consisted of a restricted set of post motifs. By limiting the number of possible post motifs, we study both experimentally and through simulations

the block-copolymer patterns and defects generated from all tile combinations as well as interactions between the tiles. Based on these results, we develop a set of template design tiling rules for our system that can be used for designing a template to achieve a given target pattern.

We first demonstrate that the orientation of block-copolymer cylinders can be restricted to two orthogonal in-plane directions by using a square lattice of topographic features. Square lattices of topographic single posts with a pitch of 39 nm were fabricated by means of electron-beam lithography. Next, the substrates and posts were chemically functionalized with hydroxyl-terminated PDMS[57]. A PS-*b*-PDMS block copolymer with cylindrical-morphology was spin-coated onto the substrate, and then solvent-annealed and finally etched to yield oxidized PDMS cylinders. On an unpatterned substrate, the observed equilibrium periodicity of the PDMS cylinders (L_o) was ~39 ± 2 nm. Figure 3-1 shows PDMS cylinders formed on a substrate with a single-post array which had a periodicity of L_o (39 nm). Figure 3-1b,c show scanning electron microscopy (SEM) images of the 39-nm-periodicity post array and the PDMS cylinders templated by this post array. As shown in Figure 3-1c, the block copolymer pattern templated by an array of single posts consisted of many grains (regions of parallel cylinders). The grains were degenerately aligned parallel either to the x-axis or to the y-axis, since both orientations were equally probable and both directions were commensurate orientations. Bends and terminations formed where two grains with different orientations met. The position of the bends or terminations was random, because the size of the grains was not uniform and also the center positions of the grains were not evenly spaced. As the templates occupy only a small fraction of the final pattern, fabricating the square lattice of posts

instead of the complete pattern of lines would increase the throughput of the lithography process, provided the positions of the bends and terminations can be controlled.

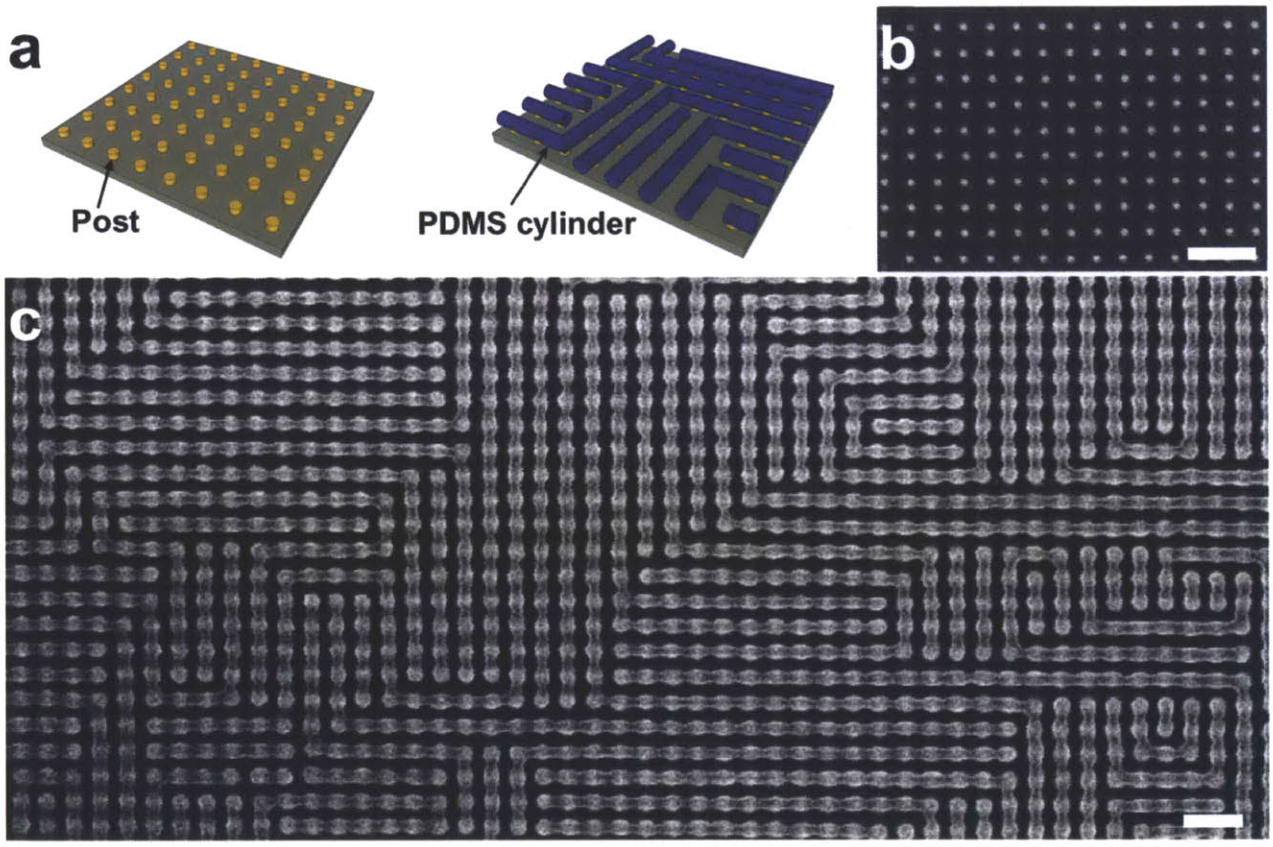

Figure 3-1: PDMS cylinders templated by a square array of posts. **a**, Three-dimensional schematic diagram showing how the PDMS cylinders were self-assembled on the post array. **b**, SEM image of a square array of posts with a periodicity of 39 nm. The height of the post was 28 ± 1 nm and the diameter was 10 ± 1 nm. **c**, SEM image of the PDMS cylinders templated by the post array in **b**. Since the pitch of the template was commensurate with the block copolymer, two orientations (parallel to the x-axis and to the y-axis) were degenerate and equally probable. Bends or terminations formed where the orientation of the PDMS cylinder changes. Scale bars: 100 nm.

To control the positions of the bends and terminations, we introduced double posts to the square array of single posts. In previous work, double posts were shown to promote block copolymer cylinders to align parallel to the direction of the double posts[7]. By replacing a single post in the array with a double post, we can locally break the degeneracy of the square array. We replaced one out of every nine single posts with a double post (Figure 3-2a). We defined the resulting 3×3 post array consisting of eight single posts and one double post at the center as a tile. As a result, a large square array of single and double posts shown in Figure 3-2a can be regarded as a checkerboard of tiles. However, the post array can be described equivalently by using another cell, defined as a design cell. As shown in Figure 3-2a and the inset of Figure 3-2a, a design cell consists of four single posts at the center and four double posts and eight single posts at the boundary. Because the single and double posts at the boundary are shared with the neighbor design cells, one design cell consists of eight single posts and one double post. Unlike a tile, the block copolymer cylinders formed on the single posts in the design cell (colored region in the inset of Figure 3-2a) are primarily templated by the four double posts at its boundary. So, the block copolymer pattern of a design cell is primarily determined by the orientations of the surrounding four double posts. The periodicity of the post template defines the periodicity of the final block copolymer pattern, and can be altered slightly (~+/- 10%) from L_0 while still effectively templating the block copolymer.

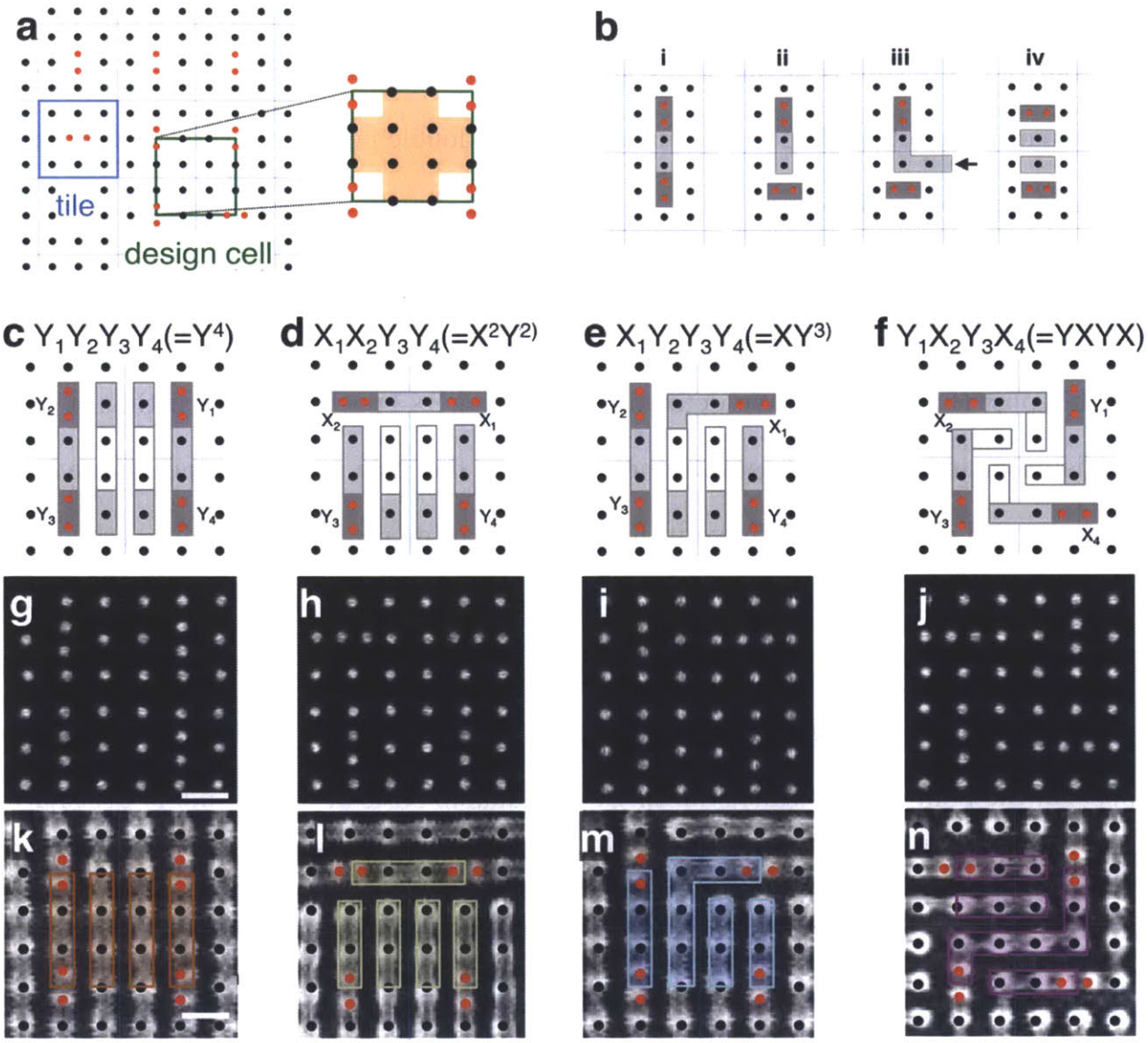

Figure 3-2: PDMS cylinders templated by a square array of posts. **a**, Schematic diagram showing templates used in this study. Black dots represent single posts and pairs of red dots represent double posts. The blue box represents a tile and green box represents a design cell. PDMS cylinders formed in a colored region would be primarily templated by the surrounding four double posts. **b**, Schematic diagrams showing how PDMS-cylinder patterns on single posts vary depending on the orientations of the closest two double posts. Dark-gray rectangles are the PDMS cylinders assembled on

double posts and light-gray rectangles are the PDMS cylinders assembled on single posts. In iii, an arrow represents a PDMS cylinder coming from a neighboring post. **c-f**, Predicted block-copolymer patterns of the four different arrangements of a design cell. White rectangles represent predicted block-copolymer patterns on four single posts at the center of a design cell. **g-j**, SEM images of the templates of the four arrangements. **k-n**, SEM images of the most frequently observed block-copolymer patterns formed on the four arrangements. Different colors were used to distinguish the block-copolymer patterns from different design-cell arrangements. Scale bars: 50 nm.

To gain insight into how the PDMS-cylinder pattern on a single post in a design cell varies depending on the orientations of the surrounding four double posts, we first studied PDMS cylinders in between two double posts. As shown in Figure 3-2b, the PDMS cylinder connected the double posts via the two single posts when the double posts were parallel (Figure 3-2b-i). The PDMS cylinders made a termination when the two double posts were perpendicular to each other (Figure 3-2b-ii). However, the PDMS cylinders formed a bend at the single posts instead when another cylinder from a neighboring post (indicated by an arrow in Figure 3-2b-iii) came into the structure (Figure 3-2b-iii). When the double posts were aligned parallel to each other in the orthogonal in-plane direction, the PDMS cylinders aligned parallel to the double posts (Figure 3-2b-iv).

By applying the four general observations mentioned above, we predicted the block-copolymer pattern templated by each design-cell arrangement. Each double post can be aligned along one of two directions with 16 (2^4) possible combinations of the

orientations of the four double posts in the design cell. The 16 combinations can be grouped into just four arrangements that are not equivalent under 90° rotations or mirror transformations. Figure 3-2c-f show the four arrangements and the predicted block-copolymer patterns based on the rules described in Figure 3-2b. We introduced a notation $X_1X_2Y_3Y_4$, in which the 1st, 2nd, 3rd, and 4th letters represent the orientation of the double post in the upper right, upper left, lower left, and lower right quadrant respectively. For a $Y_1Y_2Y_3Y_4$ (=Y^4) arrangement (Figure 3-2c), the light-gray rectangles connecting dark-gray rectangles on the Y_1 and Y_4 double posts, and the Y_2 and Y_3 double posts were predicted based on the observation in Figure 3-2b-i. Light-gray rectangles on the single posts between the Y_1 and Y_2 double posts, and the Y_3 and Y_4 double posts were predicted based on Figure 3-2b-iv. After that, white rectangles on the four single posts at the center of the design cell were predicted to align parallel to the surrounding block-copolymer patterns (dark- and light-gray rectangles). For the other three arrangements, the block-copolymer patterns were predicted based on the observations in Figure 3-2b-i,ii,iv for an $X_1X_2Y_3Y_4$ (=X^2Y^2) arrangement (Figure 3-2d), Figure 3-2b-i,ii,iii,iv for a $X_1Y_2Y_3Y_4$ (=XY^3) arrangement (Figure 3-2e), and Figure 3-2b-iii for an $Y_1X_2Y_3X_4$ (=YXYX) arrangement (Figure 3-2f). In these three arrangements, the patterns on the four single posts at the center of each design cell were predicted to align parallel to the surrounding block-copolymer patterns.

When a block-copolymer film was annealed with these four design-cell arrangements, the PDMS cylinders formed various patterns on each arrangement. Figure 3-2k-n show SEM images of the most frequently observed patterns formed on the four arrangements. For $Y_1Y_2Y_3Y_4$ (=Y^4), $X_1X_2Y_3Y_4$ (=X^2Y^2), and $X_1Y_2Y_3Y_4$ (=XY^3) arrangements, the most

frequently observed patterns were identical to the predicted patterns shown in Figure 3-2c-e. However, for an $Y_1X_2Y_3X_4$ (=YXYX) arrangement, the predicted pattern in Figure 3-2f was not observed. Instead, another pattern shown in Figure 3-2n was observed with a low reproducibility (<20%) (Figure 3-6).

3.3 Prediction of block copolymer patterns formed on a given templat

To show that the patterns in Figure 3-2k-n can be used for predicting the block-copolymer pattern formed on a large-area-template, we fabricated a square array template of single and double posts and checked whether the final PDMS pattern agreed with the predictions. Figure 3-3a shows the test template layout in which the orientations of the double posts in the layout were random. The design cells having Y^4, X^2Y^2, XY^3, and YXYX arrangements were predicted based on the patterns in Figure 3-2k-n, as shown in Figure 3-3a. When the predicted patterns from two neighboring design cells conflicted, the pattern was determined by the basic observations shown in Figure 3-2b (Figure 3-7). Figure 3-3b shows a SEM image of the template and Figure 3-3c shows the PDMS patterns directed by the template of Figure 3-3b. To quantify the accuracy of the prediction, we introduced the design cell prediction yield $D_{Y\%}$. $D_{Y\%}$ was defined as the ratio of the number of completely matched design cells to the total number of design cells. To quantify the degree of similarity between the predicted pattern and observed pattern, we introduced the grid prediction yield $G_{Y\%}$. $G_{Y\%}$ was defined as the ratio of the number of matched features on individual grid points to the total number of grid points (Figure 3-8). When the predicted pattern was compared with the block-copolymer pattern, $G_{Y\%}$ = 97% (467/480) (more typically $G_{Y\%} \approx$ 90%) and

$D_{Y\%}$ = 76% (19/25), as shown in Figure 3-3d. Red circles and ellipsoid indicate mismatches between the prediction and experimental result.

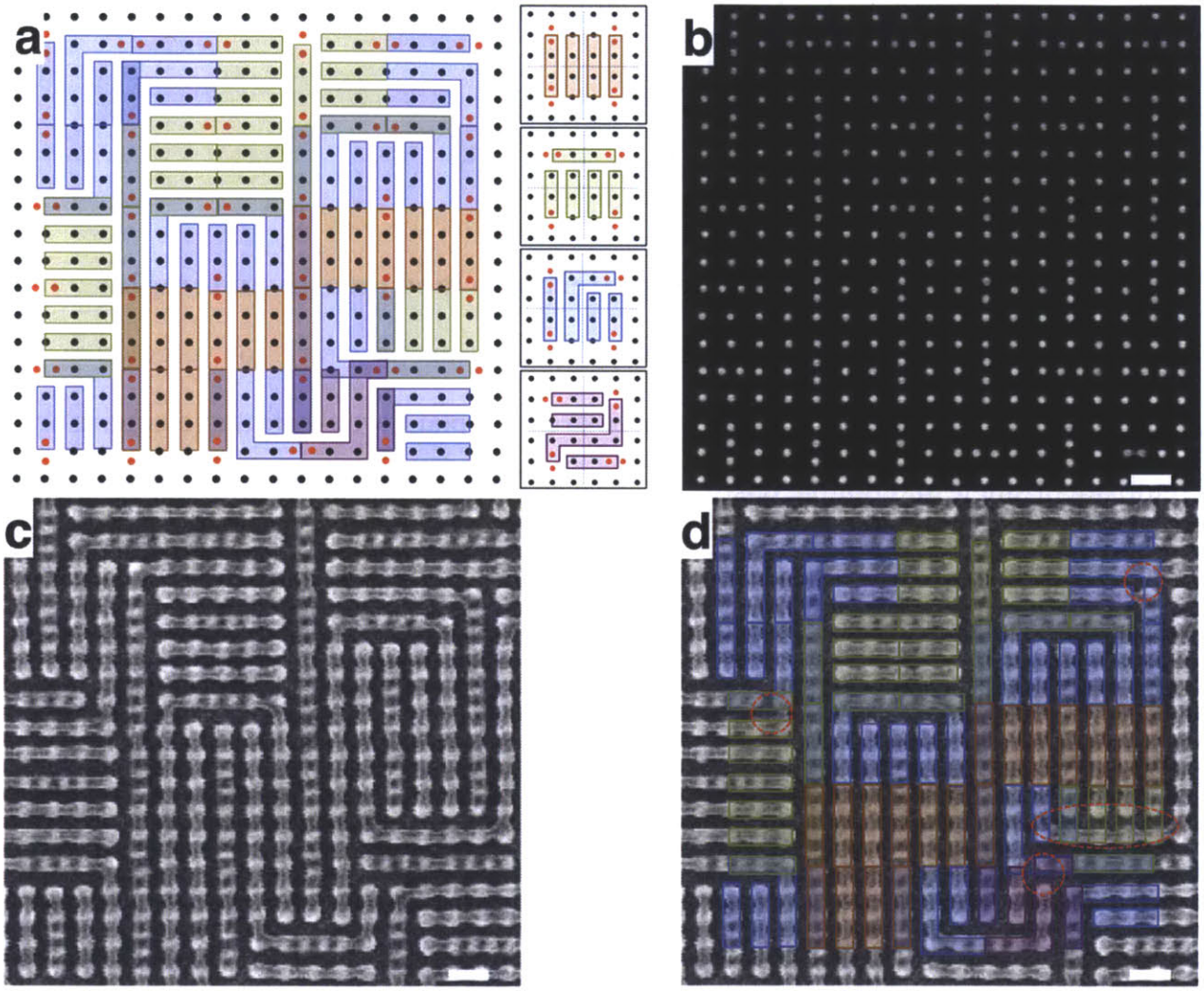

Figure 3-3: Prediction of the PDMS patterns directed by a template with random double-dot orientations and an experimental result. **a**, Random template and the predicted patterns. Insets show the block copolymer patterns of the four design-cell arrangements used for the prediction. **b**, SEM image of the fabricated template. **c**, SEM image of the PDMS cylinders formed on the template shown in **b**. **d**, The predicted pattern overlaid on the SEM image of the PDMS cylinders. Red circles and ellipsoid indicate mismatches between the prediction and experimental result. Scale bars: 50 nm.

3.4 Template design to achieve a target pattern

To demonstrate that complex target patterns can be templated by applying appropriate design rules, we fabricated two complex patterns consisting of many bends and terminations. Figure 3-4a,b show the template layouts and the block copolymer patterns predicted to form on these templates. Figure 3-4c,d show SEM images of the templates and Figure 3-4e,f show the PDMS patterns directed by the templates. Here $G_{Y\%}$ = 97% (Figure 3-4e) and 99% (Figure 3-4f). Furthermore, as shown in Figure 3-4g,h, self-consistent field theory (SCFT) simulations[92,94,120–122] were used to calculate the block copolymer morphology resulting from the input templates of Figure 3-4a and 3-4b. There is a very good agreement between the structure predicted from the empirically-derived design rules, the structure predicted by SCFT, and the structure observed in the experiments.

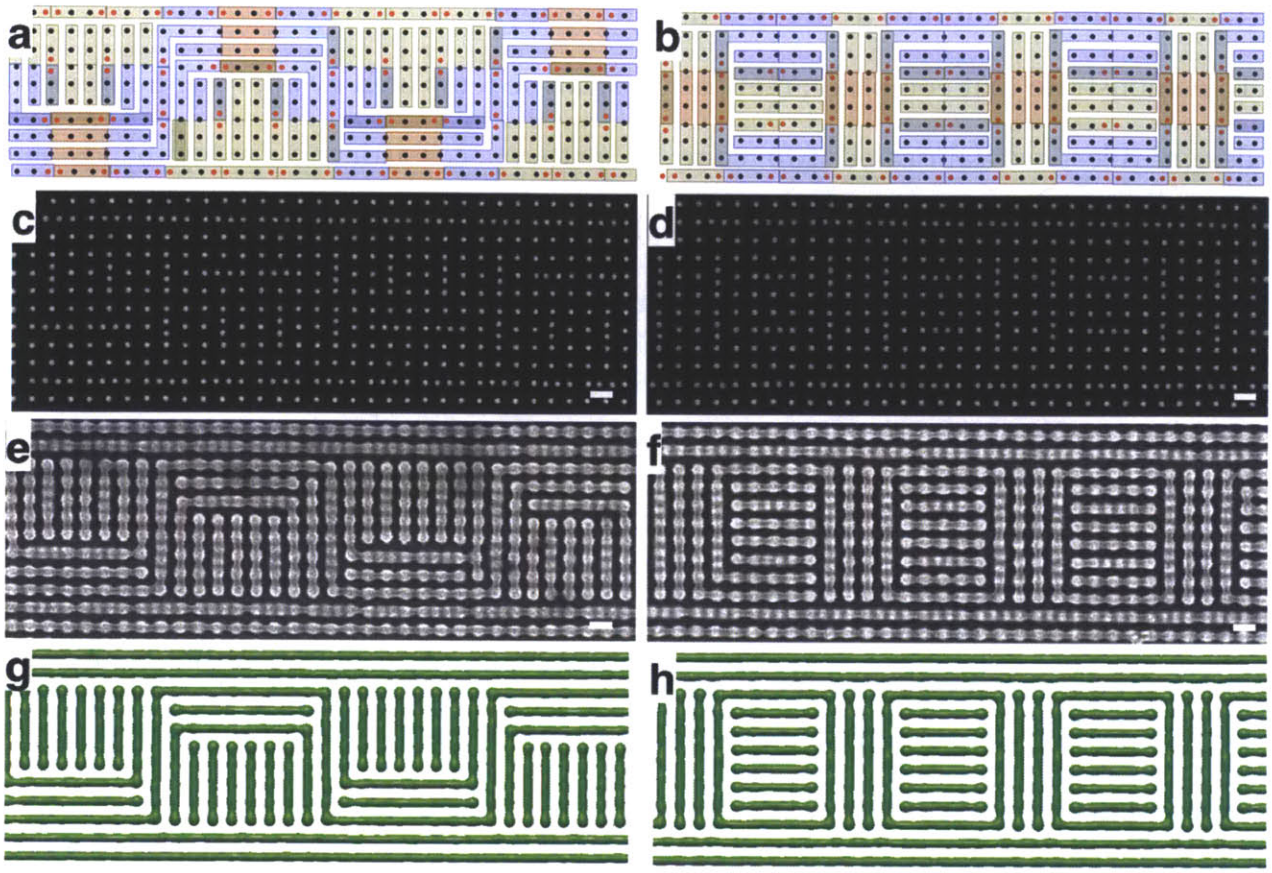

Figure 3-4: Two examples of complex target pattern fabrication. a,b, Two template layouts to fabricate complex patterns consisting of dense bends and terminations. Each color represents the pattern templated by each arrangement. c,d, SEM images of the templates to fabricate dense patterns of bends and terminations. e,f, SEM images of the PDMS patterns formed on the template shown in c and d. $G_{Y\%}$ = 97% (Figure 3e) and 99% (Figure 3f). g,h, SCFT simulation result showing the constant 50% density surface of PDMS cylinders assembled with the template in c,d. Scale bars: 50 nm.

3.5 Free energy of various patterns formed on two arrangements

To understand the differences between the experiment and prediction shown in Figure

3-3 and 3-4, we fabricated a large template array consisting of various different combinations of tile arrangements and observed the self-assembled patterns of the block copolymer on the template. $D_{Y\%}$ was 100% for the Y^4 arrangement having four parallel PDMS cylinders regardless of the arrangement of their nearest neighbor design cells. $D_{Y\%}$ = 64% for the X^2Y^2 arrangement having a pattern identical to the predicted pattern, as shown in Figure 3-5a-i. However, 7% of the X^2Y^2 arrangements yielded an internal bend, as shown in Figure 3-5a-iii,iv. As shown in Figure 3-5a-ii,iii,iv,v, $G_{Y\%}$ of the unmatched patterns were 92%, 88%, 79%, and 83% respectively. For the XY^3 arrangement, $D_{Y\%}$ was 60%, as shown in Figure 3-5b-i. In 13% of the XY^3 arrangements, the position of a bend was shifted by one grid point to the X_1 double post, as shown in Figure 3-5b-ii. In 10% of the XY^3 arrangements, the position of a bend was shifted by one grid point to the Y_3 double post, as shown in Figure 3-5b-iii. The defects in Figure 3-5a-ii,iii,iv,v and 3-5b-ii,iii,iv had a common defective feature and they could be explained by one simple mechanism (Figure 3-12).

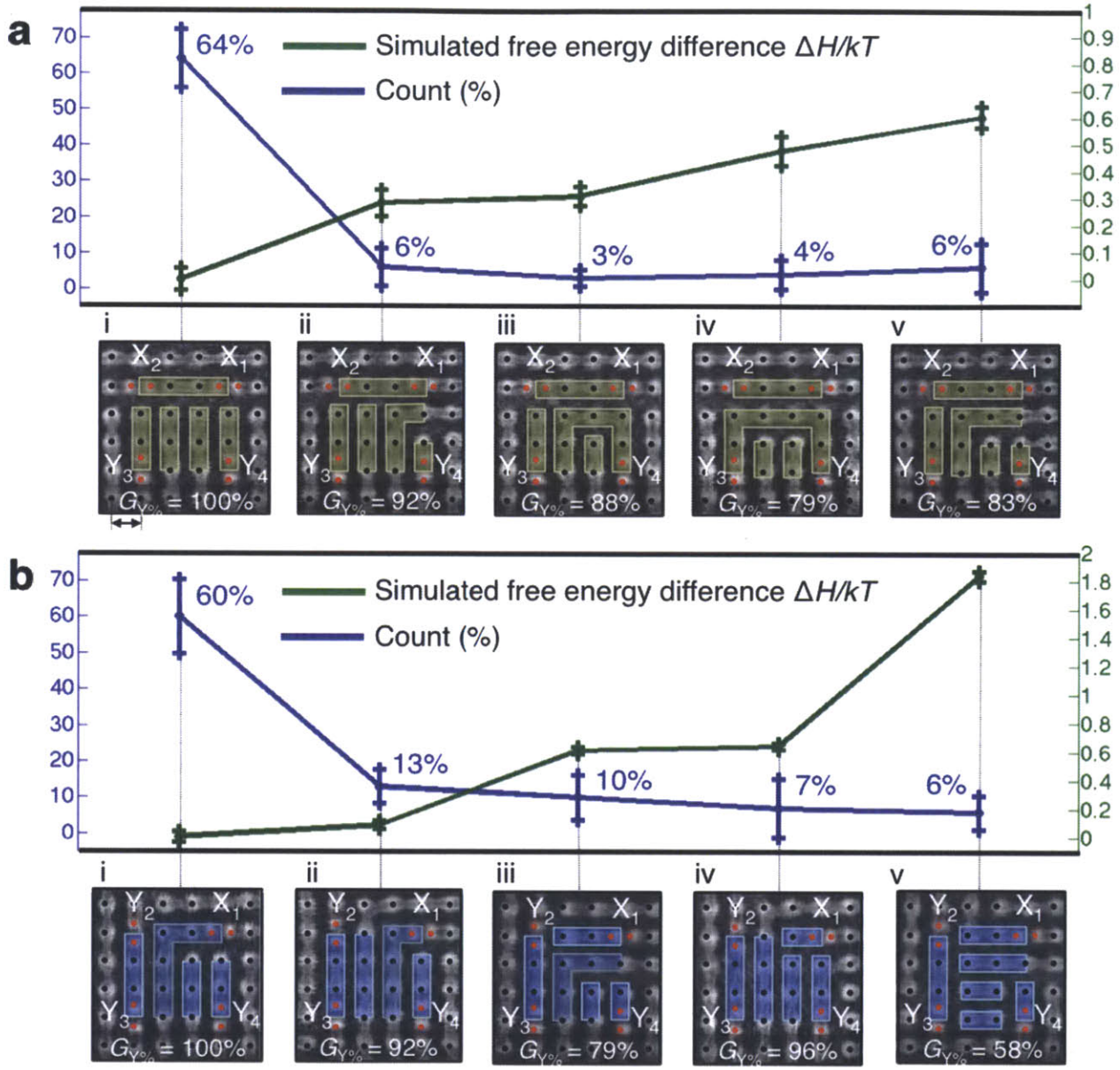

Figure 3-5: Counts and simulated free energy differences of various patterns formed on the X^2Y^2 and XY^3 arrangements. **a-b**, Panel i shows the SEM image of the PDMS pattern identical to the predicted pattern of **a**, X^2Y^2 arrangement and **b**, XY^3 arrangement. Panels ii-v show other patterns observed from the **a**, X^2Y^2 arrangement and **b**, XY^3 arrangement. Error bars show ± 1 standard deviation of the count (blue line) and simulated free energy difference (green line). $G_{Y\%}$ is the grid point yield of each

pattern. The ranges of the right y-axis in a and b are different. Length of double arrow: 39 nm.

To gain insight about the relative counts of the patterns shown in Figure 3-5, we used SCFT simulations to compute the free energy of those patterns and investigate the equilibrium stability of the patterns (collaboration with Adam F. Hannon, Professor Caroline A. Ross, and Prof. Alfredo Alexander-Katz). These free energy comparisons for the 5 structures seeded for the X^2Y^2 and XY^3 arrangements are shown in Figure 3-5a and b respectively. The general trend here is that the structures observed with a lower frequency had a higher free energy than the structure found most often. The qualitative agreement is good even though the model does not account for several features of the physical system: (1) the SCFT model does not consider the solvent anneal explicitly but rather implicitly through an effective χ; (2) the SCFT model does not consider fluctuations in film thickness; (3) a strong preference for the minority block to wet the air and substrate surfaces is assumed, which has been verified experimentally; and (4) the free energy calculations do not consider the activation barrier required to go from one structure to another. However, the fact that the less frequently observed structures have higher free energies in the simulation implies that the morphology is primarily driven by thermodynamic considerations. Some of the less frequently observed structures had similar free energy, implying there may be other factors influencing the observed structure count such as the effects of neighboring design cells.

3.6 Discussion

We developed four simple design cells and concatenated them to direct the self-

assembly of the block copolymer to form a complex pattern over a large area. The template can be determined even for large patterns because a pattern in one design cell can be considered independently of its neighboring design cells.

3.6.1 Advantage of this method compared with previous studies.

The use of posts, double posts, and solvent processing to achieve long-range ordered block copolymer patterns is well established. However, designing templates for achieving complex block copolymer patterns, which is essential to integrated-circuit layout fabrication, has not been established. The previous study (Yang et al., Nature Nanotech. 2010) showed a few examples of block copolymer patterns with bends, but they are limited in two aspects: (1) only simple structures like arrays of bends, not isolated bends, were achieved; and (2) the templates were designed by empirical iterations. In the previous study, double dots were introduced to orient the block copolymer microdomain parallel to the double dot, without any consideration of their effect on neighboring microdomain orientations or patterns, such as bends or terminations, and the double dots were parallel to their neighbors in a region of the substrate. As a result, only a limited set of patterns, such as an array of bends or periodic meanders were achieved after testing many different template designs. So, it was difficult to rationally design a template for isolated bends, terminations, or junctions and combinations of such patterns over a large area because the design space of the template increased dramatically as the complexity of the target pattern increased. For the same reason, it was difficult to judge which target patterns could be achieved or could not be achieved without trying many different template configurations.

The present work, unlike prior work, is focused on establishing rules for template design, going far beyond prior demonstrations of posts templating block copolymers. We developed four simple design cells and concatenated them to direct the self-assembly of the block copolymer to form a complex pattern over a large area. The template can be determined even for large patterns because a pattern in one design cell can be considered independently of its neighboring design cells. An advantage of this approach is that the post density across the substrate is constant, avoiding issues with varying proximity effect of the electron-beam exposure of the templates. We believe that the present study is a substantial advance over the prior work in that it provides a rational design process for directed self-assembly, rather than an empirical approach, which was backed up by analysis based on the energy of the different microdomain structures. The idea of using a limited set of template tiles combined in different ways to produce a target pattern could potentially be applicable to other self-assembling systems.

3.6.2 Summary and impact to other fields

The restricted set of geometric features presented in this study allows one to design a template for fabricating a target pattern without relying on intuition[7]. The templating effect of one double post is mainly decided by the orientations of its neighboring double posts, and is therefore restricted to its local surroundings. Predicting a block-copolymer pattern from a given template layout or designing a template layout for a target pattern is therefore simplified to just assembling design cells, and we expect that in principle, non-trivial patterns over a large area (e.g. a pattern relevant to an integrated circuit

layout) could be achieved.

This approach to complex templating provides advantages in the context of nanolithography. First, the time required for writing the template using electron-beam lithography can be a factor of 5 or shorter than the time required to write the complete pattern (Figure 3-13). The throughput could be further increased by using a two-step process for template generation, instead of writing all the posts serially: (1) the basic square array of posts could be fabricated by interference lithography or another massively parallel technique, which can generate periodic patterns over a large area with high throughput; and (2) the aperiodic double posts could then be fabricated by electron-beam lithography or by another serial method (Figure 3-13). Second, we believe that the four block-copolymer patterns shown in Figure 2k-n are only a subset of block-copolymer patterns that could be achieved. We expect that a variety of block-copolymer patterns could be achieved by fine-tuning several parameters including the size of the design cell; the spacing of the two posts of the double post; the height and diameter of the posts; the block copolymer film thickness; the volume fraction of the block copolymer; and the block-copolymer annealing conditions. For example, a T-junction was formed reproducibly when a post was missing (Figure 3-1). This would extend the rules and the available block copolymer geometries beyond what has been demonstrated here. Third, this approach could be used to achieve a block copolymer pattern with higher resolution. For example, a block copolymer pattern with a periodicity of 18 nm could be achieved by templating a 16 kg/mol PS-*b*-PDMS block copolymer[113] using a square post array with a periodicity of 18 nm and double posts with a post spacing of 12 nm. This resolution is difficult to achieve with electron-beam

lithography, but similar resolution has been achieved by helium-ion beam lithography[123] and scanning transmission electron microscopy lithography[124]

In summary, a template design based on a restricted set of tiles with post motifs provides a way to achieve a target pattern of line segments with bends and terminations from a relatively simple template. Forming a desired pattern by concatenating block-copolymer design cells (tiles) derived from a limited number of local template arrangements greatly reduces the difficulty of the template design process and the amount of experimentation required to achieve the target pattern. This approach, starting from a degenerate template, adding a restricted set of perturbations, and developing rules for all possible perturbation arrangements, could potentially be applied to other self-assembling systems that can be templated by topographic or chemical features. Rule-based patterning strategies have been developed for other self-assembling systems such as DNA origami[125–127]. In DNA origami, the information used to control the patterning is input via DNA synthesis, and is thus too slow to address the enormous challenge of pattern generation in a modern technological setting (a single mask for the semiconductor industry can take 5 days to pattern at a data-input rate of 10^8 bits per second). The application of such rule-based strategies to simple chemical systems, such as block copolymers, potentially solves the modern pattern generation problem, as the information defining the pattern is input lithographically. We expect that rule-based strategies could be developed further to describe assembly of other nanoscale objects such as nanoparticles, for example by functionalizing or programming nanoparticles with ligands that promote specific types of interactions[128,129]. Extensions of the algorithmic strategies described here for block copolymers may enable further

levels of control over the final pattern, and ultimately lead to a robust inverse-design process that determines the optimum template for a given target pattern.

DNA tiling does represent a type of rule-based self-assembly, but the process is fundamentally different from the approach presented here. In our work, lithographically-defined templates (top-down) direct the self-assembly of block copolymers (bottom-up) and the rules of template design were developed. We started from a degenerate template and added a restricted set of perturbations (double posts) to the degenerate template. As a result, we were able to study the block copolymer patterns formed on all possible perturbation arrangements. This process, starting from a degenerate template, adding a restricted set of perturbations, and studying patterns formed on all possible perturbation arrangements, could be applied to any other self-assembly systems that can be templated by topographic or chemical templates. However, in other rule- or tile-based works, the rules represent how the materials or tiles are synthesized (e.g. determining the DNA sequence) and refer to a specific materials system, so are different from the approach described here.

3.7 Methods and SCFT simulations

We used electron-beam lithography to fabricate the topographic template arrays and flow-controlled solvent annealing system. We collaborate with Prof. Caroline A. Ross for simulating the free energy of the block copolymer patterns.

3.7.1 Methods

Template fabrication

The templates were fabricated by using electron-beam patterning of hydrogen silsesquioxane (HSQ). HSQ films (XR-1541 2% solids from Dow Corning) with a thickness of 28 ± 1nm were spin-coated on a silicon substrate. Single-pixel dots were exposed in an Elionix ELS-F125 electron-beam lithography tool at 125 kV acceleration voltage. Square arrays of single dots with a diameter of 10 ± 1 nm and a range of pitches from 30 to 42 nm were exposed. The exposed samples were developed with a salty development system as described previously[58]. The developed sample was treated with O_2/He plasma (50 W, 10 sec) to convert HSQ posts into silicon oxide. To measure the diameter of the templates, SEM images of the templates were obtained by using a Raith 150 scanning electron microscope operated with an acceleration voltage of 10 kV. The errors of the template diameter were estimated from visual inspection of the SEM images.

Block copolymer self-assembly

The patterned substrates were treated with a hydroxyl-terminated PDMS brush layer (0.8 kg/mol, Polymer Source Inc., 170 °C for 12 h) to render the HSQ nano-posts attractive to the PDMS block. 2% of PS-*b*-PDMS (M_w = 45.4 kg/mol, f_{PDMS} = 33.5%, Polymer Source Inc.) solution in propylene glycol monomethyl ether acetate (PGMEA) was spin coated onto templated substrate to a thickness of 35 nm. The films were solvent annealed using either a flow-controlled solvent annealing system or conventional solvent annealing system for 3 h. In a flow-controlled solvent annealing system, nitrogen gas was bubbled through a liquid reservoir of 5:1 mixture of toluene and heptane at flow rate of 10 sccm and diluted by nitrogen gas flow of 0.7 sccm so that

the annealing chamber was maintained at constant solvent vapor pressure. The vapor pressure was controlled by changing the flow ratio between the solvent stream and the nitrogen stream[130]. In a conventional solvent annealing system, the sample was placed in the chamber containing a reservoir of liquid solvent (5:1 mixture of toluene and heptane). On an unpatterned substrate, the equilibrium periodicity of the PDMS cylinders (L_0) was ~39 ± 2 nm.

Reactive ion etching

The annealed block copolymer films were treated with a 50 W, 10 mTorr CF_4 plasma for 5 sec and then a 90 W, 6 mTorr O_2 plasma for 22 sec to remove the top PDMS surface layer and then the PS matrix. This two-step reactive ion etching process left oxygen-plasma-modified PDMS cylinders on the substrate[7]. The PDMS cylinders were imaged with a Raith 150 SEM operated with an acceleration voltage of 10 kV.

3.7.2 YXYX arrangement

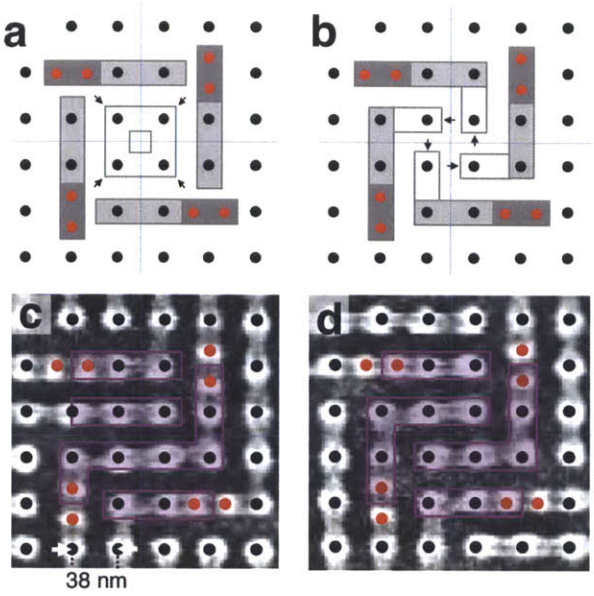

Figure 3-6: **a, b**, Two predicted block-copolymer patterns of YXYX arrangement satisfying the basic rules shown in Figure 1c and a four-fold rotational symmetry. **c,d,** Two most frequently observed block-copolymer patterns from YXYX arrangement.

As previously stated, we could not observe the predicted pattern of YXYX arrangement shown in Figure 3-2f in experiment. Figure 3-6a,b show two predicted patterns of YXYX arrangement. In Figure 3-6a,b, dark gray and light gray rectangles were predicted based on the basic design rules from Figure 3-1c. The white rectangles were arranged such that the final predicted pattern had same four-fold rotational symmetry as the YXYX arrangement. The two predicted patterns in Figure 3-6a,b either have four bends (indicated by black arrows in Figure 3-6a) or four terminations (indicated by black arrows in Figure 3-6b) formed by the white rectangles. As observed from the block copolymer patterns formed on the square arrays of single posts in Figure 1a, bends and

terminations occur at a lower frequency than lines through the post indicating these features have a higher free energy penalty of formation. This fact resulted in the block copolymer cylinders on YXYX arrangement forming more energetically favorable patterns with fewer terminations or bends regardless of the final pattern not having four-fold rotational symmetry. Figure 3-6c,d show the two most frequently observed block-copolymer patterns on YXYX arrangement. $D_{Y\%}$ of both patterns were lower than 20 %.

3.7.3 Pattern conflict between two design cells.

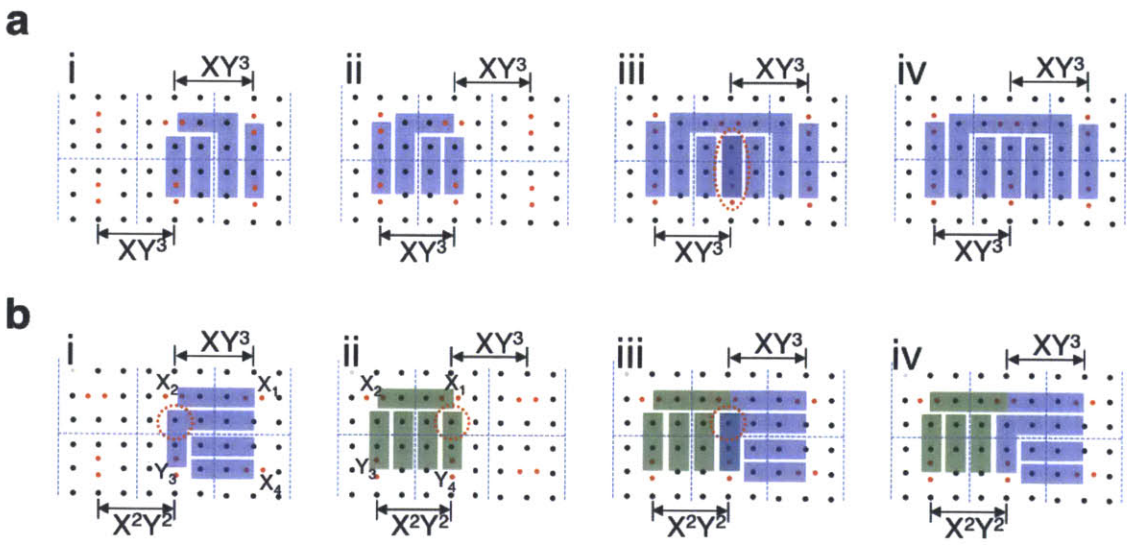

Figure 3-7: Schematic diagrams showing how the design rules were applied to two neighboring design cells. a, Two neighboring design cells having a XY^3 arrangement. **i,ii**, Predicted block-copolymer pattern of each design cell. The pattern was predicted by applying the design rule of a XY^3 arrangement. **iii**, When the design rule was applied to the two design cells together, the same pattern was predicted at the

boundary between the two design cells. **iv**, Final predicted pattern. **b**, Two neighboring design cells having a XY^3 arrangement and a X^2Y^2 arrangement. **i,ii,iii**, When the design rules of the XY^3 and X^2Y^2 arrangements were applied together, a bend was predicted by the XY^3 arrangement and a termination was predicted by the X^2Y^2 arrangement at the boundary between the two design cells (red dotted circle). **iv**, According to the observation in Figure 3-1c-iii, a bend would form when another block-copolymer cylinder comes to a termination. So, the bend would override the termination on the single post.

When a block-copolymer pattern of two neighboring design cells is predicted, the predicted patterns of the two design cells may or may not conflict. Figure 3-7a shows a case without conflict, and Figure 3-7b shows a conflict case. In Figure 3-7a the two neighboring design cells have a XY^3 arrangement. Figure 3-7a-i,ii show a block-copolymer pattern of each design cell predicted by applying the design rule of the XY^3 arrangement. When the design rule was applied to the two design cells together, the same pattern was predicted at the boundary of the two design cells (Figure 3-7a-iii). As a result, the pattern of these two design cells was predicted just by overlaying the predicted patterns of the two design cells (Figure 3-7a-iv). However, as shown in Figure 3-7b, two predicted patterns conflicted at the boundary of two neighboring design cells having a X^2Y^2 arrangement and a XY^3 arrangement. As shown in Figure 3-7b-iii, a bend was predicted by the design rule of the XY^3 arrangement at the boundary but a termination was predicted by the design rule of the X^2Y^2 arrangement. In this case, the bend would override the termination, because a bend forms when another block-copolymer cylinder comes to a termination (Figure 3-1c-iii). As a result, the final

predicted pattern would have the bend instead of the termination at the boundary of the two design cells, as shown in Figure 3-7b-iv.

3.7.4 Grid prediction yield $G_{Y\%}$

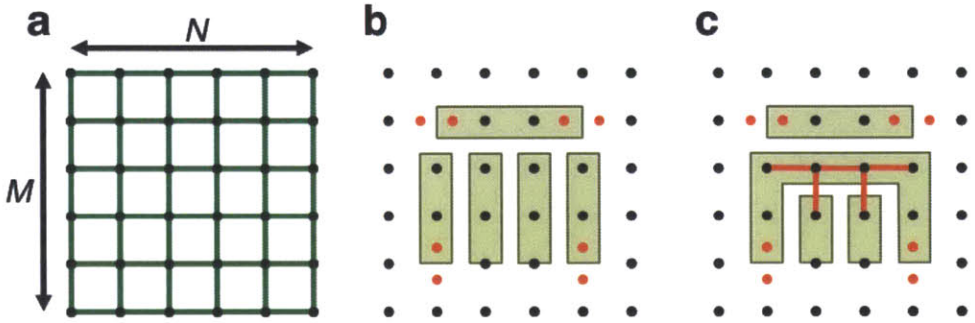

Figure 3-8: **Grid prediction yield. a**, M-by-N square grid. The total number of lines connecting one grid point to its nearest neighbors is given by $M(N-1)+N(M-1)$. **b**, The predicted block-copolymer pattern of the X^2Y^2 arrangement. **c**, One of the observed block-copolymer pattern from the X^2Y^2 arrangement. Red lines represent the mismatches between the predicted pattern and the pattern in **c**.

The grid prediction yield was defined as the ratio of the number of matched features on individual grid points to the total number of grid points. When there is a M-by-N square grid (Figure 3-8a), the total number of lines connecting one grid point and its nearest neighbors is given by $M(N-1)+N(M-1)$. One design cell consisted of a 4-by-4 square grid if we consider a double post as a single grid point, as shown in Figure 3-8b,c. Hence, the number of possible links between one grid point and its nearest neighbor grid points in this 4-by-4 square grid is 24. Figure 3-8b shows the predicted copolymer pattern on

the X^2Y^2 arrangement and Figure 3-8c shows one of the observed block-copolymer patterns on the X^2Y^2 arrangement. When two patterns in Figure 3-8b and c were compared, there were mismatches in five lines, as shown in Figure 3-8c (red lines). So, the grid point prediction yield of the pattern in Figure 3-8c was 79% (19/24).

3.7.5 SCFT simulation

The SCFT simulations used here use the same equations and computational methods as presented in the supporting information of previous work by Mickiewicz *et al.*[94]. In the SCFT simulations, the system was modeled by using hard-wall field boundary conditions that represented the topographic posts used in experiment and PDMS attractive potentials that represented the surface-air interface and brush layer. The system was discretized onto an $N_x \times N_y \times N_z$ grid with a course-graining of 9 grid points assigned to a distance of L_0. Both 2D ($N_z = 1$) and 3D simulations were performed for comparison (note that only the final 3D results are reported here). The posts were modeled with a hard-wall potential field value surrounded by an attractive field parameter modeling the PDMS brush layer. Two coarse grainings of posts were used as schematically shown in Figure 3-9 with the first single point hard-wall potential corresponding to ~8 nm post and brush layer and the second five point hard-wall potential corresponding to ~16 nm post and brush layer. These 9-by-9 grids were concatenated to form the entire simulation cells used with periodic boundary conditions imposed in the planar directions and confined boundary conditions in the thickness direction for the 3D simulations. The resulting simulation cells were on the order of ~108 by ~108 by 20 grid points (the thickness here chosen to roughly correspond to a

swelling thickness observed in experiment of ~2.0 L_0). The lateral grid points used varied depending upon the simulations.

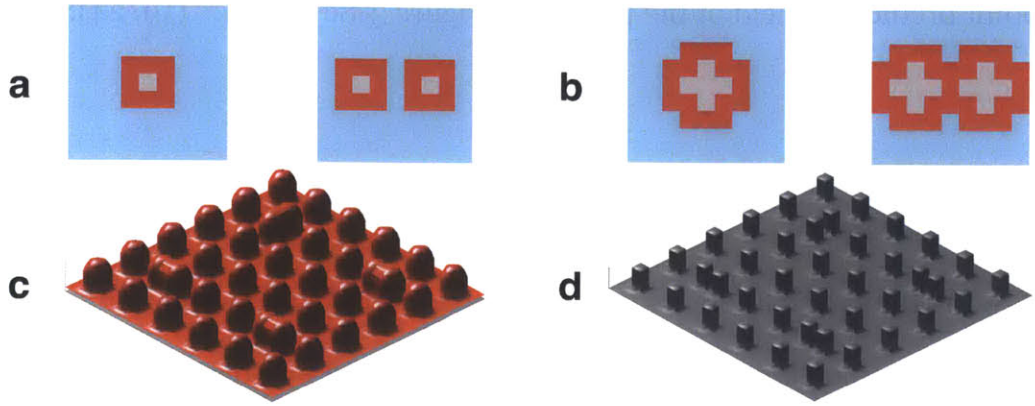

Figure 3-9: **a**, Left: Cross section of a single 9-by-9 grid used in the SCFT simulations with a single grid point in the center assigned for a single post in grey and the surrounding red grid points being attractive to PDMS with the remaining blue region being unconstrained fields that evolve during the simulation. Right: Corresponding 9-by-9 grid cross-section for double dot motifs used in the SCFT simulations. **b**, Left: Cross section of a single 9-by-9 grid used in the SCFT simulations with five grid points in the center assigned in grey for larger post modeling and the surrounding red grid points being attractive to PDMS with the remaining blue region being unconstrained fields that evolve during the simulation. Right: Corresponding 9-by-9 grid cross-section for double dot motifs used in the SCFT simulations. **c**, Schematic of the PDMS attractive surface field boundary conditions (red) in the 3D SCFT simulations using an XY_3 design cell for the post type in **a**. **d**, Schematic of the post hard wall repulsive field boundary conditions (grey) in the 3D SCFT simulations using an XY_3 design cell for the post type in **b**.

Since the primary interest in using the simulations was to explore the energetics of various structures, most simulations were seeded with target structures and the chemical potential fields relaxed holding the seeded density fields constant to obtain estimates of the free energy of the structures. These target-structure density fields were created by first simulating a single cylinder feature over a single or double post in a 9-by-9-by-20 grid and then concatenating the field results into the appropriate seed structure. The field relaxation required two steps. First the exchange field Ω_- was relaxed until the free energy reached an approximately constant value (~10,000 to 20,000 iterations). Then the pressure fields Ω_+ were relaxed based on the density solution of the relaxed Ω_- until the free energy was again approximately constant. Various likely seed structures were used to test each template.

In the experiment, the film thickness during solvent swelling varied from around 1.5 to 2.0 L_0, so in the simulations a film thickness corresponding to 2.0 L_0 was chosen for simplicity in 3D simulations, though further studies on the effect of film thickness on the structures and viability of the design rules for these thicknesses should be taken into consideration. The post heights used in experiment were around ~2/3 L_0 but it has been observed that the exact height in relation to the film thickness affects the final morphology, so various post heights were tried in preliminary simulations. Since the experimental system is solvent annealed, the exact equilibrium volume fraction may not be exactly the bulk value due to the solvent preferentially swelling the two blocks differently. Thus different volume fractions were tried during preliminary simulations. The exact χ value used was reduced by a factor of ~1/2 since the solvent was modeled

implicitly by varying χ and the volume fraction (assuming ~50% of the system consists of solvent). Since all these parameters need to be optimized for comparison with experiment, an initial screening of the structure made experimentally in Figure 3-3g was initiated in the simulations for a range of post heights from 0.67 L_0 to 1.11 L_0 and a range of volume fractions from 0.30 to 0.37 on a 162-by-81-by-16 grid. Here the thickness corresponded to 1.5 L_0. The resulting minority densities after 10,000 iterations were calculated and are shown for the interface density of 0.5 in 3D along with the total energy of the system (not normalized by grid point volume) in Figure S5. From these simulations, the seeded structure only stabilized for volume fractions greater than 0.35 in the simulation. For all the post heights used, these higher volume fractions kept the structure after relaxing the fields, but the lowest energy structure occurred for the shorter posts. Based on these considerations, the lowest volume fraction that kept the structures intact of 0.36 and height that gave the lowest free energy of 0.78 L_0 were chosen to use as the parameters for free energy comparison simulations of structures observed in the X^2Y^2 and XY^3 design cells. These parameters do not correspond exactly to the experiment, so other parameters such as total design cell thickness and surface energy attraction strength could be optimized to get better corresponding results. However, this optimization is not necessary since only general free energy trends were of interest. The surface energy attraction strength was based upon the values used in previous studies[94].

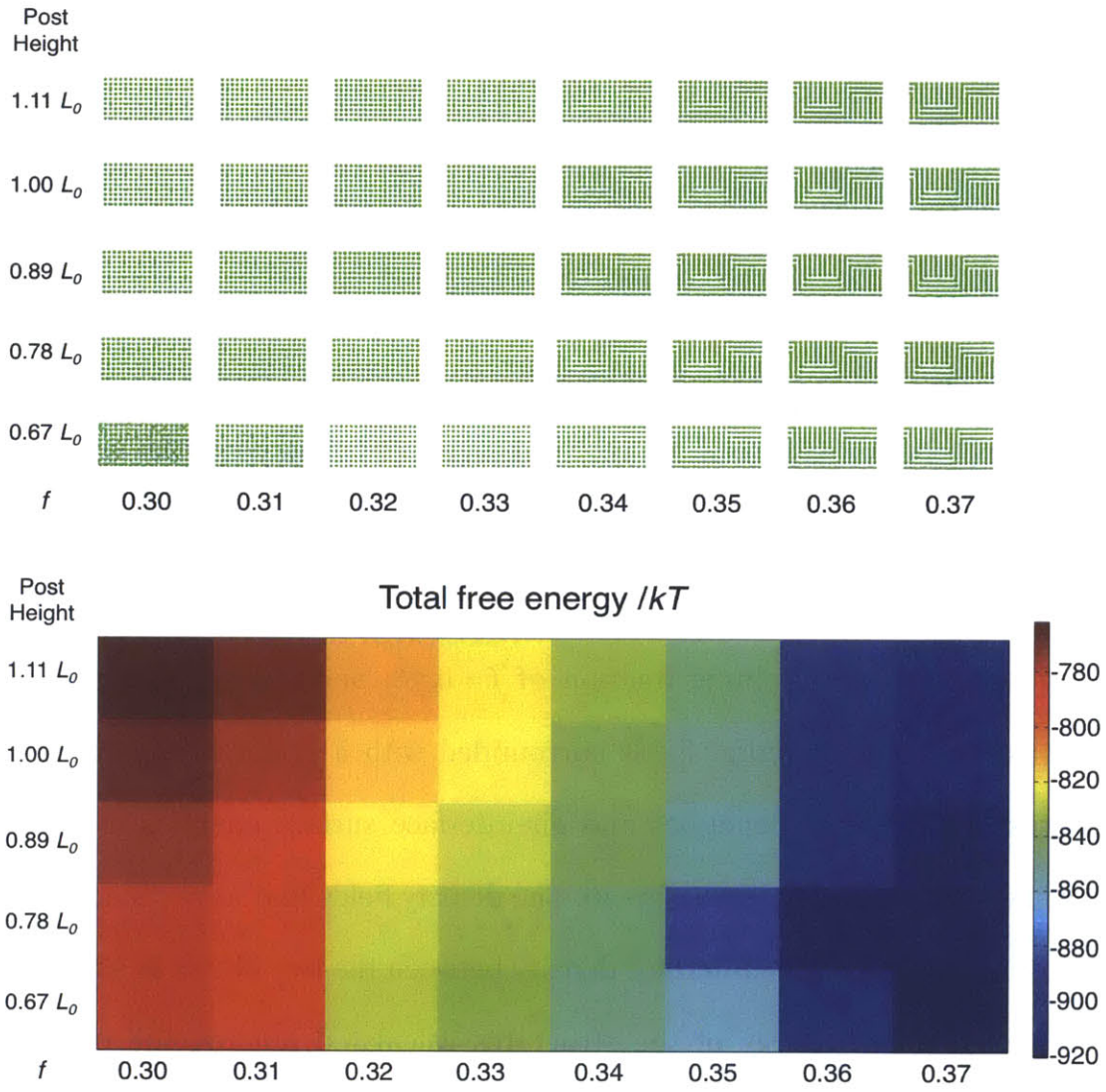

Figure 3-10: Top: Preliminary simulation phase diagram using the target structure from Figure 3 as an initial seeding. Parameters changed were height of posts and effective volume fraction. For volume fractions above 0.35, the structure remained after 10,000 iterations implying the structure was a potential equilibrium structure. Bottom: Total free energy of preliminary simulation phase diagram. The energy decreased with increasing volume fraction. For a volume fraction of 0.36, the post height of 0.78 L_0 had the lowest free energy and thus these parameters were chosen for additional simulations.

Using the parameters corresponding to stable formation of the target cylindrical patterns, the 10 structures shown in Figure 4 were each seeded into a simulation box with appropriate X^2Y^2 and XY^3 template boundary conditions. To eliminate effects of periodic boundary conditions, internal reflective boundary conditions were implemented such that a 4-fold reflective simulation cell was created for the structures with additional buffer layers of X^4 or Y^4 design cells that were the same in each simulation for the given boundary conditions. In these simulations, the block copolymer was modeled with a Flory-Huggins parameter $\chi = 0.224$, $N = 125$ effective Kuhn monomer segments and volume fraction of $f = 0.36$, and topographic post features modeled as hard wall potential fields surrounded with a preferential surface field to model brush layer surface energies and air-interface surface energies in periodically bound design cells of size 81-by-81-by-20. The density fields that were seeded are shown as 3D isosurface for the 50% interface density between the two blocks in Figure S6. The difference in the free energy of the structures calculated holding the density fields constant while relaxing the fields and their standard deviation are thus shown in the main text in Figure 4. Note that the use of reflective boundary conditions rather than considering neighboring design cells as well as having a buffer layer of the Y^4 structure may change some of the energetics at the boundary of the structures. Since the connectivity of the cylinders differs only in the design cell of interest across a given post template, one can safely compare the relative free energies of these structures. The absolute values of these energies are not as important since they depend on the boundary conditions used. Ideally one would want to calculate a free energy of an isolated design cell, but because there are always boundary issues at the connections,

there are inherently effects due to the neighboring design cells or whatever boundary conditions are chosen that affects the final energetics of the system.

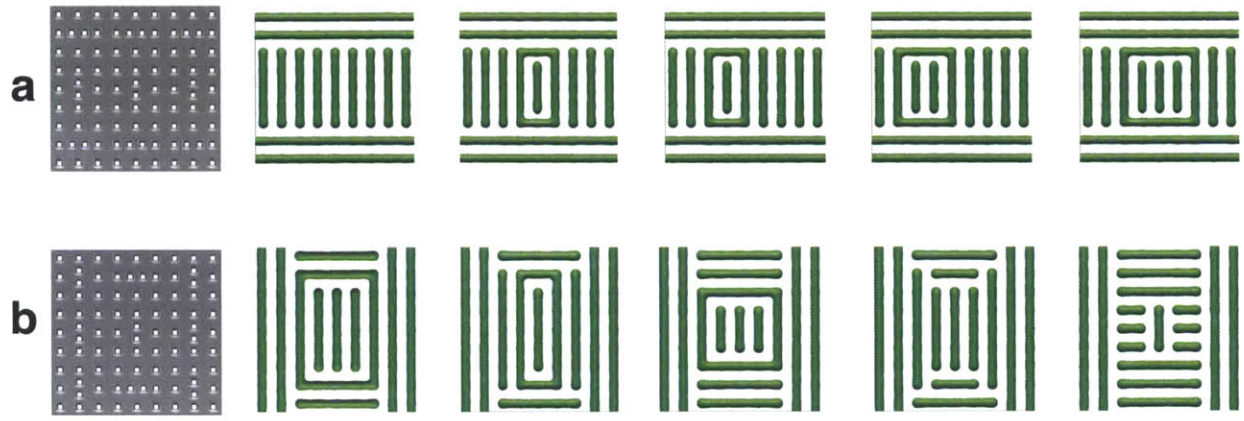

Figure 3-11: **a**, Left: Post template used to examine free energy of X^2Y^2 template in SCFT simulations. Template used periodic boundary conditions with a buffer layer of 3 X^4 design cells on the top and bottom with the other 6 design cells being X^2Y^2. Right: 3D plots of constant density surfaces $\phi = 0.5$ for structures used to simulate observed structures for the X^2Y^2 template in experiment. **b**, Left: Post template used to examine free energy of XY^3 template in SCFT simulations. Template used periodic boundary conditions with two buffer layers of 3 Y^4 design cells on the sides and 2 X^2Y^2 design cells at the top and bottom with the other 4 design cells being XY^3. Right: 3D plots of constant density surfaces $\phi = 0.5$ for structures used to simulate observed structures for the XY^3 template in experiment.

The general trend of the populations of the block copolymer patterns formed on each template arrangement show in Figure 3-5 did agree well with what was expected from the calculated free energy of the patterns. This indicates that thermodynamic considerations have a key role in determining which pattern forms. The good qualitative

agreement supports the use of SCFT for analysis of the energies of the structures. However, the relative populations of the block copolymer patterns formed on each template arrangement was not a perfect match to those predicted from the free energy, indicating an important role of kinetics in determining which pattern forms. This is perhaps not surprising since the samples were solvent annealed and the kinetics of this process is still under investigation. We expect that more study on the kinetics is required to predict the relative counts of the block copolymer patterns precisely, which will be a topic for future work.

There is not an exact correspondence between the experimental occurrence percentage and the free energy of the structures calculated via the SCFT simulations because the SCFT does not capture all the details of the system. In particular, it does not consider the kinetic pathway to forming a structure, but only the free energy. For example, one structure may be much higher in energy from an equilibrium standpoint, but may be kinetically trapped during the solvent annealing, producing the structure in the higher energy state more often than expected from a simple Boltzmann distribution. There are other model approximations that may affect the energies of structures, such as the use of periodic boundary conditions, which means that calculating the exact energy of an isolated tile is not strictly possible. Other differences include approximations to the post size, shape, surface energy, etc., and the assumption of a fixed film thickness.

The discrepancies between calculated energy and observed frequency of different structures suggests to us that there is a kinetic component that affects which structures occur. However, the fact that the lowest energy structures still dominate the majority of

the landscape of structures observed means that we are reaching equilibrium structures in most cases, and thus the model is useful in characterizing the most probable morphologies.

3.7.6 Common defective feature

When we examined the defects in Figure 3-5, we found that several defects had a common defective feature. The common defective feature was found between two double posts that were perpendicular to each other. In this situation, a termination formed where the extension of one double post met the other double post (Figure 3-2c-ii, Figure 3-12a). However, in the common defective feature, an additional PDMS cylinder formed between the two double posts (Orange rectangle in Figure 3-12b).

When we developed the rule-based approach, we assumed that the block copolymer pattern of a design cell is primarily determined by the orientations of the surrounding four double posts regardless of its neighboring design cells. However, when we studied the block copolymer patterns formed on a template array consisting of various combinations of tile arrangements, we found that a defect formed at the boundary of one design cell could propagate to its neighboring design cells and induce another defect there. The majority of defects shared one common feature. As shown in Figure 3-12, the most common defective feature was found between two perpendicular double posts. Usually a termination formed where the extension of one double post met the other double post. However, in the common defective feature, an additional PDMS cylinder formed between the two double posts. All the four unmatched patterns of the X^2Y^2

arrangement and three unmatched patterns of the XY^3 arrangement had this common defective feature, so the key to increasing the probability of getting the predicted pattern of the XY^3 and X^2Y^2 arrangements is prohibiting the formation of the common defective feature. The probability of getting the predicted pattern would then increase to 83% for the X^2Y^2 arrangement and 90% for XY^3 arrangement.

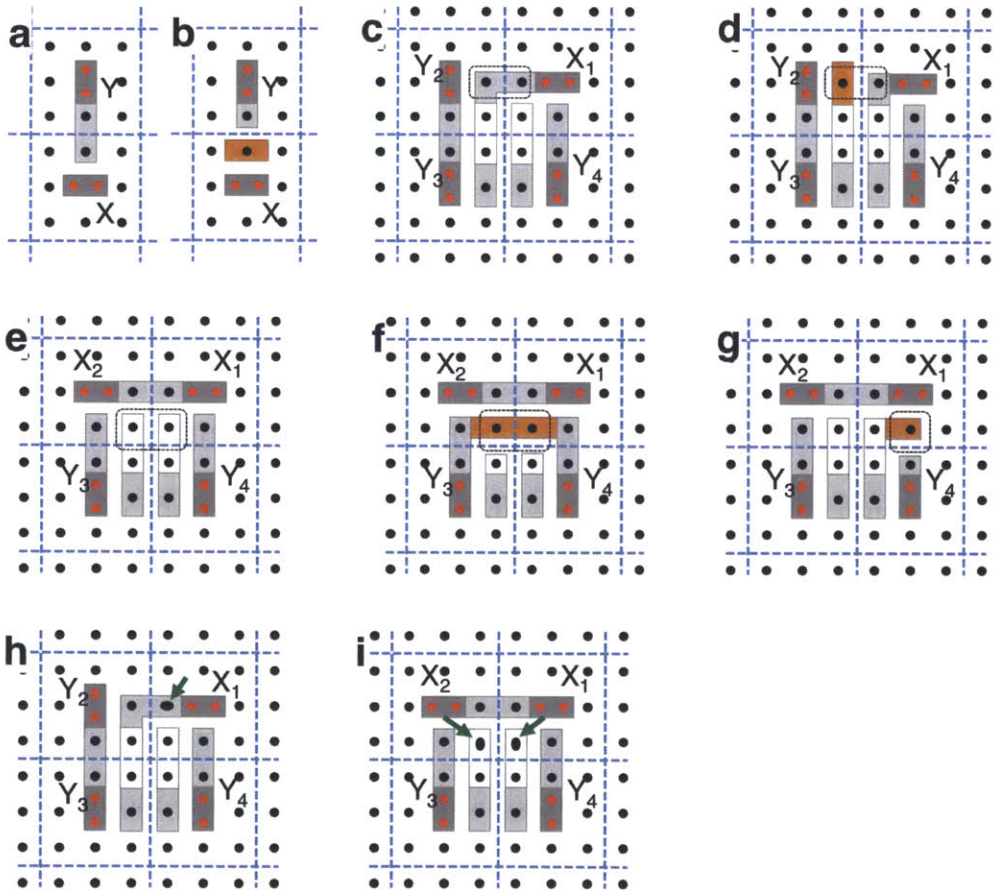

Figure 3-12: Schematic diagrams showing a common defective feature. Dark gray rectangles: PDMS cylinders templated by a double post; Light gray rectangles: PDMS cylinders templated by the PDMS cylinders formed at double posts; White

rectangles: PDMS cylinders formed on the four single posts at the center of the design cell; Orange rectangles: additional PDMS cylinder formed between two perpendicular PDMS cylinders. **a,c,e**, Dominant block-copolymer patterns observed on **a**, two perpendicular double posts; **c**, XY^3 arrangement; and **e**, X^2Y^2 arrangement. Defective patterns observed on **b**, two perpendicular double posts; **d**, XY^3 arrangement; and **f,g**, X^2Y^2 arrangement. **h,i,** Possible way to prevent the formation of the common defective feature by using elliptical-shaped posts instead of circular posts. Green arrows indicate the positions where the elliptical-shaped posts should be used to prevent the formation of the common defective feature.

In one of the defects formed on a $X_1Y_2Y_3Y_4$ (=XY^3) arrangement, the position of a bend was shifted by a one grid point to X_1, as shown in Figure 3-12d. On the X_1-Y_2 double post pairs, the common defective feature shown in Figure 3-12b formed, instead of the pattern in Figure 3-12a. In two of the defects formed on a $X_1X_2Y_3Y_4$(=X^2Y^2) arrangement, a bend formed inside the design cell (Figure 3-12f,g). In those two defects, an additional PDMS cylinder parallel to the X_1 and X_2 double posts formed and the internal bend formed where the additional PDMS cylinder met another PDMS cylinder. So, the defects in Figure 3-4a-ii,iii,iv,v and 3-4b-ii,iii,iv formed when the pattern in Figure 3-12b formed between two perpendicular double posts instead of the pattern in Figure 3-12a. One possible way to prevent the formation of such common defective feature would be using an elliptical-shaped post instead of circular post. As shown in Figure 3-12(h,i), elliptical-shaped posts would guide the PDMS microdomains to be aligned parallel to the elliptical-shaped posts and thus prevent the formation of the common defective

feature. Closely positioned two posts could also be used instead of the elliptical-shaped posts.

3.7.7 Throughput

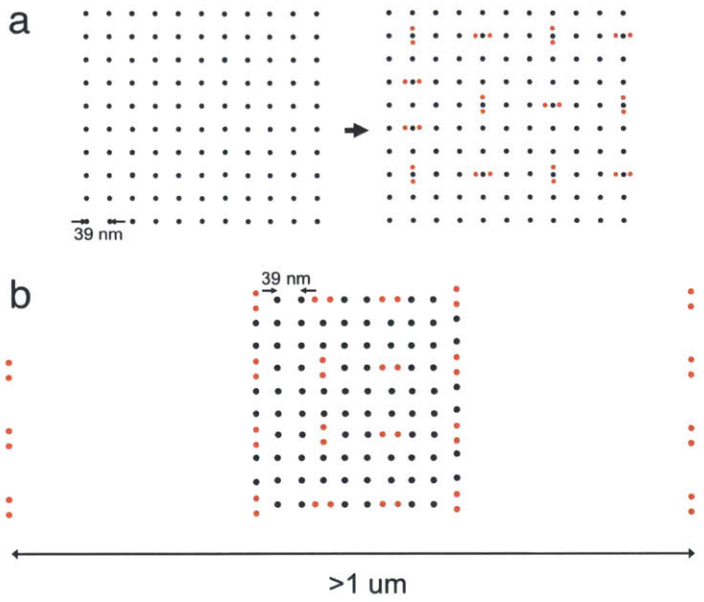

Figure 3-13: Two possible methods for increasing the throughput of template fabrication. a, Square array of single posts are fabricated by a massively parallel technique, such as interference lithography and double posts are fabricated on the square array of single posts by a serial fabrication technique, such as electron-beam lithography. **b**, If a target pattern consists of many parallel lines and few complex patterns, a sparse array of double posts or lines can be used to achieve a long-range ordered block copolymer patterns.

One of the best advantages of our approach is that a square array of single and double posts requires less writing time than simply directly writing a final pattern. The

templates shown in Figure 3-2,3 occupied ~10% of the area occupied by the final patterns. When the pattern writing time of the templates was estimated, it was 22~40% of the time required for directly writing the final patterns (depending on the line width of the final patterns), giving a factor of 2.5 ~ 5 increase in throughput. The throughput of the template fabrication can be further increased by using two possible approaches. First, as shown in Figure 3-13a, we can use a massively parallel technique to fabricate a square array of single posts and then use a serial fabrication technique to fabricate double posts. This approach will result in a triple post rather than a double post, but we expect that same design rules will apply to this array of single and triple posts and in fact may enhance the reliability of the rules by having a stronger orientation preference for the block copolymer near the triple post when compared with the double post. In this method, the overlay accuracy of two separate exposures should be smaller than few nanometers, which may be possible in the near future. Second, if a target pattern consists of many parallel lines and sparse complex patterns, then we can use sparse double posts to achieve long-range ordered block-copolymer lines and use an array of single and double posts to make complex patterns. Jung and colleagues have shown that a trench with a width of 10 μm can be used to achieve long-range ordered PDMS cylinders[9]. Chang and colleagues also have demonstrated long-range ordered PDMS cylinders by using a sparse triple-dot array[113]. By combining a sparse double post arrays (or lines) with a square array of single and double posts, the writing time of a template could be greatly reduced.

3.7.8 T-junction

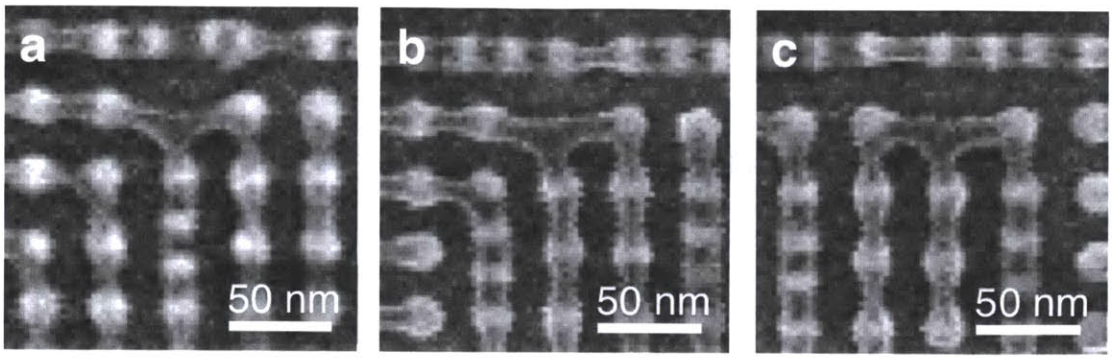

Figure 3-14: Examples of T-junctions formed at missing posts. a-c, T-junctions were formed when a single post was missing in the square array of single posts.

T-junctions are one of the essential features of a circuit layout, but this structure was not observed from the block-copolymer patterns templated by the square grid of single posts and sparse double posts. We observed instead that a T-junction was formed wherever a single post was missing (due to the errors of the electron-beam lithography system or poor adhesion of the post). Figure 3-14 shows three such examples of T-junctions. We speculate that T-junctions also could be fabricated by deliberately removing a single post, by reducing the diameter of a single post in an array of single posts, or by moving the position of a single post a few nanometers away from its original position.

3.7.9 More diverse template designs

In our tile-based approach, the range of achievable patterns is naturally going to be limited by the patterns that can be created in individual tiles. With the four template arrangements we presented in this work, an array of concentric bends cannot be

achieved from the 16 combinations of the orientations of the four double posts. However, more diverse template arrangements could be developed by using triple or quadruple dots or by removing dots. For example, an array of bends was achieved by using an L-shaped template, as shown in Figure 3-15a. We believe that a template arrangement to achieve an array of bends could be developed by using triple dots (or L-shaped templates), as shown in Figure 3-15b,c. Fig. 3-15e suggests how these tiles could be concatenated.

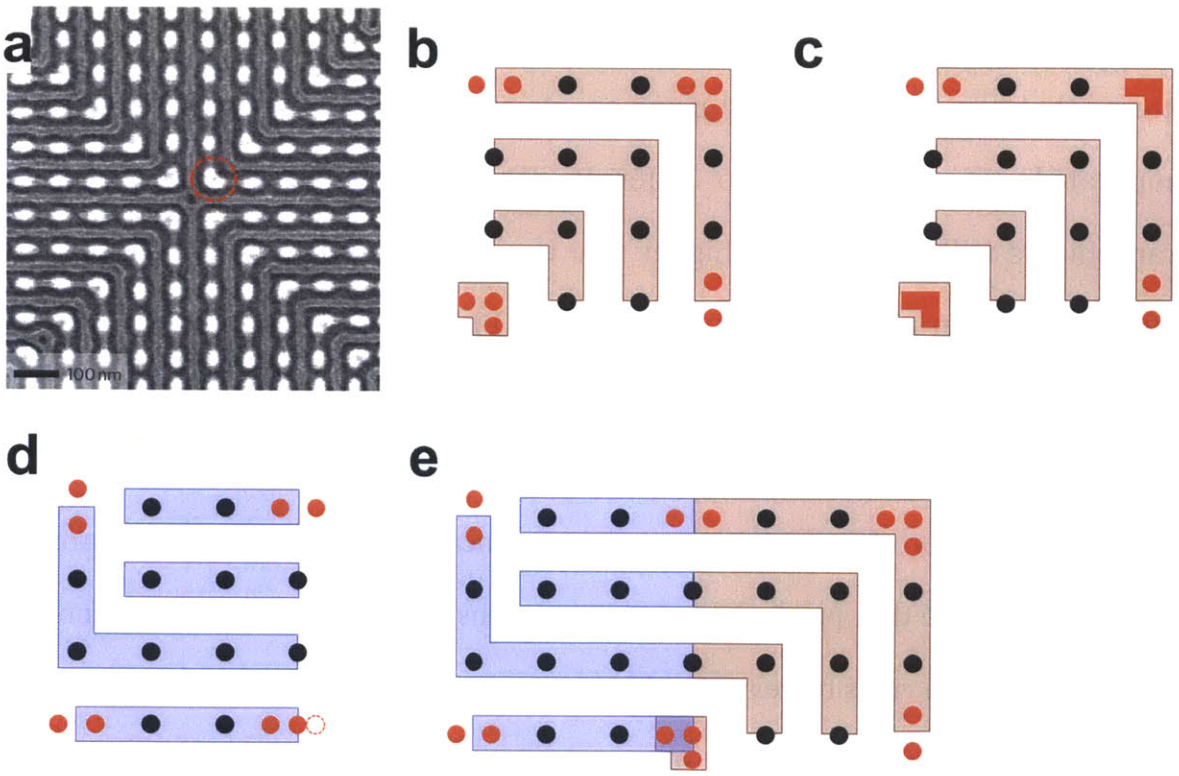

Figure 3-15. Proposed template arrangement to achieve an array of bends. a, SEM image of an array of bends achieved in the previous study by using L-shaped tepmlates (reproduced from Yang *et al. Nature Nanotechnol.* 5, 245, 2010). Red dotted circle indicates the L-shaped template. **b**, Proposed template arrangement to achieve an

array of bends. **c**, The triple dots shown in in **b** could be replaced with L-shaped templates. **d**, Modified X^3Y arrangement to be joined with the template arrangement shown in **b**. Post positioned at the dotted red circle was shifted leftward to make the X^3Y arrangement compatible with the template arrangement shown in **b**. **e**, More complex block-copolymer pattern could be achieved by joining the modified X^3Y arrangement with the template arrangement shown in **b**.

In general, we expect that there will be a limit to the geometries of block copolymer patterns that can be achieved by using sparse templates. Making the templates more complicated can give access to different geometries, but some block copolymer arrangements will always have higher free energy than others and therefore be less readily formed. An unfavorable (highly strained) morphology can always be promoted by a denser template and in the limiting case, a 1:1 template that is identical to the target pattern. The utility of the current approach comes from a compromise between having a template that can produce enough patterns to concatenate into useful structures, while avoiding a template that produces so many patterns that the selectivity between them is too small for design rules to be applicable.

3.7.10 Line edge roughness

In terms of line width roughness, we are confident that it could be improved by optimizing parameters such as the etch process or by reducing the post diameter by trimming (we have reported sub-10 nm posts previously, Chang et. al. ACS Nano 2012).

In the present work, we slightly over-etched the block copolymer films to clearly observe the block copolymer patterns and reveal post locations. We believe that the line width roughness could be improved by optimizing the etching condition. In addition to the etching condition, we have found that the line width roughness changes depending on solvent-annealing conditions and block copolymer film thickness. For example, the below SEM image shows a self-assembled 16 kg/mol PS-*b*-PDMS block copolymer directed by a rectangular lattice of posts. The natural periodicity of the block copolymer in the image was 18 nm and L_x and L_y of the post array was 36 nm and 24 nm respectively. As shown in the image, the PDMS microdomains did not bulge around the posts as they formed on top of the posts. We believe that the block copolymer film thickness during a solvent annealing process affects the line width roughness of a final block copolymer pattern by changing the height of the PDMS microdomains from the surface of the substrate. So, we expect that the line width roughness of a PDMS microdomain can be reduced by optimizing etching condition, solvent annealing condition, and block copolymer film thickness.

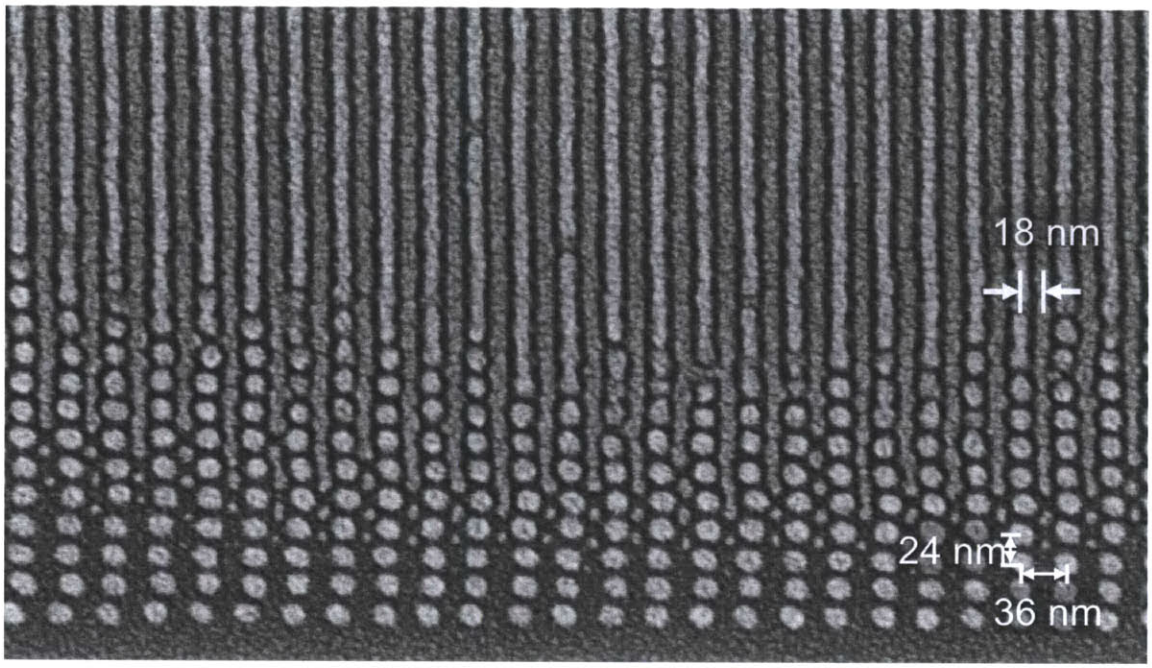

Figure 3-16. SEM image of a 16 kg/mol PS-b-PDMS block copolymer templated by a post array. The film thickness increases from the bottom to top of the image. The image was taken after a short Au/Pd sputter coating. The posts look larger than their actual diameter because the PDMS blocks of the PS-*b*-PDMS block copolymer wetted the surface of the posts (unpublished result).

Also, in our previous study (Chang et. al. ACS Nano 2012), we found that posts with diameters ranging from 8 nm to 12 nm can be used for templating a 16 kg/mol PS-*b*-PDMS block copolymer (L_o = 18 nm). Based on this study, we achieved long-range ordered block copolymer lines with a periodicity of 18 nm with a controlled orientation. To apply the method developed in this work to the 16 kg/mol PS-*b*-PDMS block copolymer, a square post array with a periodicity of 18 nm and double posts with a post spacing of 12 nm are required. This resolution is difficult to achieve with electron-beam lithography, but it has been achieved by helium-ion beam lithography (Sidorkin, V. et. al.

J. Vac. Sci. Technol. B 27(4) L18-20 2009). So, we believe that our approach could be applied to a lower molecular weight block copolymer to achieve complex block copolymer patterns with a periodicity of 18 nm.

4. Placement Control of Coiled-Coil Proteins

Patterning protein at few-molecule level or single-molecule level can be used for studying biological phenomena at single-molecule level or developing a sensor with ultra high sensitivity. Here, we demonstrate a method of making single-molecule protein array by using cysteine-gold interaction.

4.1 Introduction

Protein patterning on a substrate is a very useful for many applications, such as a platform for studying biological phenomena[131–135] or developing a sensor[136]. There have been several studies on patterning proteins, but the organization of the proteins at the single-molecular level has not been studied. Patterning proteins at various length-scales have been demonstrated by using a nanostructure[137] or self-assembled monolayer (SAM)[138–140]. Recently, patterning proteins at the single-molecular level has been demonstrated by using sub-10-nm gold or gold-palladium nanostructures[141]. However, organization of the proteins at the single-molecule level has not been studied. Here, we study the organization of the patterned proteins at the single-molecule level, and based on the study, we also control the protein organization by using various nanostructures and protein engineering.

4.2 Gold structure fabrication

We used gold nanostructures to control the position of the proteins on a surface. The gold nanodots were fabricated by using electron-beam lithography and lift-off process. A

silicon substrate was spin-coated with a thin layer of a positive-tone electron-beam resist PMMA950A with a thickness of 60 nm. The spin-coated resist film was exposed with a Raith 150 electron-beam lithography system operating at 30 kV acceleration voltage. The gold dots with diameters ranging from 30 nm to 100 nm were exposed. The exposed resist film was developed in a 3:1 IPA:MIBK at -15 °C for 30 sec[142]. 3-nm Ti film and 6-nm Au film were deposited onto the sample with a physical vapor deposition. Then the metal films on top of the resist film were removed by lift-off process. The lift-off process was carried out in 60°C NMP for 20 min. The samples were rinsed with acetone and sonicated in acetone for 1 min to completely dissolve out the resist film and remove the metal films on the resist. The fabricated patterns were imaged with a Raith 150 electron-beam lithography system operating at 10 kV acceleration voltage. This process could be used for fabricating gold nanostructures on a TEM membrane or fabricating dense gold nanodot arrays, as shown in Figure 4-2,3.

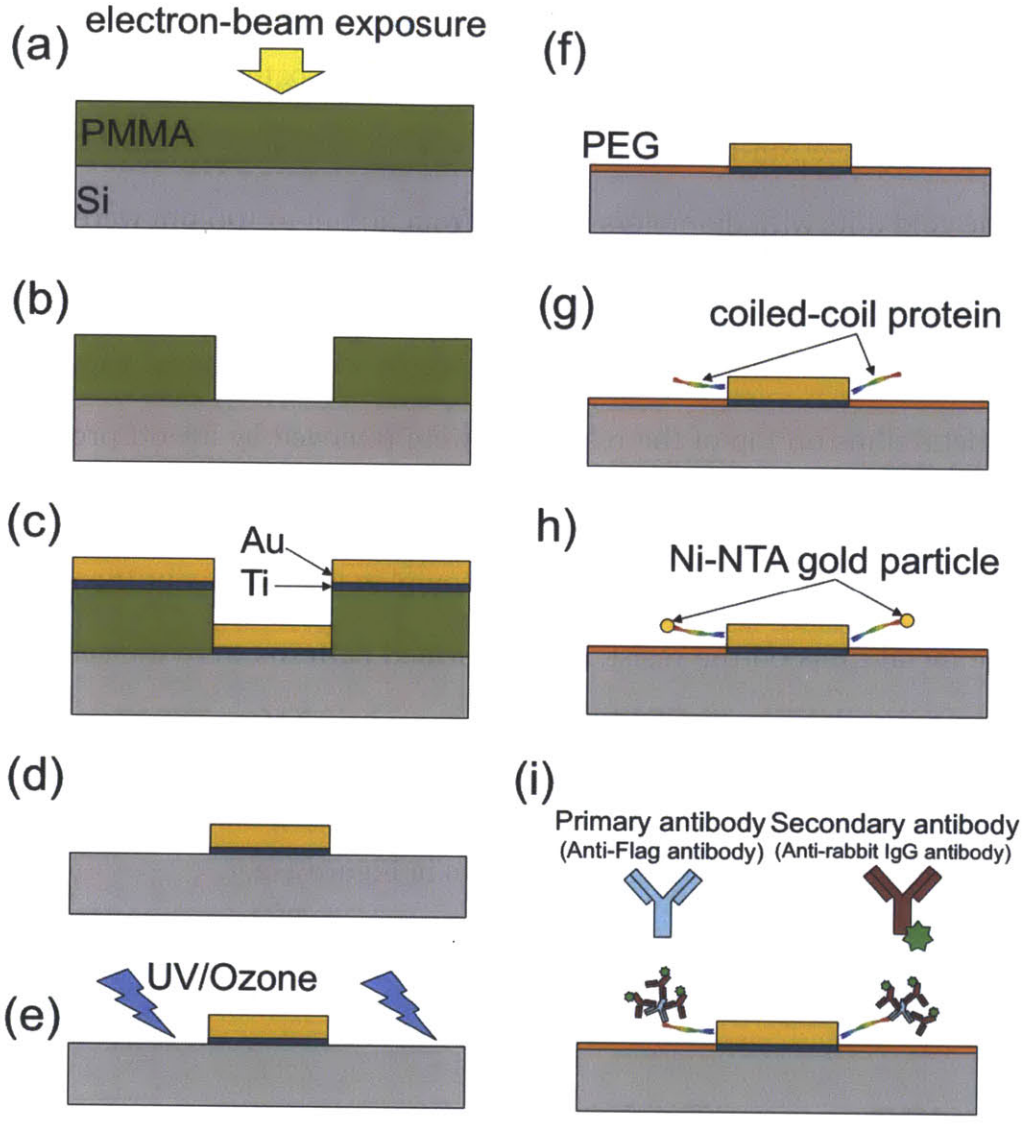

Figure 4-1. Gold nanodot fabrication process and two methods used in this study to indirectly observe the assembled proteins around the gold nanodots.

\

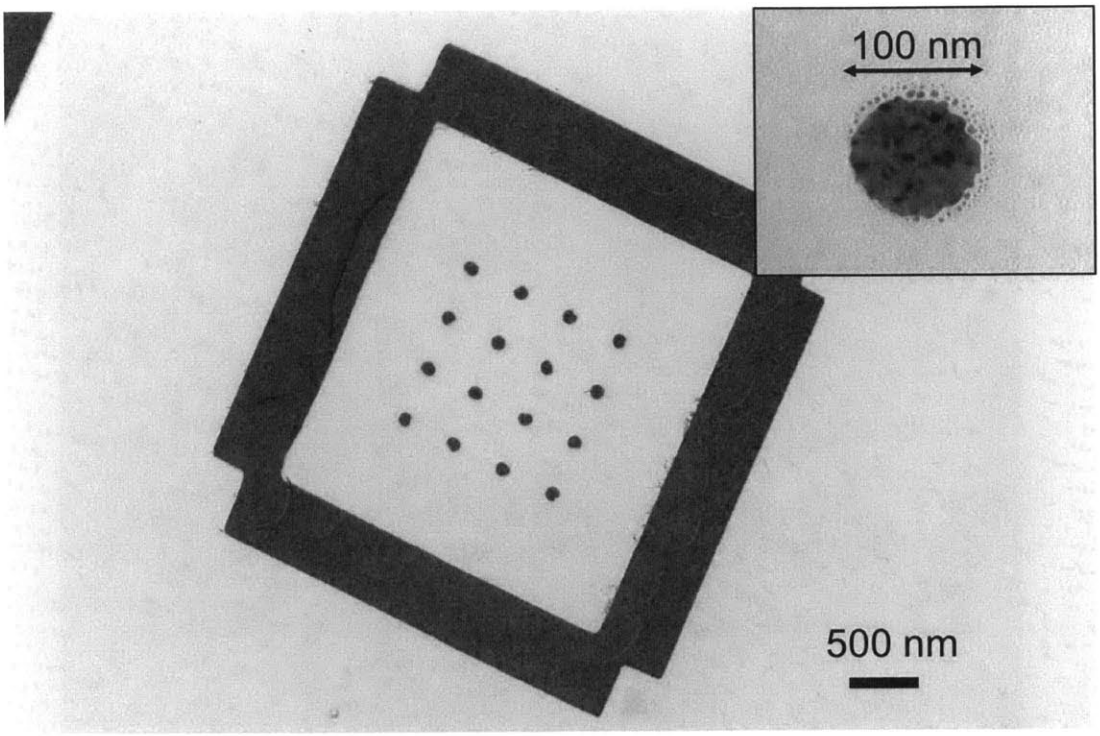

Figure 4-2. Gold nanostructures fabricated on top of a TEM membrane by the process described above.

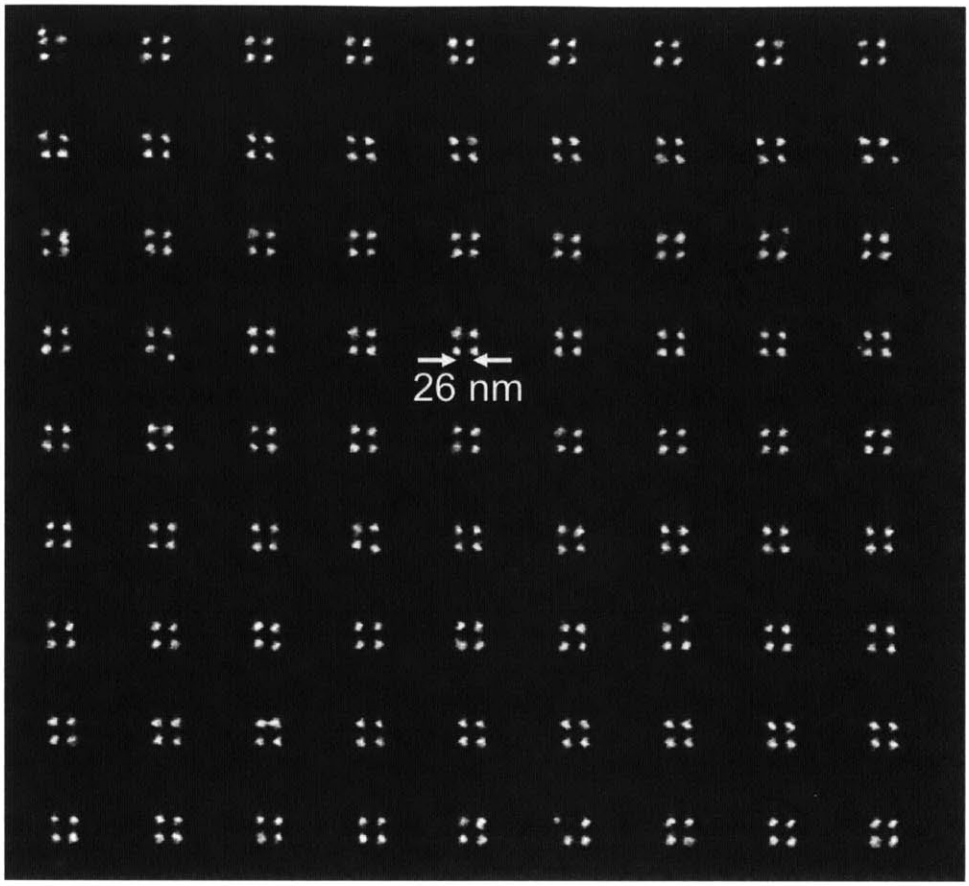

Figure 4-3. Quadruple gold nanodot arrays. The center-to-center distance between the dots of the quadruple dot was 26 nm. The diameter of the dots was around 6 nm.

4.3 Templating proteins

Here, we patterned two coiled-coil proteins by using gold nanostructures. We also studied how the assembly and distribution of the templated coiled-coil proteins change depending on the gold pattern geometries and number of cysteine residues.

4.3.1 Templating proteins by using gold nanostructures

There have been many studies on patterning proteins by using lithographically-defined patterns[131,133–135,141,143], but controlling the placement of proteins at single-molecular level has been demonstrated recently. However, in those studies, attachment of only a limited range of proteins - such as antibodies or streptavidin - was demonstrated. Such proteins were used as a linker to attach other proteins to a predefined pattern. However, using linker increases the complexity of the process and it also requires a genetic engineering of a target protein, which prevents this method to be used for patterning native proteins. To control the placement of native proteins on a substrate, an interaction between a native protein and surface pattern should be used. Here, we show that a coiled-coil protein can be attached to a gold surface with high precision through cysteine-gold interaction. By using gold nanostructure with different geometries, it is possible to achieve a higher control of the assembly of proteins. We also study how multiple cysteine residues changes the attachment of proteins. As cysteine is one of the twenty amino acids constituting proteins, our approach could be used for patterning other proteins with cysteine residues.

In this work, two coiled-coil proteins with different length were used as a model protein for demonstrating the attachment of proteins to a gold surface via cysteine-gold interaction. The advantages of using coiled-coil proteins over other proteins are their length and stiffness[144,145]. The lengths of two coiled-coil proteins are 14 nm[144] and 40 nm[145], which are much longer than usual globular proteins. Based on these two advantages (length and stiffness), we studied how the protein assembly changes depending not only on the presence of gold nanostructures but also on the arrangement of gold nanostructures.

The cortexillin I monomer consists of a large globular domain, strait coiled-coil domain, and relatively flexible tail domain[144]. We used only the strait coiled-coil domain in this study. The coiled-coil domain of cortexillin $I_{272-352}$ used in this study consisted of 81 amino acids and the expected end-to-end length was 14 nm. To demonstrate the attachment of a protein to a gold surface via cysteine-gold interaction, we added additional cysteine residue to the N-terminal of the cortexillin $I_{272-352}$, as depicted as red dots in Figure 4-4(a). We also used a longer coiled-coil protein, tropomyosin. Additional cysteine residue was also introduced to the N-terminal of tropomyosin. However, the native tropomyosin had additional cysteine residue at the 190th amino acid from the C-terminal of tropomyosin. To study the effect of this internal cysteine, we constructed another tropomyosin, in which the internal cysteine was replaced with another amino acid, alanine. We denote the mutated tropomyosin as C190A tropomyosin. To observe the attached proteins, we used two methods: (1) gold nanoparticle tagging; and (2) fluorescence microscope. To selectively tag proteins with a fluorophore, we added FLAG sequence to C-terminal of the proteins (cortexillin $I_{272-352}$, tropomyosin, C190A tropomyosin). This C-terminal FLAG sequence was used as a binding site of anti-FLAG rabbit IgG antibody and the anti-FLAG antibody was used as a binding site of fluorophore-tagged anti-rabbit-IgG antibody, as shown in Figure 4-4(c). We also added Hig-tag residue to the C-terminal of the proteins. This Hig-tag residue was used as a binding site of Ni-NTA gold nanoparticle with a diameter of 5 nm. Each coiled-coil dimer has two cysteine residues at its C-terminal, but due to steric hindrance, we expected that only one gold nanoparticle could be attached to the C-terminal of the proteins. As a result, gold-nanoparticle tagging could offered a platform for studying

how an individual protein is assembled around gold nanostructures by using a conventional SEM.

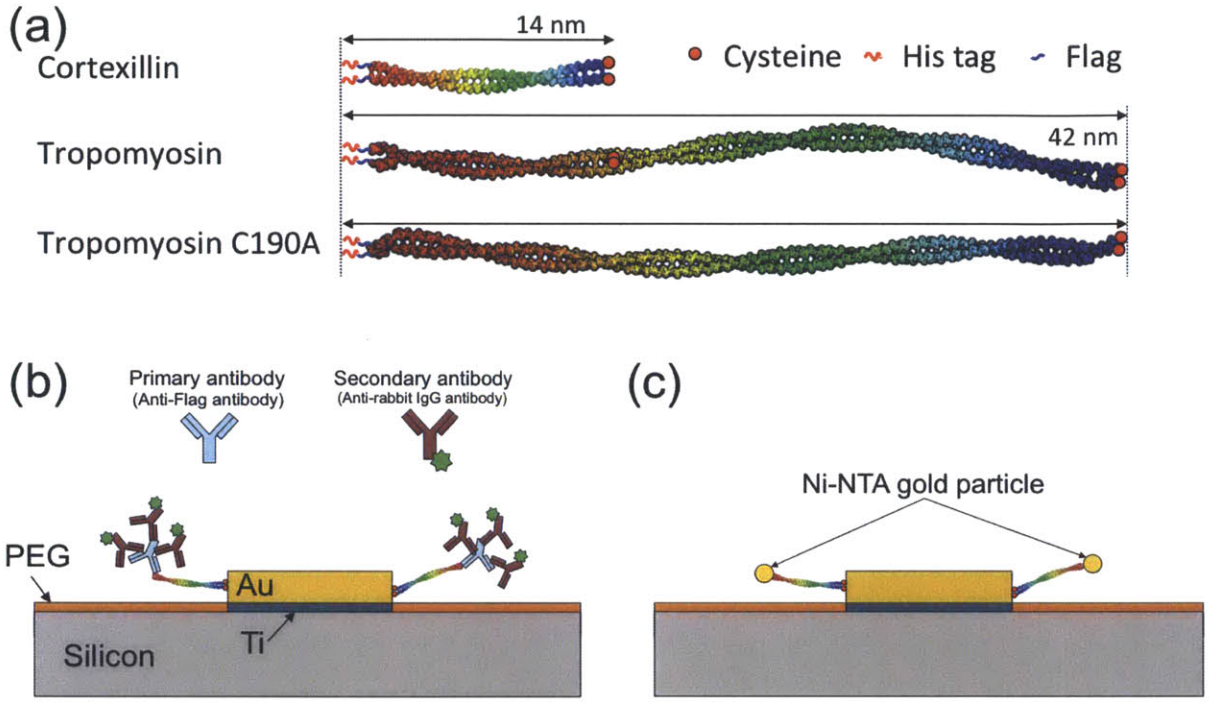

Figure 4-4. Proteins, gold nanodots, and imaging methods used in this study. (a) Schematic diagram showing three proteins used in this study. (b) Schematic diagram showing how the proteins were attached to the gold nanodots and imaged by using gold nanoparticles. (c) Schematic diagram showing how fluorophore-tagged antibody was used for observing the templated proteins.

To image proteins, a liquid tapping mode of atomic force microscope (AFM) and transmission electron microscope (TEM) have been widely used. However, a liquid tapping mode of AFM requires a relatively complex and well-maintained AFM. Also the

speed of AFM is not fast enough more large-area study. TEM is fast compared with AFM, but fabricating various nanostructures on a TEM membrane is not well established yet. So, we used scanning electron microscope to observe the attachment of the proteins to gold nanostructures. As proteins are not visible under SEM, a gold nanoparticles were used.

To template the assembly of the proteins, we used thin gold nanostructures. The gold nanostructures were fabricated by electron-beam exposure of positive-tone electron-beam lithography resist and lift-off process. 3-nm-thick titanium layer was used as an adhesion layer between a gold layer and a silicon substrate. The thickness of gold nanostructures was 6 nm. To prevent the non-specific binding of the proteins to a un-patterned surface, the surface of the substrate was coated by polyethylene glycol, which is widely used as a passivation layer[133].

4.3.2 Fluorescence imaging

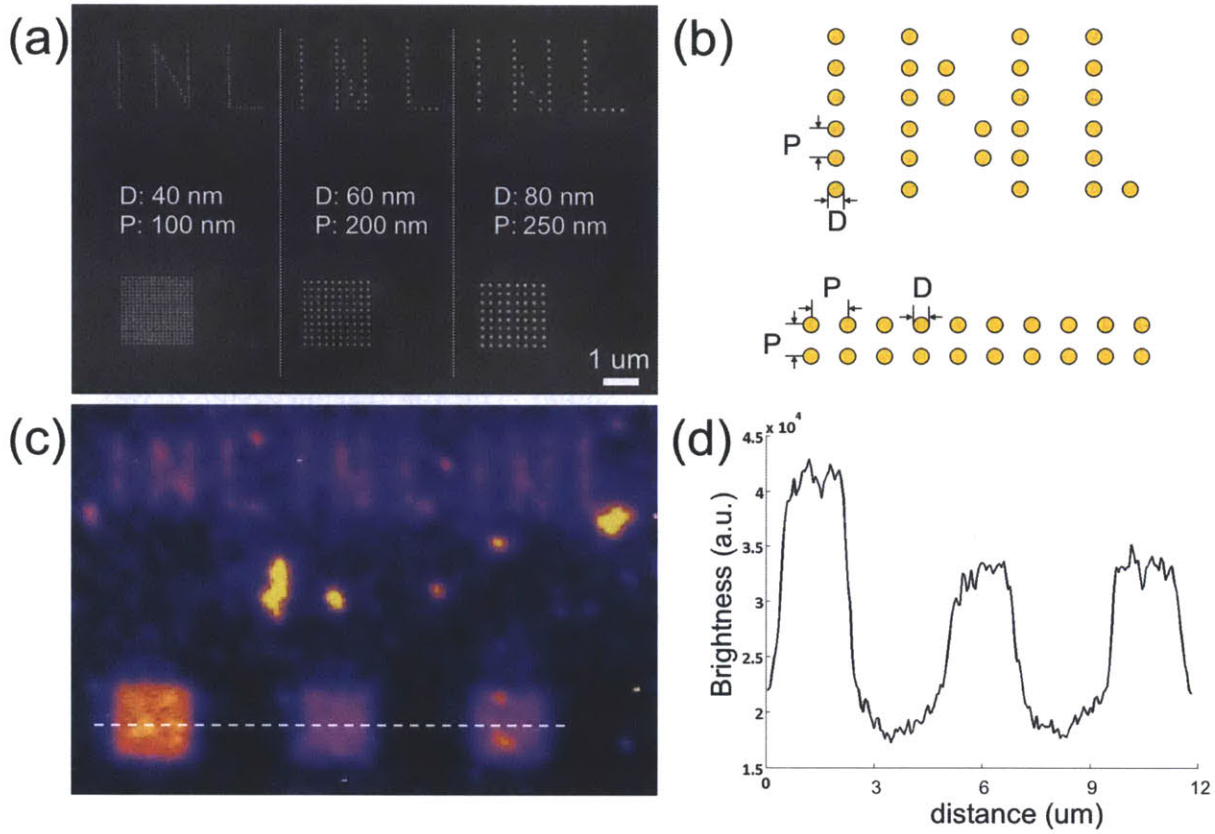

Figure 4-5. Fluorescence study of templated cortexillin. (a) SEM image of gold nanodot arrays with various diameters and pitches. (b) Schematic diagram showing the arrangement of the gold nanodot patterns shown in (a). (c) Fluorescence micrograph of gold nanodot patterns incubated with cortexillin, first antibody, and FITC-tagged second antibody. (d) Fluoroscence intensity profile across the dotted line in (c).

We first demonstrated that the proteins can be selectively attached to a gold nanostructure. Gold nanodots arrays with diameter ranging from 40 nm to 80 nm and periodicity ranging from 100 nm to 250 nm were incubated with a solution of cortexillin $I_{272-352}$ for 3 hours and then incubated with a solution of anti-FLAG rabbit IgG antibody (primary antibody) and anti-rabbit-IgG antibody (secondary antibody). The primary

antibody would bind to the FLAG residues in cortexillin $I_{272-352}$, and the secondary antibody, which has a fluorophore, would bind to the primary antibody. The substrate was imaged using a conventional fluorescence microscope. Figure 4-5(a) shows SEM image of the gold nanostructures and figure 4-5(b) shows schematic diagram showing the arrangement of the gold nanostructures. Figure 4-5(c) shows the fluorescence micrograph. Bright color yellow color represents strong fluorescence signal and dark purple color represents weak fluorescence signal. The fluorescence signal was strong around the gold nanostructures and letter made of a single column of gold nanostructures with a diameter of 40 nm was visible. When the fluorescence signals from gold nanostructure arrays with different diameters and pitches were compared, the fluorescence signal was proportional to the surface area of the gold. This result shows that the attachment of proteins to the gold nanostructures were mediated by specific surface interaction.

4.3.3 Gap size measurement of templated cortexillin

Next, we used gold nanoparticles to observe proteins attached to the gold nanostructures at single-molecular level. Substrate with gold nanodots with diameters ranging from 70 nm to 100 nm were first incubated with cortexillin $I_{272-352}$ and then incubated with Ni-NTA gold nanoparticles with a diameter of 5 nm. Then the sample was rinsed by a buffer solution and dried by nitrogen gun blow. Figure 4-6(a) shows a SEM image of the gold nanodots after the drying. As shown in Figure 4-6(a), the gold nanoparticles were assembled around the gold nanodots with a non-zero spacing between the sidewall of the gold nanodots and the gold nanoparticles. Figure 4-6(b)

shows a distribution of the size of the spacing. The average of the spacings was 9.2 nm, which is slightly shorter than the expected end-to-end length of cortexillin $I_{272-352}$. Instead, there was a pick at 14 nm, which is the expected end-to-end length of cortexillin $I_{272-352}$.

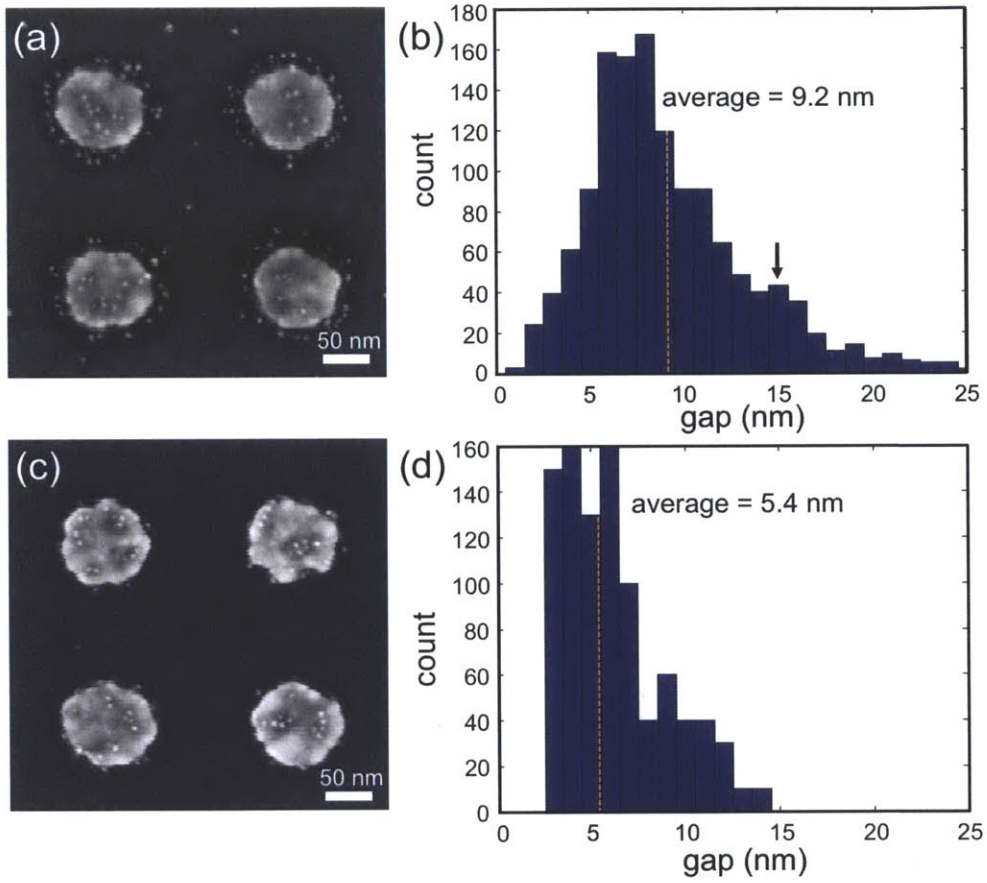

Figure 4-6. Cortexillin templated by gold nanodots at room temperature and high temperature. (a,c) SEM images of gold nanodots incubated with cortexillin and gold nanoparticles at (a) room temperature; and (c) 80°C. (b,d) Histograms showing the distribution of the gaps between the gold nanodots and cortexillin incubated at (a) room temperature; and (d) 80 °C.

We also tested the assembly of proteins at high temperature. When cortexillin $I_{272-352}$ was incubated with gold nanostructures at 80 °C, which was higher than the melting temperature of cortexillin $I_{272-352}$, the gold nanoparticles were assembled around the gold nanodots with almost-zero gap, as shown in Figure 4-6(c). At temperature higher than the melting temperature of a protein, a protein agglomerates and forms a globular shape instead of maintaining its native 3-D structure. As a result, the gold nanoparticles attached to the N-terminal of cortexillin $I_{272-352}$ were assembled around the gold nanodots with much smaller spacing. The average of the spacings was 5 nm, as shown in Figure 4-6(d). There was no gold nanoparticles assembled around the gold nanodots with a gap of 14 nm, when cortexillin $I_{272-352}$ was incubated at 80 °C.

4.3.4 Gap size measurement of templated tropomyosin

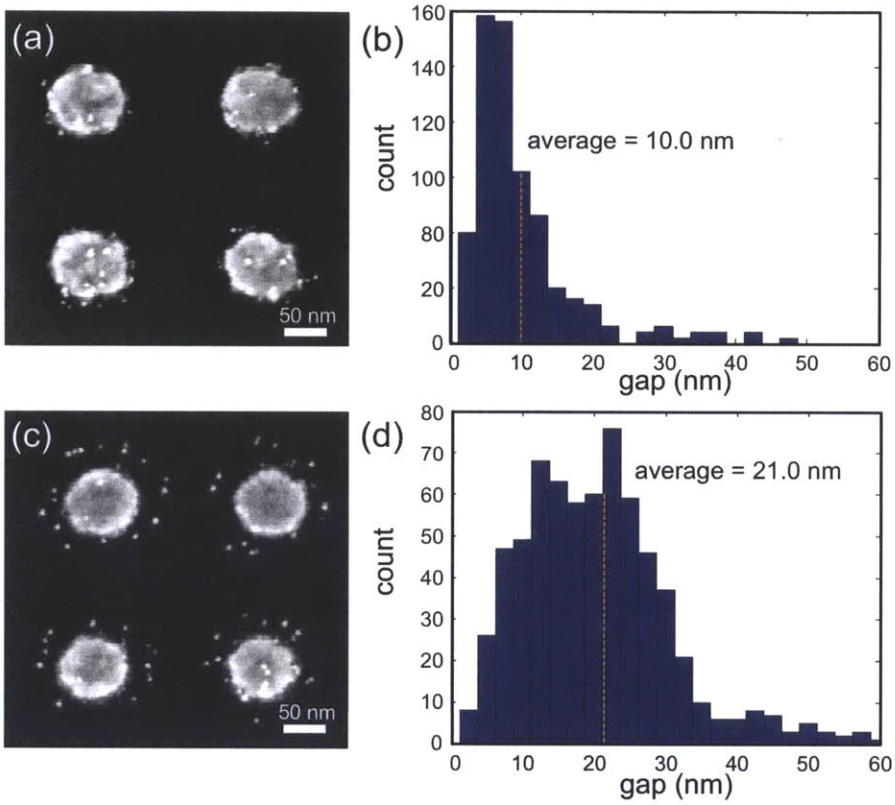

Figure 4-7. Native and C190A tropomyosin templated by gold nanodots. (a,c) SEM images of gold nanodots incubated with (a) native tropomyosin and gold nanoparticles; and (b) C190A tropomyosin and gold nanoparticles. (b,d) Histograms showing the distribution of the gaps between the gold nanodots and (b) native tropomyosin; and (d) C190A tropomyosin.

To further study how the proteins are assembled around the gold nanostructure (or to gain insight about), we used a longer proteins, tropomyosin. When a native tropomyosin was incubated with gold nanodots and gold nanoparticles, the gold nanoparticles were assembled around the gold nanodots with a gap spacing of 10 nm, as shown in Figure 4-

7(a,b). There was only few gold particles were assembled around the gold nanodots with a gap spacing of 40 nm or around 40 nm, which is the expected end-to-end distance of tropomyosin. When a mutated tropomyosin C190A tropomyosin, in which an internal cysteine was replaced with alanine, was incubated with gold nanodots and gold nanoparticles, the gold nanoparticles were assembled around the gold nanodots with larger gap spacing, as shown in Figure 4-7(c,d). The average of the gap spacings was 21 nm, which is half of the expected end-to-end length of tropomyosin.

4.3.5 Higher control of the proteins by using gold trenches

To achieve the control of not only the placement but also the orientation of proteins, we used gold trenches. The gold trenches were fabricated with same procedure used for fabricating gold nanodots arrays. To test how the orientation of the proteins changes depending on the width of the gold trenches, we fabricated two rectangular gold pads, in which one gold pad is slightly tilted relative to the other gold pad. As a result, gold nanotrenches with a trench width ranging from 40 nm to 100 nm was achieved. When the gold nanotrench was incubated with C190A tropomyosin and gold nanoparticles, the assembly of the gold nanoparticles changed depending on the width of the trench. As shown in Figure 4-8(a), the gold nanoparticles were aligned at the center of the trench when the trench width was 68 nm, which is slightly shorter than the expected end-to-end distance of C190A tropomyosin. However, when the trench width was narrower than 68 nm, gold particles were aligned at the center of the trench, instead their positions were deviated from the center of the trench, as shown in Figure 4-8(b). When the trench width was wider than 68 nm, the gold nanoparticles stick to the either side

the the trench, as shown in Figure 4-8(c-e). To quantify the degree of alignement of the gold nanoparticles at the center of the trench, we defined delta as the difference between the gap spacing of the nanoparticles to the two sides of the trench. Figure 4-8(f) shows the distribution of the delta depending on the width of the trench. The delta is 0 if the gold nanoparticles are aligned at the center of the trench, and it is same to the trench width, if the gold nanoparticles stick to the either side of the trench. As shown in Figure 4-8(f), the delta generally increased as the trench width increased.

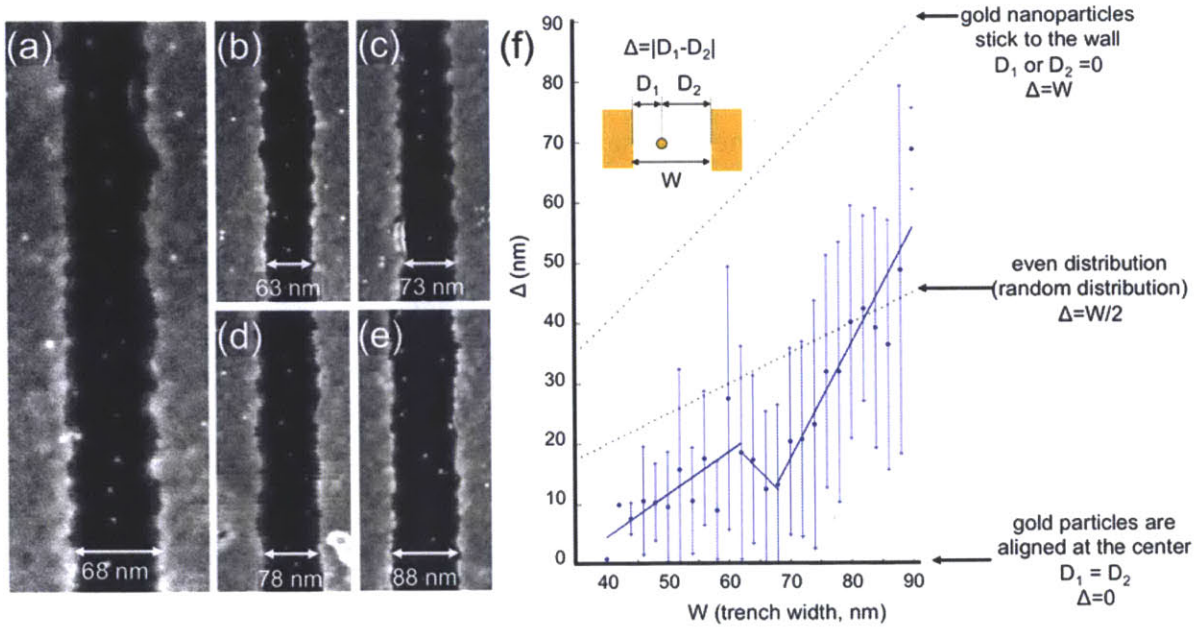

Figure 4-8. C190A tropomyosin templated by a gold trench. (a-e) SEM images of gold trenches incubated with C190A tropomyosin and gold nanoparticles. The width of the trenches are (a) 68 nm; (b) 63 nm; (c) 73 nm; (d) 78 nm; and (e) 88 nm. (f) Statistical result showing how delta changed depending on the trench width. Delta was defined by the difference of the gaps between a nanoparticle and two walls of the trench.

4.3.6 Discussion

We demonstrated the placement control of proteins by using gold nanostructures and two coiled-coil proteins. We used a cysteine residue of a protein to direct the attachment of the proteins to gold nanostructures. By using a fluorescence microscope, we showed that the proteins were localized around the nanostructures. We also observed an individual protein with a SEM by attaching gold nanoparticles to the proteins. Finally, we achieved more precise placement control of proteins by using a gold trench. The placement control and visualization method developed in this program could be easily applied to another proteins. We expect that the techniques developed in this program could be used for studying biological phenomena at a single molecular level or developing an ultra-sensitive biomedical sensors or devices.

5. Summary and future direction

Topographic templates can be used for guiding the self-assembly of block copolymers to produce complex nanoscale patterns. In our previous work, regular patterns were achieved by using a polystyrene-*b*-polydimethylsiloxane (PS-*b*-PDMS) block copolymer and topographic templates. We applied the similar approach to achieve long-range ordered sub-10-nm line patterns by using a 16 kg/mol PS-b-PDMS block copolymer. Template height and diameter effect on the orientation of the block copolymer was studied. To achieve more diverse patterns, such as dot patterns with square symmetry, a triblock terpolymer was used. By using topographic templates to control the self-assembly of PI-*b*-PS-*b*-PFS triblock terpolymer, we achieved a long-range ordered dot patterns with square symmetry. Also, to achieve more complex patterns, such as a dot-line hybrid pattern, we cross-linked a solvent-annealed block copolymer film with electron-beam exposure and performed a second solvent annealing with a different annealing condition. By fine-tuning a topographic template array, we successfully achieved a long-range ordered dot-line hybrid patterns.

Despite that the block copolymer self-assembly had been heavily studied, researchers had yet to ascertain how to design nanostructures to achieve a desired target pattern using block copolymers, because, more complex block-copolymer patterns required similarly complex templates. As a result, a complex circuit-layout pattern over a large area can only be achieved using a template with many different and non-periodic features. To address this problem, we developed a modular method that greatly

simplifies the template design. By developing design cells from a simple square grid of single posts and concatenating the design cells, it was possible to design a template to achieve a complex target pattern. This approach, template design based on a restricted set of tiles with post motifs provides a way to achieve a target pattern of line segments with bends and terminations from a relatively simple template. Several groups have already demonstrated fabrication of simple bends or jogs by guiding block-copolymer microdomains to follow a topographic or chemical template. However, no one has yet combined arbitrary assemblies of dense bends and jogs in a single pattern, in large part because no one knew how to design templates for such complex patterns.

The method shown in this thesis used a topographic template consisting of a square lattice of posts with a restricted set of post motifs. Since a finite number of post motifs are considered, block-copolymer patterns from all possible square geometry templates with these post motifs can be studied. We used a sparse array of double posts distributed among a dense array of single posts. One out of every nine single posts was replaced with a double post. When this template was used to guide a 45.5 kg/mol PS-*b*-PDMS block copolymer, the PDMS cylinders that assembled over double posts were aligned parallel to the double post direction. However, the orientation of the PDMS cylinders assembled over single posts depended on the orientations of the neighboring four double posts. We first studied PDMS cylinders surrounded by two double posts and found that termination or bend was formed depending on the orientations of the surrounding two double posts. By applying these observations, we predicted the possible block-copolymer patterns surrounded by four double posts. Each double post can be

aligned along one of the two directions with 16 (2^4) combinations of the orientations of the four double posts. These 16 combinations can be grouped into four nonequivalent arrangements. On each arrangement, various block copolymer patterns were observed. For a Y^4, X^2Y^2, and XY^3 post arrangement, the most frequently observed patterns matched the predicted patterns and the reproducibility were 100%, 64%, and 60% respectively. For an YXYX arrangement, the predicted pattern was not observed. When the free energy of these five patterns were calculated by using a SCFT simulation, the pattern observed with a lower count had a higher energy than the pattern found most often. To demonstrate that patterns needed for components of integrated circuits (IC) can be fabricated based on our rules, we fabricated an array of bends, one of the essential components of an IC layout.

The key innovation is the use of a binary set of tiles that can be used to very simply cover the desired patterning area. Despite the simplicity of the approach, by exploiting neighbor-neighbor interactions of the tiles, a complex final pattern can be formed. The vision is thus one of programmability of patterning by using a simple instruction set. This development will thus be of interest to scientists and engineers across many fields involving self-assembly, including biomolecule, quantum-dot or nanowire positioning; algorithmic self-assembly; and integrated-circuit development. The specific strategy (based on a binary set of tiles on a 3×3 grid of template posts) that we demonstrated is only one of many possible such tiling strategies, and so we expect that this paper will spark interest in finding new and optimum strategies for rule-based cellular approaches to the directed self-assembly of block copolymers and other self-assembling material

systems. This approach, starting from a degenerate template, adding a restricted set of perturbations, and developing rules for all possible perturbation arrangements, could potentially be applied to other self-assembling systems that can be templated by topographic or chemical features.

We also showed that proteins can be attached to a metal surface through gold-cysteine interaction. There have been many studies on patterning proteins in micron length scale, but only few studies successfully showed protein patterning at the single-molecule level. Also, in those studies, the details of the assembly of the proteins around the nanostructures were not studied. Here, we used a cysteine residue of a protein to direct the attachment of the proteins to gold nanostructures. By using relatively long and stiff proteins (coiled-coil proteins), we studied how the proteins were assembled around the patterned nanostructures. We also showed that higher control of the proteins can be achieved by using more complex nanostructures, such as gold trenches. We believe that the method developed in this study could be applied to diverse proteins and DNA origami structures.

6. Appendix

We developed an image analysis software to measure the area fractions of the block copolymer grains. Here is the code of the software.

6.1 Image analysis code for measuring the area fractions of polymer grains

An Image analysis software was developed to measure the area fraction of polymer grains formed on a patterned substrate. The program first transforms a SEM image of PDMS patterns to a grey scale image and after that further processes the image and measures the area fractions of polymer grains oriented along various directions.

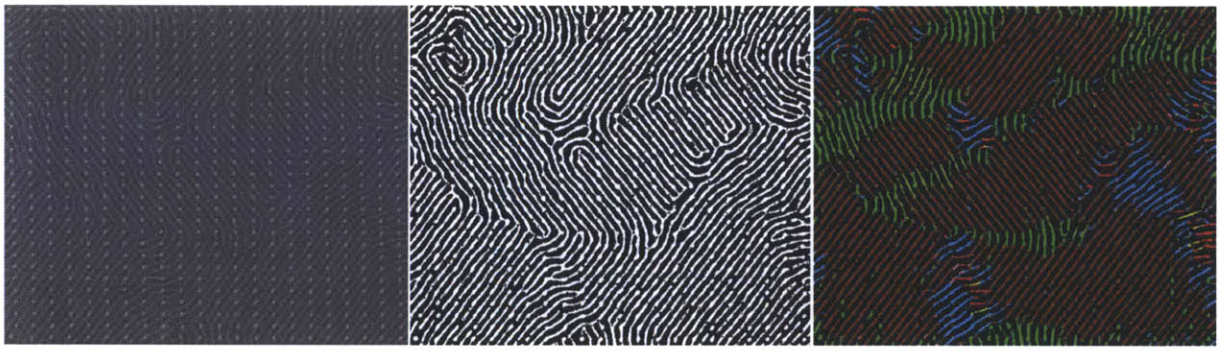

Figure 6.1 SEM image of PDMS patterns, greyscale version of the image, and image showing grains oriented along different directions with different colors.

The software was written with MATLAB and it consists of 5 m files. cylin_test.m is the main file and it has the filename of file to be analyzed as an input.

6.1.1 cylin_test.m

```
function cylin_test(filename)

x=[0:1:256];
```

```
warning off all
close all

deltax=round(70/200*128);
deltay=round(70/200*128/1.5);

image=imread(filename);
original_img=image;
original_img3(:,:,1)=original_img(:,:);
original_img3(:,:,2)=original_img(:,:);
original_img3(:,:,3)=original_img(:,:);
original_img3(:,:,:)=0;
original_img2=original_img3;
img=original_img;

pixel=zeros(1,size(img,1)*size(img,2));
k=0;

for i=1:size(img,1)
  for j=1:size(img,2)
    k=k+1;
    pixel(1,k)=img(i,j);
  end
end

first_max=0;
first_min=0;

for i=90:255
  if first_max==0;
    if size(find(pixel(:,:)==i),2)>size(find(pixel(:,:)==i+1),2);
      first_max=i;
```

```
    end
  else
    if first_min==0 && size(find(pixel(:,:)==i),2)<size(find(pixel(:,:)==i+1),2);
      first_min=i;
    end
  end
end

image=img;
sum=uint32(img);
sum(:,:)=0;
num_picture=0;

for i=-1:2
  num_picture=num_picture+1;
  img=image;

  temp=i;

  img(find(img(:,:)<=first_min+temp))=0;
  img(find(img(:,:)>first_min+temp))=255;
  se=strel('disk',1);

  img=imclose(img,se);
  img=imopen(img,se);

  sum(:,:)=sum(:,:)+uint32(img(:,:));
  [labeled,numObjects]=bwlabel(img,4);
end

temp=uint8(sum(:,:)/num_picture);
image(find(temp(:,:)<60))=0;
```

```
image(find(temp(:,:)>60))=255;
[labeled,numObjects]=bwlabel(image,4);
graindata=regionprops(labeled,'Area');
temp=labeled;

for i=1:numObjects
  if graindata(i).Area<=20
    temp(find(labeled(:,:)==i))=0;
  end
end

board=zeros(size(labeled,1),size(labeled,2),10);
for i=1:size(board,3)
  board(:,:,i)=labeled;
end

board(:,:,:)=0;

[labeled,numObjects]=bwlabel(temp,4);
graindata=regionprops(labeled,'Area');
temp=labeled;
figure;imshow(temp);
pause

temp2=temp;

colormap=zeros(14,3);
colormap(1,:)=[255 0 0];
colormap(2,:)=[0 255 0];
colormap(3,:)=[255 255 0];
colormap(4,:)=[0 176 240];
colormap(5,:)=[161 77 7];
```

```
colormap(6,:)=[146 208 80];
colormap(7,:)=[255 153 204];
colormap(8,:)=[102 0 255];
colormap(9,:)=[204 0 204];
colormap(10,:)=[0 0 0];

temp(find(temp(:,:)~=0))=1;
for i=1:numObjects
  [i numObjects]
  temp=temp2;
  temp(find(temp(:,:)~=i))=0;
  xyc=cylin_test3(temp,deltax,deltay,5);

  for j=1:size(xyc,1)

    original_img3(xyc(j,2),xyc(j,1),:)=0;
    original_img3(xyc(j,2),xyc(j,1),:)=colormap(xyc(j,3),:);

    board(xyc(j,2),xyc(j,1),xyc(j,3))=1;

  end
end

for i=1:size(board,3)
  board(:,:,i)=remove_small(board(:,:,i));
end

for x=1:size(original_img2,2)
  for y=1:size(original_img2,1)
    for c=1:size(board,3)

      if board(y,x,c)~=0; original_img2(y,x,:)=colormap(c,:); end
```

```
    end


  end
end

result_filename=[filename 'i' '.' 't' 'i' 'f'];
imwrite(original_img2,result_filename,'tif');
area=zeros(size(board,3),1);

for i=1:size(original_img2,1)
  for j=1:size(original_img2,2)
    for k=1:size(board,3)-1
      if original_img2(i,j,1)==colormap(k,1) && original_img2(i,j,2)==colormap(k,2)
&& original_img2(i,j,3)==colormap(k,3)
        area(k,1)=area(k,1)+1;
      end
    end


  end
end
total_area=0;
for k=1:size(board,3)-1
  total_area=total_area+area(k,1);
end

area_fraction=double(area(1:size(board,3)-1,1))/double(total_area)*100
area_fraction_filename=[filename 'a' '.' 'd' 'a' 't'];
dlmwrite(area_fraction_filename,area_fraction);
```

6.1.2 cylin_test3.m

```
function xyc=cylin_test3(output,deltax,deltay,width)

[m n]=find(output~=0);
xy=[m n];
xyc=zeros(size(m,1),3);
xyc(:,1:2)=xy(:,1:2);

y10=convolution(output,1,0,deltax,deltay,width);
y01=convolution(output,0,1,deltax,deltay,width);
y11=convolution(output,1,1,deltax,deltay,width);
y21=convolution(output,2,1,deltax,deltay,width);
y12=convolution(output,1,2,deltax,deltay,width);
y13=convolution(output,1,3,deltax,deltay,width);
y23=convolution(output,2,3,deltax,deltay,width);
y31=convolution(output,3,1,deltax,deltay,width);
y32=convolution(output,3,2,deltax,deltay,width);

y(:,:,1)=y10;
y(:,:,2)=y01;
y(:,:,3)=y21;
y(:,:,4)=y11;
y(:,:,5)=y12;
y(:,:,6)=y13;
y(:,:,7)=y23;
y(:,:,8)=y31;
y(:,:,9)=y32;

z=y;

for i=1:size(m,1)
```

```
    x=xy(i,2);
    y=xy(i,1);
    maximum=0;
    n=0;
    for k=1:size(z,3)
      if z(y,x,k)>maximum;
        n=k;
        maximum=z(y,x,k);
      end
    end

    xyc(i,1)=x;
    xyc(i,2)=y;

    if maximum>0.6


    xyc(i,3)=n;

    else
      xyc(i,3)=10;
    end
end
```

6.1.3 convolution.m

```
function convoluted_image=convolution(image,i,j,deltax,deltay,width)

[positive_filter,negative_filter, filter_size]=make_filter(deltax,deltay,width,i,j);
positive_result=conv2(image,positive_filter,'same');
negative_result=conv2(image,negative_filter,'same');
```

```
for x=1:size(positive_result,2)
  for y=1:size(positive_result,1)
    if positive_result(y,x)<negative_result(y,x)
      positive_result(y,x)=negative_result(y,x);
    end
  end
end

convoluted_image=double(positive_result/filter_size);
```

6.1.4 make_filter.m

```
function [positive_filter,negative_filter, filter_size]=make_filter(deltax,deltay,width,i,j)

if i==1 && j==0
  filter=zeros(width,deltax);
  filter(:,:)=1;
  positive_filter=filter;
  negative_filter=filter;
elseif i==0 && j==1
  filter=zeros(deltay,width);
  filter(:,:)=1;
  positive_filter=filter;
  negative_filter=filter;
else
  length=round((((i*deltax)^2+(j*deltay)^2)^(1/2)));
  filter=zeros(width,length);
  filter(:,:)=1;
  positive_filter=imrotate(filter,180/pi*atan((j*deltay)/(i*deltax)));
  negative_filter=imrotate(filter,-180/pi*atan((j*deltay)/(i*deltax)));
end
```

```
[m n]=size(find(positive_filter(:,:)~=0));
filter_size=m*n;
```

6.1.5 remove_small.m

```
function output=remove_small(img)

se=strel('disk',1);
output=imopen(img,se);
output=imclose(output,se);
```

7. References

1. Winston, D. *et al.* Neon Ion Beam Lithography (NIBL). *Nano Lett.* **11,** 4343–7 (2011).

2. Winston, D. *et al.* Scanning-helium-ion-beam lithography with hydrogen silsesquioxane resist. *J. Vac. Sci. Technol. B Microelectron. Nanom. Struct.* **27,** 2702 (2009).

3. Yang, J. K. W. *et al.* Understanding of hydrogen silsesquioxane electron resist for sub-5-nm-half-pitch lithography. *J. Vac. Sci. Technol. B Microelectron. Nanom. Struct.* **27,** 2622 (2009).

4. Wagner, C. & Harned, N. EUV lithography: Lithography gets extreme. *Nat. Photonics* **4,** 24–26 (2010).

5. Schift, H. Nanoimprint lithography: An old story in modern times? A review. *J. Vac. Sci. Technol. B Microelectron. Nanom. Struct.* **26,** 458 (2008).

6. Bita, I. *et al.* Graphoepitaxy of self-assembled block copolymers on two-dimensional periodic patterned templates. *Science* **321,** 939–43 (2008).

7. Yang, J. K. W. *et al.* Complex self-assembled patterns using sparse commensurate templates with locally varying motifs. *Nat. Nanotechnol.* **5,** 256–60 (2010).

8. Cheng, J. Y., Mayes, A. M. & Ross, C. a. Nanostructure engineering by templated self-assembly of block copolymers. *Nat. Mater.* **3,** 823–8 (2004).

9. Jung, Y. S., Chang, J. B., Verploegen, E., Berggren, K. K. & Ross, C. a. A path to ultranarrow patterns using self-assembled lithography. *Nano Lett.* **10,** 1000–5 (2010).

10. Hirai, T. *et al.* One-Step Direct-Patterning Template Utilizing Self-Assembly of POSS-Containing Block Copolymers. *Adv. Mater.* **21,** 4334–4338 (2009).

11. Xu, J. *et al.* Fabrication of silicon oxide nanodots with an areal density beyond 1 teradots inch(-2). *Adv. Mater.* **23,** 5755–61 (2011).

12. Popa, A.-M., Niedermann, P., Heinzelmann, H., Hubbell, J. a & Pugin, R. Fabrication of nanopore arrays and ultrathin silicon nitride membranes by block-copolymer-assisted lithography. *Nanotechnology* **20,** 485303 (2009).

13. Pease, R. F. To charge or not to charge: 50 years of lithographic choices. *J. Vac. Sci. Technol. B Microelectron. Nanom. Struct.* **28,** C6A1 (2010).

14. Bang, J., Jeong, U., Ryu, D. Y., Russell, T. P. & Hawker, C. J. Block copolymer nanolithography: translation of molecular level control to nanoscale patterns. *Adv. Mater.* **21,** 4769–92 (2009).

15. Lu, W. & Lieber, C. M. Nanoelectronics from the bottom up. *Nat. Mater.* **6,** 841–50 (2007).

16. Baxter, J. *et al.* Nanoscale design to enable the revolution in renewable energy. *Energy Environ. Sci.* **2,** 559 (2009).

17. Arlett, J. L., Myers, E. B. & Roukes, M. L. Comparative advantages of mechanical biosensors. *Nat. Nanotechnol.* **6,** 203–15 (2011).

18. Ozbay, E. Plasmonics: merging photonics and electronics at nanoscale dimensions. *Science* **311,** 189–93 (2006).

19. Bunch, J. S. News: Putting a damper on nanoresonators. *Nat. Nanotechnol.* **6,** 331–2 (2011).

20. Yang, Y.-L., Hsu, C.-C., Chang, T.-L., Kuo, L.-S. & Chen, P.-H. Study on wetting properties of periodical nanopatterns by a combinative technique of photolithography and laser interference lithography. *Appl. Surf. Sci.* **256,** 3683–3687 (2010).

21. Bowden, N. Self-Assembly of Mesoscale Objects into Ordered Two-Dimensional Arrays. *Science (80-.).* **276,** 233–235 (1997).

22. Barth, J. V *et al.* Stereochemical effects in supramolecular self-assembly at surfaces: 1-D versus 2-D enantiomorphic ordering for PVBA and PEBA on Ag(111). *J. Am. Chem. Soc.* **124,** 7991–8000 (2002).

23. Pokroy, B., Kang, S. H., Mahadevan, L. & Aizenberg, J. Self-organization of a mesoscale bristle into ordered, hierarchical helical assemblies. *Science* **323,** 237–40 (2009).

24. Teranishi, T., Hasegawa, S., Shimizu, T. & Miyake, M. Heat-Induced Size Evolution of Gold Nanoparticles in the Solid State. *Adv. Mater.* **13,** 1699–1701 (2001).

25. Whitesides, G. M., Mathias, J. P. & Seto, C. T. Molecular self-assembly and nanochemistry: a chemical strategy for the synthesis of nanostructures. *Science* **254,** 1312–9 (1991).

26. Hartgerink, J. D., Beniash, E. & Stupp, S. I. Self-assembly and mineralization of peptide-amphiphile nanofibers. *Science* **294,** 1684–8 (2001).

27. Andres, R. P. *et al.* Self-Assembly of a Two-Dimensional Superlattice of Molecularly Linked Metal Clusters. **43,** (1987).

28. Pacholski, C., Kornowski, A. & Weller, H. Self-assembly of ZnO: from nanodots to nanorods. *Angew. Chem. Int. Ed. Engl.* **41,** 1188–91 (2002).

29. Jenekhe, S. a. Self-Assembly of Ordered Microporous Materials from Rod-Coil Block Copolymers. *Science (80-.).* **283,** 372–375 (1999).

30. Kato, T. Self-Assembly of Phase-Segregated Liquid Crystal Structures. **2414,** (2013).

31. Rothemund, P. W. K. Folding DNA to create nanoscale shapes and patterns. *Nature* **440,** 297–302 (2006).

32. Duan, H. & Berggren, K. K. Directed self-assembly at the 10 nm scale by using capillary force-induced nanocohesion. *Nano Lett.* **10,** 3710–6 (2010).

33. Hung, A. M. *et al.* Large-area spatially ordered arrays of gold nanoparticles directed by lithographically confined DNA origami. *Nat. Nanotechnol.* **5,** 121–6 (2010).

34. Xia, Y., Yin, Y., Lu, Y. & McLellan, J. Template-Assisted Self-Assembly of Spherical Colloids into Complex and Controllable Structures. *Adv. Funct. Mater.* **13,** 907–918 (2003).

35. Tzeng, S.-D., Lin, K.-J., Hu, J.-C., Chen, L.-J. & Gwo, S. Templated Self-Assembly of Colloidal Nanoparticles Controlled by Electrostatic Nanopatterning on a Si3N4/SiO2/Si Electret. *Adv. Mater.* **18,** 1147–1151 (2006).

36. Stoykovich, M. P. *et al.* Directed Self-Assembly of Block Copolymers for Nanolithography : Essential Integrated Circuit Geometries. **1,** 168–175

37. Lu, B. N. *et al.* Fabrication of Chemically Patterned Surfaces. 1812–1815 (2002).

38. He, H. X. *et al.* Fabrication of Designed Architectures of Au Nanoparticles on Solid Substrate with Printed Self-Assembled Monolayers as Templates. 3846–3851 (2000).

39. Cheng, J. Y., Zhang, F., Smith, H. I., Vancso, G. J. & Ross, C. a. Pattern Registration Between Spherical Block-Copolymer Domains and Topographical Templates. *Adv. Mater.* **18,** 597–601 (2006).

40. Cheng, J. Y., Mayes, A. M. & Ross, C. a. Nanostructure engineering by templated self-assembly of block copolymers. *Nat. Mater.* **3,** 823–8 (2004).

41. Liu, S., Maoz, R. & Sagiv, J. Template Guided Self-Assembly of [Au 55] Clusters on Nanolithographically Defined Monolayer Patterns. 10–15 (2002).

42. Sharma, J., Chhabra, R., Liu, Y., Ke, Y. & Yan, H. DNA-templated self-assembly of two-dimensional and periodical gold nanoparticle arrays. *Angew. Chem. Int. Ed. Engl.* **45,** 730–5 (2006).

43. Liu, S., Maoz, R., Sagiv, J. & Reho, V. Planned Nanostructures of Colloidal Gold via Self-Assembly on Hierarchically Assembled Organic Bilayer Template Patterns with In-situ Generated Terminal Amino Functionality. (2004).

44. Zehner, R. W. & Sita, L. R. Electroless Deposition of Nanoscale Copper Patterns via Microphase-Separated Diblock Copolymer Templated Self-Assembly. 6139–6141 (1999).

45. Yin, Y., Lu, Y., Gates, B. & Xia, Y. Template-assisted self-assembly: a practical route to complex aggregates of monodispersed colloids with well-defined sizes, shapes, and structures. *J. Am. Chem. Soc.* **123,** 8718–29 (2001).

46. Stoykovich, M. P. *et al.* Directed assembly of block copolymer blends into nonregular device-oriented structures. *Science* **308,** 1442–6 (2005).

47. Sato, K. & Hisano, S. Chemically Synthesized L1 0 -Type FePt Nanoparticles. **41,** 660–664 (2005).

48. Chen, X., Rogach, A. L., Talapin, D. V, Fuchs, H. & Chi, L. Hierarchical luminescence patterning based on multiscaled self-assembly. *J. Am. Chem. Soc.* **128,** 9592–3 (2006).

49. Cui, Y. *et al.* Integration of Colloidal Nanocrystals into Lithographically Patterned Devices. (2004).

50. Varghese, B. *et al.* Size selective assembly of colloidal particles on a template by directed self-assembly technique. *Langmuir* **22,** 8248–52 (2006).

51. Song, L. *et al.* Facile Microstructuring of Organic Semiconducting Polymers by the Breath Figure Method: Hexagonally Ordered Bubble Arrays in Rigid Rod-Polymers. *Adv. Mater.* **16,** 115–118 (2004).

52. Kim, S. O. *et al.* Epitaxial self-assembly of block copolymers on lithographically defined nanopatterned substrates. *Nature* **424,** 411–4 (2003).

53. Son, J. G., Chang, J.-B., Berggren, K. K. & Ross, C. a. Assembly of sub-10-nm block copolymer patterns with mixed morphology and period using electron irradiation and solvent annealing. *Nano Lett.* **11,** 5079–84 (2011).

54. Bates, F. S. & Fredrickson, G. H. Block copolymer thermodynamics: theory and experiment. *Annu. Rev. Phys. Chem.* **41,** 525–57 (1990).

55. Darling, S. B. Directing the self-assembly of block copolymers. *Prog. Polym. Sci.* **32,** 1152–1204 (2007).

56. Bates, F. S. & Fredrickson, G. H. Block Copolymers—Designer Soft Materials. *Phys. Today* **52,** 32 (1999).

57. Jung, Y. S. & Ross, C. a. Orientation-controlled self-assembled nanolithography using a polystyrene-polydimethylsiloxane block copolymer. *Nano Lett.* **7,** 2046–50 (2007).

58. Yang, J. K. W. & Berggren, K. K. Using high-contrast salty development of hydrogen silsesquioxane for sub-10-nm half-pitch lithography. *J. Vac. Sci. Technol. B Microelectron. Nanom. Struct.* **25,** 2025 (2007).

59. Bergmair, I. *et al.* Single and multilayer metamaterials fabricated by nanoimprint lithography. *Nanotechnology* **22,** 325301 (2011).

60. Chang, L.-W., Bencher, C. & Philip Wong, H.-S. Experimental demonstration of aperiodic patterns of directed self-assembly by block copolymer lithography for random logic circuit layout. *2010 Int. Electron Devices Meet.* **2,** 33.2.1–33.2.4 (2010).

61. Hellwig, O. *et al.* Bit patterned media based on block copolymer directed assembly with narrow magnetic switching field distribution. *Appl. Phys. Lett.* **96,** 052511 (2010).

62. Tsai, H.-Y. *et al.* Sub-30 nm pitch line-space patterning of semiconductor and dielectric materials using directed self-assembly. *J. Vac. Sci. Technol. B Microelectron. Nanom. Struct.* **30,** 06F205 (2012).

63. Lithography, B. C. *et al.* Formation of a Cobalt Magnetic Dot Array via. 1174–1178 (2001).

64. Black, C. T. Self-aligned self assembly of multi-nanowire silicon field effect transistors. *Appl. Phys. Lett.* **87,** 163116 (2005).

65. Liu, G. *et al.* Epitaxial graphene nanoribbon array fabrication using BCP-assisted nanolithography. *ACS Nano* **6,** 6786–92 (2012).

66. Lee, J. *et al.* Uniform graphene quantum dots patterned from self-assembled silica nanodots. *Nano Lett.* **12,** 6078–83 (2012).

67. Jung, Y. S. & Ross, C. a. Well-ordered thin-film nanopore arrays formed using a block-copolymer template. *Small* **5,** 1654–9 (2009).

68. Stefik, M. *et al.* sols. **21,** 5466–5473 (2010).

69. Simon, P. F. W., Ulrich, R., Spiess, H. W. & Wiesner, U. Block Copolymer - Ceramic Hybrid Materials from Organically Modified Ceramic Precursors. 3464–3486 (2001).

70. Toombes, G. E. S. *et al.* Self-Assembly of Four-Layer Woodpile Structure from Zigzag ABC Copolymer / Aluminosilicate Concertinas. 852–859 (2008).

71. Park, J. *et al.* Three-dimensional nanonetworks for giant stretchability in dielectrics and conductors. *Nat. Commun.* **3,** 916 (2012).

72. Moon, J. H. *et al.* Core-shell diamond-like silicon photonic crystals from 3D polymer templates created by holographic lithography. *Opt. Express* **14,** 6297–302 (2006).

73. Jin, W.-M. & Moon, J. H. Supported pyrolysis for lithographically defined 3D carbon microstructures. *J. Mater. Chem.* **21,** 14456 (2011).

74. Leiblert, L. Theory of Microphase Separation in Block Copolymers. **1617,** 1602–1617 (1980).

75. Lazzari, M. & López-Quintela, M. a. Block Copolymers as a Tool for Nanomaterial Fabrication. *Adv. Mater.* **15,** 1583–1594 (2003).

76. Tang, C. *et al.* Square Packing and Structural Arrangement of ABC Triblock Copolymer Spheres in Thin Films. *Macromolecules* **41,** 4328–4339 (2008).

77. Park, M. Block Copolymer Lithography: Periodic Arrays of 1011 Holes in 1 Square Centimeter. *Science (80-.).* **276,** 1401–1404 (1997).

78. Tang, C., Lennon, E. M., Fredrickson, G. H., Kramer, E. J. & Hawker, C. J. Evolution of Block Copolymer Square Arrays. **322,** 429–432 (2008).

79. Segalman, R., Hexemer, A. & Kramer, E. Edge Effects on the Order and Freezing of a 2D Array of Block Copolymer Spheres. *Phys. Rev. Lett.* **91,** 196101 (2003).

80. Son, J. G., Hannon, A. F., Gotrik, K. W., Alexander-Katz, A. & Ross, C. a. Hierarchical nanostructures by sequential self-assembly of styrene-dimethylsiloxane block copolymers of different periods. *Adv. Mater.* **23,** 634–9 (2011).

81. Cheng, J., Jung, W. & Ross, C. Magnetic nanostructures from block copolymer lithography: Hysteresis, thermal stability, and magnetoresistance. *Phys. Rev. B* **70,** 064417 (2004).

82. Thurn-Albrecht, T. Ultrahigh-Density Nanowire Arrays Grown in Self-Assembled Diblock Copolymer Templates. *Science (80-.).* **290,** 2126–2129 (2000).

83. Jung, Y. S., Jung, W., Tuller, H. L. & Ross, C. a. Nanowire conductive polymer gas sensor patterned using self-assembled block copolymer lithography. *Nano Lett.* **8,** 3776–80 (2008).

84. Naito, K., Hieda, H., Sakurai, M., Kamata, Y. & Asakawa, K. 2.5-Inch Disk Patterned Media Prepared By an Artificially Assisted Self-Assembling Method. *IEEE Trans. Magn.* **38,** 1949–1951 (2002).

85. Cheng, J. Y., Rettner, C. T., Sanders, D. P., Kim, H.-C. & Hinsberg, W. D. Dense Self-Assembly on Sparse Chemical Patterns: Rectifying and Multiplying Lithographic Patterns Using Block Copolymers. *Adv. Mater.* **20,** 3155–3158 (2008).

86. Ruiz, R. *et al.* Density multiplication and improved lithography by directed block copolymer assembly. *Science* **321,** 936–9 (2008).

87. Son, J. G., Bulliard, X., Kang, H., Nealey, P. F. & Char, K. Surfactant-Assisted Orientation of Thin Diblock Copolymer Films. *Adv. Mater.* **20,** 3643–3648 (2008).

88. Cheng, J. Y., Ross, C. a., Smith, H. I. & Thomas, E. L. Templated Self-Assembly of Block Copolymers: Top-Down Helps Bottom-Up. *Adv. Mater.* **18,** 2505–2521 (2006).

89. Black, C. T. & Bezencenet, O. Nanometer-Scale Pattern Registration and Alignment by Directed Diblock Copolymer Self-Assembly. *IEEE Trans. Nanotechnol.* **3,** 412–415 (2004).

90. Park, S. *et al.* Square-Inch Arrays from Block Copolymers with Lateral Order. *Science (80-.).* 1030–1033 (2009).

91. Jung, Y. S. & Ross, C. a. Solvent-Vapor-Induced Tunability of Self-Assembled Block Copolymer Patterns. *Adv. Mater.* **21,** 2540–2545 (2009).

92. Fredrickson, G. H. *The equilibrium theory of inhomogeneous polymers.* 203–276 (Oxford University press, 2006).

93. Alexander-Katz, A. & Fredrickson, G. H. Diblock Copolymer Thin Films: A Field-Theoretic Simulation Study. *Macromolecules* **40,** 4075–4087 (2007).

94. Mickiewicz, R. a. *et al.* Enhancing the Potential of Block Copolymer Lithography with Polymer Self-Consistent Field Theory Simulations. *Macromolecules* **43,** 8290–8295 (2010).

95. Stadler, R., Auschra, T. C., Beckmann, J. & Voigt-martin, I. Morphology and Thermodynamics of Symmetric Poly (A-block-B-block-C) Triblock Copolymers. 3080–3091 (1995).

96. Zheng, W. & Wane, Z. Morphology of ABC Triblock Copolymers. 7215–7223 (1996).

97. Ludwigs, S. *et al.* Self-assembly of functional nanostructures from ABC triblock copolymers. *Nat. Mater.* **2,** 744–7 (2003).

98. Chuang, V. P., Ross, C. a., Gwyther, J. & Manners, I. Self-Assembled Nanoscale Ring Arrays from a Polystyrene- b -polyferrocenylsilane- b -poly(2-vinylpyridine)Triblock Terpolymer Thin Film. *Adv. Mater.* **21,** 3789–3793 (2009).

99. Chuang, V. P., Gwyther, J., Mickiewicz, R. a, Manners, I. & Ross, C. a. Templated self-assembly of square symmetry arrays from an ABC triblock terpolymer. *Nano Lett.* **9,** 4364–9 (2009).

100. Ruiz, R., Dobisz, E. & Albrecht, T. R. Rectangular Patterns Using Block Bit Aspect Ratio Patterned Media. **5,** 79–84 (2011).

101. Park, S., Craig, G. S. W., La, Y., Solak, H. H. & Nealey, P. F. Square Arrays of Vertical Cylinders of PS- b -PMMA on Chemically Nanopatterned Surfaces. 5084–5094 (2007).

102. Tang, C. *et al.* Square Packing and Structural Arrangement of ABC Triblock Copolymer Spheres in Thin Films. *Macromolecules* **41,** 4328–4339 (2008).

103. Tang, C. *et al.* Thin Film Morphology of Block Copolymer Blends with Tunable Supramolecular Interactions for Lithographic Applications. *Macromolecules* **43,** 2880–2889 (2010).

104. Hur, S.-M., García-Cervera, C. J., Kramer, E. J. & Fredrickson, G. H. SCFT Simulations of Thin Film Blends of Block Copolymer and Homopolymer Laterally Confined in a Square Well. *Macromolecules* **42,** 5861–5872 (2009).

105. Bates, F. S. & Fredrickson, G. H. Block copolymer thermodynamics: theory and experiment. *Annu. Rev. Phys. Chem.* **41,** 525–57 (1990).

106. Edwards, E. W., Montague, M. F., Solak, H. H., Hawker, C. J. & Nealey, P. F. Precise Control over Molecular Dimensions of Block-Copolymer Domains Using the Interfacial Energy of Chemically Nanopatterned Substrates. *Adv. Mater.* **16,** 1315–1319 (2004).

107. Segalman, R. a. Patterning with block copolymer thin films. *Mater. Sci. Eng. R Reports* **48,** 191–226 (2005).

108. Park, C., Yoon, J. & Thomas, E. L. Enabling nanotechnology with self assembled block copolymer patterns. *Polymer (Guildf).* **44,** 6725–6760 (2003).

109. Bang, J. *et al.* Defect-Free Nanoporous Thin Films from ABC Triblock Copolymers. 7622–7629 (2006).

110. Bates, C. M. *et al.* Polarity-switching top coats enable orientation of sub-10-nm block copolymer domains. *Science* **338,** 775–9 (2012).

111. Bita, I. *et al.* Graphoepitaxy of self-assembled block copolymers on two-dimensional periodic patterned templates. *Science* **321,** 939–43 (2008).

112. Ding, B. *et al.* Interconnecting Gold Islands with DNA Origami Nanotubes. *Nano Lett.* 5065–5069 (2010). doi:10.1021/nl1033073

113. Chang, J.-B. *et al.* Aligned sub-10-nm block copolymer patterns templated by post arrays. *ACS Nano* **6,** 2071–7 (2012).

114. Yi, H. *et al.* Flexible control of block copolymer directed self-assembly using small, topographical templates: potential lithography solution for integrated circuit contact hole patterning. *Adv. Mater.* **24,** 3107–14, 3082 (2012).

115. Bai, J., Zhong, X., Jiang, S., Huang, Y. & Duan, X. Graphene nanomesh. *Nat. Nanotechnol.* **5,** 190–4 (2010).

116. Liang, X. & Wi, S. Transport characteristics of multichannel transistors made from densely aligned sub-10 nm half-pitch graphene nanoribbons. *ACS Nano* **6,** 9700–10 (2012).

117. Zschech, D. *et al.* Ordered arrays of <100>-oriented silicon nanorods by CMOS-compatible block copolymer lithography. *Nano Lett.* **7,** 1516–20 (2007).

118. Liu, G., Thomas, C. S., Craig, G. S. W. & Nealey, P. F. Integration of Density Multiplication in the Formation of Device-Oriented Structures by Directed Assembly of Block Copolymer-Homopolymer Blends. *Adv. Funct. Mater.* **20,** 1251–1257 (2010).

119. Hannon, A. F., Gotrik, K. W., Ross, C. a. & Alexander-Katz, A. Inverse Design of Topographical Templates for Directed Self-Assembly of Block Copolymers. *ACS Macro Lett.* **2,** 251–255 (2013).

120. Tavakkoli K G, a *et al.* Templating three-dimensional self-assembled structures in bilayer block copolymer films. *Science* **336,** 1294–8 (2012).

121. Fredrickson, G. H., Ganesan, V. & Drolet, F. Field-Theoretic Computer Simulation Methods for Polymers and Complex Fluids. *Macromolecules* **35,** 16–39 (2001).

122. Tavakkoli K G, A. *et al.* Rectangular symmetry morphologies in a topographically templated block copolymer. *Adv. Mater.* **24,** 4249–54 (2012).

123. Sidorkin, V. *et al.* Sub-10-nm nanolithography with a scanning helium beam. *J. Vac. Sci. Technol. B Microelectron. Nanom. Struct.* **27,** L18 (2009).

124. Manfrinato, V. R. *et al.* Resolution limits of electron-beam lithography toward the atomic scale. *Nano Lett.* **13,** 1555–8 (2013).

125. Winfree, E., Liu, F., Wenzler, L. a & Seeman, N. C. Design and self-assembly of two-dimensional DNA crystals. *Nature* **394,** 539–44 (1998).

126. Wei, B., Dai, M. & Yin, P. Complex shapes self-assembled from single-stranded DNA tiles. *Nature* **485,** 623–6 (2012).

127. Rothemund, P. W. K., Papadakis, N. & Winfree, E. Algorithmic Self-Assembly of DNA Sierpinski Triangles. **2,** (2004).

128. Kim, H. *et al.* Synthesis and characterization of Janus gold nanoparticles. *Adv. Mater.* **24,** 3857–63 (2012).

129. Macfarlane, R. J. *et al.* Nanoparticle Superlattice Engineering with DNA. *Science (80-.).* **334,** 204–208 (2011).

130. Gotrik, K. W. *et al.* Morphology control in block copolymer films using mixed solvent vapors. *ACS Nano* **6,** 8052–9 (2012).

131. Cai, H. *et al.* Bifunctional nanoarrays for probing the immune response at the single-molecule level. *J. Vac. Sci. Technol. B Microelectron. Nanom. Struct.* **31,** 06F902 (2013).

132. Cherniavskaya, O. *et al.* Fabrication and surface chemistry of nanoscale bioarrays designed for the study of cytoskeletal protein binding interactions and their effect on cell motility. *J. Vac. Sci. Technol. B Microelectron. Nanom. Struct.* **23,** 2972 (2005).

133. Palma, M. *et al.* Selective biomolecular nanoarrays for parallel single-molecule investigations. *J. Am. Chem. Soc.* **133,** 7656–9 (2011).

134. Schvartzman, M. *et al.* Fabrication of Nanoscale Bioarrays for the Study of Cytoskeletal Protein Binding Interactions Using Nanoimprint Lithography. *J. Vac. Sci. Technol. B. Microelectron. Nanometer Struct. Process. Meas. Phenom.* **27,** 61–65 (2009).

135. Schvartzman, M. *et al.* Nanolithographic control of the spatial organization of cellular adhesion receptors at the single-molecule level. *Nano Lett.* **11,** 1306–12 (2011).

136. Chen, Y.-S. *et al.* DNA sequencing using electrical conductance measurements of a DNA polymerase. *Nat. Nanotechnol.* **8,** 452–458 (2013).

137. Schlapak, R. *et al.* Painting with biomolecules at the nanoscale: biofunctionalization with tunable surface densities. *Nano Lett.* **12,** 1983–9 (2012).

138. Gao, B., Bernstein, G. H. & Lieberman, M. Self-assembled monolayers of poly(ethylene glycol) siloxane as a resist for ultrahigh-resolution electron beam lithography on silicon oxide. *J. Vac. Sci. Technol. B Microelectron. Nanom. Struct.* **27,** 2292 (2009).

139. Harnett, C. K., Satyalakshmi, K. M. & Craighead, H. G. Bioactive Templates Fabricated by Low-Energy Electron Beam Lithography of Self-Assembled Monolayers. 178–182 (2001).

140. Senaratne, W. *et al.* Molecular Templates for Bio-specific Recognition by Low-Energy Electron Beam Lithography. 23–33 (2005). doi:10.1385/Nano

141. Chai, J., Wong, L. S., Giam, L. & Mirkin, C. a. Single-molecule protein arrays enabled by scanning probe block copolymer lithography. *Proc. Natl. Acad. Sci. U. S. A.* **108,** 19521–5 (2011).

142. Koh, A. L., McComb, D. W., Maier, S. a., Low, H. Y. & Yang, J. K. W. Sub-10 nm patterning of gold nanostructures on silicon-nitride membranes for plasmon mapping with electron energy-loss spectroscopy. *J. Vac. Sci. Technol. B Microelectron. Nanom. Struct.* **28,** C6O45 (2010).

143. Cherniavskaya, O. *et al.* Fabrication and surface chemistry of nanoscale bioarrays designed for the study of cytoskeletal protein binding interactions and their effect on cell motility. *J. Vac. Sci. Technol. B Microelectron. Nanom. Struct.* **23,** 2972 (2005).

144. Faix, J. *et al.* Cortexillins, major determinants of cell shape and size, are actin-bundling proteins with a parallel coiled-coil tail. *Cell* **86,** 631–42 (1996).

145. Li, X. E., Holmes, K. C., Lehman, W., Jung, H. & Fischer, S. The shape and flexibility of tropomyosin coiled coils: implications for actin filament assembly and regulation. *J. Mol. Biol.* **395,** 327–39 (2010).